KARL FRANZENS UNIVERSITÄT GRAZ

Dissertation
zur Erlangung des akademischen Grades
Doktor der Naturwissenschaften (Dr. rer. nat.)

Pion-Nucleon Scattering in Lattice QCD

Eingereicht von
Valentina Verduci

Angefertigt am Institut für Physik
der Karls-Franzens-Universität Graz

Betreuer und Gutachter
Univ.Prof. Dr. Christian B. Lang
Zweitgutachter
Prof. Dr. Sasa Prelovsek

SEPTEMBER 2014

Präambel

Ich bestätige, dass es sich bei der hier vorgelegten Dissertation um eine Originalarbeit handelt, die von mir selbstständig angefertigt und abgefasst wurde.

(Valentina Verduci)

Abstract. The Euclidean space-time lattice regularization represents an excellent framework for a non-perturbative study of QCD. The main goal in lattice hadron spectroscopy is to reproduce the experimentally observed properties of the hadrons by a first principle computation, in order to verify QCD and gain a deeper understanding of strong interactions.

The ambitious task of this thesis is to drift from the traditional path of lattice hadron spectroscopy and analyze the spectrum of N and Δ by taking into account their resonant nature. The products of their decays are pion-nucleon systems in S and P wave, which represent the main subject of investigation of this work.

The energy spectrum is evaluated using the variational method and the distillation approach. Great interest is also addressed to the phase shift analysis and the possibility of extracting the resonances parameters such as mass and width is explored.

This study sheds some light on different spin and isospin sectors of the QCD baryon spectrum and provides new insight on multi-particle lattice studies, which still constitute an outstanding challenge in lattice QCD.

Zusammenfassung. Die Formulierung auf einem euklidischen Raum-Zeit Gitter ist eine hervorragende Methode um Gitter QCD nicht-perturbativ zu untersuchen. Das hauptsächliche Ziel der Gitter Hadron-Spektroskopie ist, die experimentell beobachteten Eigenschaften der Hadronen in einer ab-initio Rechnung zu bestätigen, um so die QCD zu verifizieren und ein tieferes Verständnis der starken Wechselwirkung zu gewinnen.
Die ehrgeizige Aufgabe dieser Dissertation ist es, den traditionellen Zugang der Gitter Hadron-Spektroskopie zu erweitern und das Energiespektrum von Nukleon und Delta unter Berücksichtigung ihrer Resonanz-Eigenschaft zu studieren. Ihre Zerfallskanäle sind das Pion-Nukleon System in S und P Welle; dies ist das Hauptthema der vorgelegten Arbeit.
Das Energiespektrum wird mittels der Variationsmethode und der sogenannten Distillationsmethode bestimmt. Ein Schwerpunkt ist dabei die Analyse der Phasenverschiebung und daraus die Ermittlung der Resonanzparameter wie Masse und Halbwertsbreite.
Diese Studie liefert Informationen über Spin und Isospin der QCD Baryonen und gibt Einblicke zum Problem von gekoppelten Mehrteilchenkanälen, das noch immer eine Herausforderung in der Gitter QCD darstellt.

Contents

List of Figures

Introduction

The 20th century has been the arena of revolutionary discoveries in particle physics. In 1919 Rutherford reported the first experimental evidences of the existence of the proton, a suitable candidate for being an elementary particle. In the following decades, with the invention of the bubble chamber, a wide variety of particles was discovered: the hadron spectrum [2] started to be explored and it soon became clear that these particles could not be all fundamental.

The properties of the hadron spectrum led to the conjecture of underlying degrees of freedom: the *quarks* [3] [4], bound together into the observable states by the *strong force*. The strong interaction, carried by massless vector bosons called *gluons*, is encoded in the *Quantum Chromodynamics* (QCD) action, a non-abelian quantum gauge field theory of the $SU(3)$ gauge group. QCD was introduced in 1973 and it became soon part of the Standard Model, a theory which merges electromagnetic, strong and weak interactions. Even though QCD seems to explain the structure of the observable matter, an analytic solution has not yet been found. Many different strategies are available, most of them based on a perturbative approach, which requires a small coupling and therefore not suitable for the description of the hadron creation process, where a strong coupling is involved. An alternative approach was introduced by Wilson [5] in 1974 and concerns the study of QCD on a discretized space-time grid: the lattice. The lattice regularization provides an efficient method for ab-initio calculations and a valid way to obtain predictions starting from the QCD action.

In this work we focus our attention on the properties of the hadrons, which are nothing but excited states in the QCD vacuum, and we study them with the help of the lattice discretization. Lattice hadron spectroscopy has so far obtained extraordinary results in the reproduction of the particle spectrum observed in nature. However these studies have been limited as the particles were traditionally treated as stable states. Even considering only strong interactions, most of the hadrons are unstable. Their resonant nature and their coupled decay channels have to be taken into account if a reliable picture wants to be achieved. Formally we would expect that mesons and baryons would couple to their decay states via dynamical vacuum loops generated from the dynamical action,

however in realistic simulations such intermediate channels are not observed (see, e.g., [6–11] for baryon correlation studies) and it seems necessary to explicitly introduce the interpolators of the decay channels. In the last years, thanks to the development of new techniques for the evaluation of correlation functions (e.g. the distillation method [12]) and the extraction of energy states on the lattice (such as the variational method [13–16]), hadron-hadron states have been explicitly included in hadron calculations demonstrating their crucial influence on the observed spectrum (e.g. meson resonance studies [17–22]).

The interplay between resonance levels and hadron-hadron states has been studied in details by Lüscher [14, 23–25], who developed an approach that relates the energy levels in a finite spatial volume to the elastic scattering phase shift in the continuum. Using this approach the parameters of the resonance, such as mass and width, can be extracted.

The energy levels on finite volumes can also be obtained starting from a continuum model for the scattering process [26–29] and allowing a comparison with lattice results. Alternative methods for the identification of the resonance parameters have been also discussed in [26, 30, 31].

Two particle states on the lattice require special care, in particular when moving frames are required [32–36]. Mixing between different partial waves and the opening of further inelastic channels can additionally complicate the situation.

In this work we have investigated pion-nucleon systems coupled with different resonances of the low lying baryon spectrum. An interesting case is the negative parity nucleon channel. The two low lying resonances $N^*(1535)$ and $N^*(1650)$ couple to $N\pi$ in S-wave and so far all the lattice simulations that explored this channel included only 3-quark interpolators [9–11]. These studies do not lead to completely satisfactory results: two low lying energy levels are identified and assigned to the two negative parity resonances. However, the lower of the two levels lies below the $N^*(1535)$ even at unphysical pion masses. In order to clarify the situation we study the coupled system of a nucleon and a pion-nucleon in S-wave.

Another outstanding dilemma in particle physics is represented by the Roper resonance [37]. Effective models with a confining interaction between quarks in light and strange baryons imply a very characteristic mass ordering: the spectrum of the light baryons is expected to be arranged into a succession of positive and negative parity states. However the spectrum of the nucleon, differently from the Λ-hyperon, does not follow this pattern and brings into question the hypothesis of a flavor-blind gluon exchange mechanism [38].

Lattice calculations so far did not manage to shed light on this issue [39–42]: the mass of the Roper resonance appears to be higher than the first negative nucleon state and the nature of this resonance is still unknown. $N(1440)$ decays into $N\pi$ states in P-wave. Therefore we perform a coupled system study in order to investigate this sector of the

nucleon spectrum.
The pion-nucleon P-wave is also the main decay channel of the Δ-baryon, whose resonant nature has only recently been considered in lattice studies [43]. We study the $\{\Delta, N\pi\}$ system and extract information on the resonance.
Note that in our study we take into account only contributions from the $N\pi$ decay channel. Further inelastic decays are expected not to play a role on our lattice due to the unphysical pion mass. It also has to be kept in mind that all the results presented in this thesis are obtained from a discretized version of the QCD action with two light mass-degenerate quarks in finite volume. The effects of electroweak interactions and isospin symmetry breaking are not taken into account.

This thesis is structured as follows: in Chapter 1 and Chapter 2 we briefly introduce the basic concepts of QCD and its discretization on the lattice. In Chapter 3 we list the tools at the basis of lattice hadron spectroscopy. Chapter 4 is devoted to the analysis of multi-particle states setup and the effects of non-rest frames on the symmetries of the system. After a summary of the calculation setup, we display the results of this work. In Chapter 5 we present the outcome of the pion-nucleon scattering in S-wave, which couple to the negative parity sector of the nucleon. Chapter 6 and Chapter 7 are focused on the $N\pi$ system in P-wave. The results for the Roper sector and the Delta baryon are shown. Appendices A, B and C include details about the structure of the interpolators, such as their properties under parity transformations and the isospin structure, while in Appendix D we list all the Wick contractions that have been evaluated in the lattice calculations.

Chapter 1

Quantum Chromodynamics

Quantum Chromodynamics (QCD) is the theory of *strong interactions* between quarks and gluons and it was introduced in 1973 [44] in order to explain the properties of the proton and the whole variety of experimentally observed hadrons. The theory is based on an exact SU(3) color symmetry and the gluon fields, the gauge bosons of QCD, act as vectors of the interaction.

QCD can be formulated in a compact way and it is completely specified by very few parameters: the number of quark flavors with their mass and one coupling constant which determines the strength of the interaction. The main features that characterize the theory are its asymptotic freedom at high energies together with the confinement (not yet rigorously proven), which explains the fact that only color neutral states are observed.

Despite its elegance and the presence of only few parameters, obtaining predictions starting from the QCD action is not an easy task due to the fact that an analytic solution of the theory is still missing. Most of the approaches that are used to deal with QCD are based on perturbation theory: an expansion at small couplings. However, they are destined to fail in the description of the process which leads the generation of the hadrons, since it involves a strong coupling interaction. A possible way to overcome the problem is the lattice discretization.

In this chapter we introduce the QCD action and we briefly list properties and symmetries of the theory in order to prepare the ground for its discretization, which will be discussed in Chapter 2.

1.1 The theory in the continuum

The QCD action can be written as a sum of two parts

$$S_{QCD} = S_F + S_G, \tag{1.2}$$

which encode different kind of interactions: the fermionic and the gauge action.
The fermionic action is written in terms of quark fields: massive fermions defined as Dirac 4-spinors

$$\psi^{(f)}(x)^{\alpha}_{c}, \tag{1.3}$$

where $f = 1..6$ is the flavor index, $c = 1, 2, 3$ is a color index and $\alpha = 1..4$ is a Dirac index. S_F is a bilinear functional of the quark fields

$$S_F[\bar{\psi}, \psi, A] = \sum_{f=1}^{N_f} \int d^4x \bar{\psi}^{(f)}(x) \left[i\gamma^\mu D_\mu(x) - m^{(f)} \right] \psi^{(f)}(x), \tag{1.4}$$

where γ^μ are (4×4) matrices (a representation in Euclidean space can be found in Appendix A). The covariant derivative is defined as

$$D_\mu(x) = \partial_\mu - iA_\mu(x), \tag{1.5}$$

with $A_\mu(x)_{cd}$ being the gluon field: a vector field which carries a Lorenz index μ. The QCD action is required to be invariant under local rotations of the quark color indices, which constrains A_μ to be an element of the $su(3)$ algebra. For the same reason it is necessary to introduce a gauge action of the form

$$S_G = \frac{1}{2g^2} \int d^4x \mathrm{Tr} \left[F^{\mu\nu}(x) F_{\mu\nu}(x) \right], \tag{1.6}$$

where g is the QCD coupling constant, while the trace over color indices guarantees the gauge invariance. The definition of $F_{\mu\nu}$ hides the main differences between QCD and QED:

$$\begin{aligned} F_{\mu\nu}(x) &= i[D_\mu(x), D_\nu(x)] = \\ &= \partial_\mu A_\nu(x) - \partial_\nu A_\mu(x) + i[A_\mu(x), A_\nu(x)], \end{aligned} \tag{1.7}$$

where the commutator does not vanish since $su(3)$ is non-abelian. The main consequence on the action is the presence of cubic and quartic terms of self interaction among gluons, which are mainly responsible for confinement and determine the non-triviality of QCD.

In the functional integral formalism of QCD the action enters the partition function as

$$Z = \int D[A_\mu] D[\bar{\psi}] D[\psi] e^{iS_{QCD}}, \tag{1.8}$$

affecting its convergence in different ways. The introduction of the lattice regularization is in fact determined by the necessity of dealing with this Z:

- Due to the gauge symmetry, the integral in Eq. (1.8) results in a sum of infinitely many copies which can be eliminated by fixing the gauge. However, on a finite lattice this integral is finite and there is no need for gauge fixing as long as gauge invariant quantities are computed.
- The integral in Eq. (1.8) diverges due to quantum fluctuations and has to be regularized. A renormalization of the parameters is also needed and their dependence on the scale makes perturbation theory approaches only valid in restricted ranges. The lattice is not affected by this problem thanks to its non-perturbative nature, giving access to different aspects of QCD including the mass generation mechanism.

As we will see in the next chapter, the discretization of QCD is a non trivial process. The hardest task will be to resemble as good as possible the symmetries that characterize QCD in the continuum:

- Poincaré invariance, which includes Lorenz and translational invariance;
- Gauge invariance;
- Symmetries under discrete transformations such as parity, time-reversal and charge conjugation;
- Chiral symmetry realized for massless quarks;
- Flavor symmetry for mass-degenerate quarks.

1.2 QCD hadron spectrum

As we have seen, the building blocks of QCD are the gluons together with 6 flavors of quarks. Due to the confinement property of the theory, these blocks must be combined in colorless structures which are the only objects that can be observed: the hadrons [2]. The symmetry pattern of the observed hadron spectrum has inspired the constituent quark model [3**?**]: an underlying flavor $SU(3)$ symmetry imposes strong constraints on the composition of the hadrons (see Fig. 1.1):

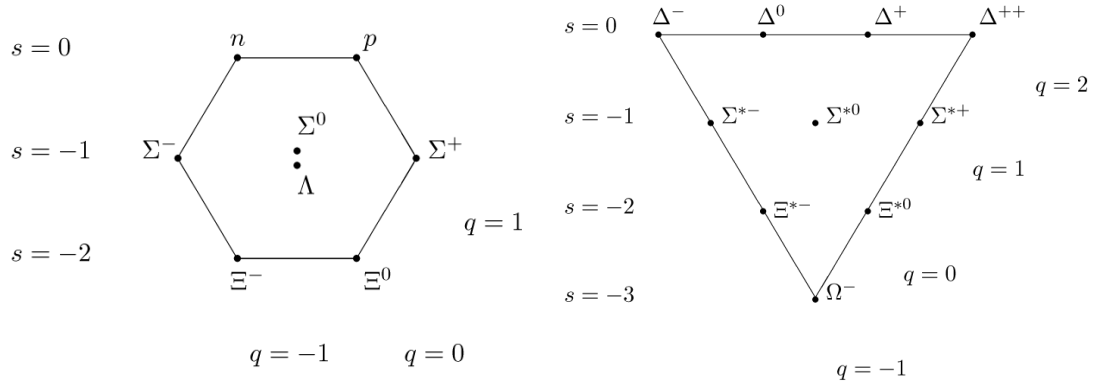

FIGURE 1.1: A schematic representation of the baryon octet and decuplet: the particles are organized following an underlying $SU(3)$ flavor symmetry.

Hadron	Quark content	Group representation
meson	$\bar{q}\,q$	$\mathbf{3} \otimes \bar{\mathbf{3}} = \mathbf{8} \oplus \mathbf{1}$
baryon	$q\,q\,q$	$\mathbf{3} \otimes \mathbf{3} \otimes \mathbf{3} = \mathbf{10} \oplus \mathbf{8} \oplus \mathbf{8} \oplus \mathbf{1}$

However in the experimentally measured spectrum there are some resonances that do not fit in the quark model as well as aspects that are still unclear.
An example is the $(J = 1/2, I = 1/2)$ sector: the nucleon spectrum.

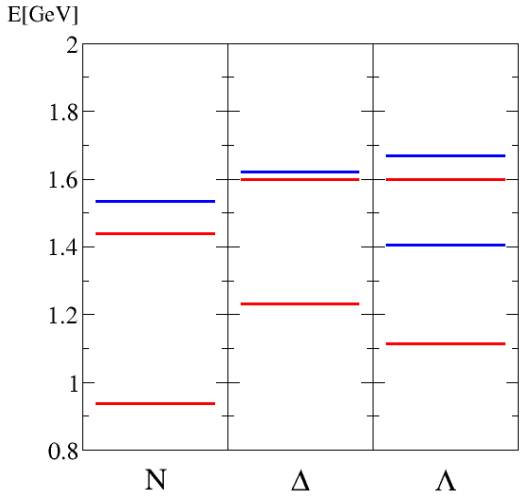

FIGURE 1.2: Experimental values of the low-lying spectra of nucleon, Δ-resonance and Λ-hyperon. The red lines represent states with positive parity and the blue lines are negative parity states. Note the different ordering between the spectra of baryons constituted by light quarks (N and Δ) compared to the spectrum of the Λ, which contains a strange quark.

A simple model with a confining and color-blind interaction would imply that in the baryon spectrum masses of positive and negative parity alternate [38]. This is the case for the Λ-hyperion, but not for the nucleon: the Roper resonance $N^+(1440)$ lies below $N^-(1550)$ breaking the expected pattern. The reverse mass ordering observed in nature might be a hint for the exotic nature of the Roper resonance: a pentaquark composition would place it out of the scheme and explain the unconventional mass [45–48]. Another possibility is the assumption of a flavor-spin dependent interaction between valence quarks of the Goldstone boson exchange type [49–51]. A Roper-like behavior is actually observed also in the Delta spectrum triggering similar questions.
Other areas of the spectrum might hint the presence of non QCD-like objects such as glueballs, hybrids, tetraquarks and the aforementioned pentaquarks. A further inspection of the QCD spectrum is hopefully going to shed some light on the nature of the states. At the same time it becomes crucial to find an approach that can systematically test whether QCD can predict all the properties of the resonances, among which the mass and the width.

Chapter 2

QCD on the Lattice

In this chapter we explain how to discretize the QCD action on the lattice and which are the main properties and symmetries of the resulting framework. Since many books and reviews are available [52–59], we will just provide a short overview in order to make this text self contained.

Lattice QCD represents an ideal ground for testing non-perturbative QCD phenomena despite its limits, which can be summarized in

- unphysical pion mass,
- finite volume effects,
- explicit chiral and Poincaré symmetry breaking.

In order to understand these issues we will briefly explain how to rewrite the QCD action on a discrete Euclidean lattice and which are advantages and disadvantages of this procedure.

2.1 The discretized action

Considerable steps forward in the understanding of the mass generation have been made thanks to Chiral Perturbation Theory studies [60, 61] as well as models based on dynamical symmetry breaking [62, 63], however none of them includes quarks and gluons as fundamental degrees of freedom. Introduced in 1974 by K.G. Wilson [5], the lattice discretization represents a valid tool to perform ab-initio calculations using quarks and gluons as building blocks.

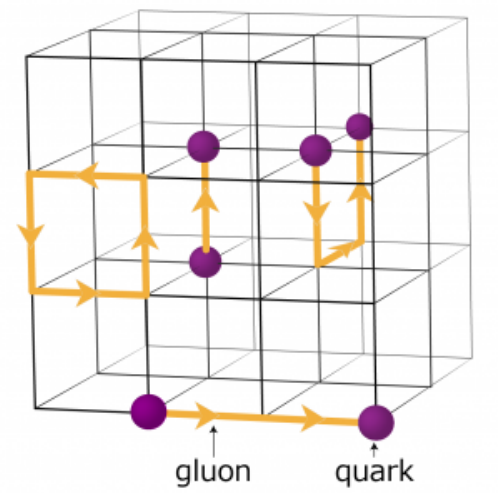

FIGURE 2.1: A sketch of the discretization of QCD on a cubic lattice.

Lattice QCD is formulated on a discrete Euclidean space-time grid (the lattice Λ) where the minimum distance a is the lattice spacing. Every fermionic degree of freedom is assigned to a site of the lattice, while the gluons are placed on the links (see Fig. (1.1)). As a consequence

- the lattice spacing serves as natural ultraviolet cutoff;
- due to its discrete nature, lattice quantum field theories can be simulated on a computer with the same techniques used in Statistical Mechanics.

A naive discretization with the substitution of the derivatives in the continuum expression for S_F gives

$$S_F^{(0)}[\bar{\psi},\psi] = a^4 \sum_{n\in\Lambda} \bar{\psi}(n) \left\{ \sum_\mu \gamma_\mu \frac{U_\mu(n)\psi(n+\hat{\mu}) - U_{-\mu}(n)\psi(n-\hat{\mu})}{2a} + m\psi(n) \right\}, \quad (2.1)$$

where the requirement to preserve the gauge symmetry leads to the introduction of the gluon fields U_μ. The link variables are oriented (from n to $n+\hat{\mu}$) and they are elements of the group $SU(3)$.

The simplest gauge invariant object that can be constructed on the lattice coincides with a closed loop of 4 gauge links

$$U_{\mu\nu}(n) = U_\mu(n) U_\nu(n+\hat{\mu}) U_\mu(n+\hat{\nu})^\dagger U_\nu^\dagger(n), \quad (2.2)$$

and $U_{\mu\nu}$ is called *plaquette*. A function of the plaquette is defined as the discretized version of the gauge action

$$S_G[U] = \frac{2}{g^2} \sum_{n\in\Lambda} \sum_{\mu<\nu} Re\ \mathrm{Tr}[\mathbb{1} - U_{\mu\nu}(n)], \tag{2.3}$$

which approaches its continuum counterpart for $a \to 0$ with corrections $O(a^2)$.
The fermionic action as defined in Eq. (2.3) suffers from the *doubling* problem: when inverting the Dirac operator, one obtains a quark propagator which has 15 extra poles, in addition to the original one. In order to get rid of these copies (the doublers) Wilson suggested to add an $O(a^{-1})$ term which corresponds to adding an extra mass to the doublers mass: in the continuum limit these artificial copies of the original fermion decouple from the rest of the theory due to their extremely heavy mass. This term is added to the naive version of the fermion action so that

$$S_f[\bar{\psi}, \psi, U] = a^4 \sum_{n,m\in\Lambda} \bar{\psi}(n) D(n|m) \psi(m), \tag{2.4}$$

with

$$D^{(f)}(n|m) = \left(m^{(f)} + \frac{4}{a}\delta_{nm} \right) \delta_{nm} - \frac{1}{2a} \sum_{\mu=\pm1}^{\pm4} (1 - \gamma_\mu) U_\mu(n) \delta_{n+\hat{\mu},m}, \tag{2.5}$$

which is γ_5-hermitian since

$$(\gamma_5\, D)^\dagger = \gamma_5 D. \tag{2.6}$$

This property implies that the determinant of the Dirac operator is real, which is crucial for Monte Carlo simulations.

2.1.1 Symmetries

The symmetries appear to play a decisive role since they define universality classes: different theories belonging to the same universality class are expected to provide the same predictions for physical observables when the limit $a \to 0$ is performed. The final action conserves many of the symmetry properties of the continuum action: the gauge symmetry, together with the discrete symmetries under parity and charge conjugation are preserved. On the other hand chiral symmetry, which requires

$$D\gamma_5 + \gamma_5 D = 0, \tag{2.7}$$

is explicitly broken for Wilson fermions even at vanishing quark masses due to the term that has been introduced to remove the doublers. The well known No-Go Theorem by

FIGURE 2.2: The symmetries of the sphere $O(3)$ are transformed in the symmetries of a hypercube O_h when the space is discretized.

Nielsen and Ninomiya [64] states the impossibility of defining a discretized version of the fermionic action which has no doublers and at the same time preserves chiral symmetry. Ginsparg and Wilson formulated [65] a new definition of chiral symmetry on the lattice as

$$D\gamma_5 + \gamma_5 = aD\gamma_5 D, \tag{2.8}$$

which reduces to the definition in the continuum for $a \to 0$.
Another symmetry that does not survive after the discretization is the Poincaré symmetry $SU(2)$ (double cover of $SO(3)$ which includes half integer spin representations): it is broken to a discrete subgroup ${}^2O$ (double cover of the octahedral group O). The breaking of the Poincaré symmetry determines complications in the definition of spin on the lattice, affecting the construction of the interpolators (see Section 3.2).

2.1.2 Wilson clover action and HYP smearing

Other possibilities for the lattice action exist: as long as the final action belongs to the same universality class and therefore gives the same predictions in the continuum limit, new terms can be included in the action to improve its scaling behavior and reduce discretization errors.
A common approach is smearing: links and/or quark sources are redefined as functions of the neighboring variables. In this section we define the two types of smearing that are used in the action which enters in the calculations of the current work: a Wilson Clover action with HYP smearing [66, 67].

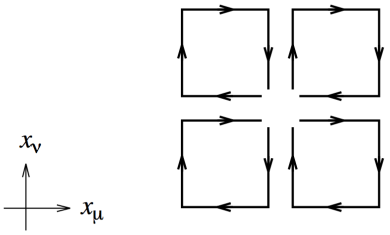

FIGURE 2.3: Lattice representation of the clover term $F_{\mu\nu}$.

The link smearing consists in averaging each link with a specified selection of neighboring links, usually the staple $S_\mu(n)$ defined as

$$S_\mu(n) = \sum_{\nu=\pm\mu} U_\nu(n)U_\mu(n+\hat{\nu})U_\nu(n+\hat{\mu})^\dagger. \tag{2.9}$$

The APE smearing was the first to be introduced [68] and defines the new link as

$$V_\mu(n) = P_{SU(3)}\left[(1-\alpha)U_\mu(n) + \frac{\alpha}{6}S_\mu(n)\right], \tag{2.10}$$

with α to be tuned. $P_{SU(3)}$ represents the projection onto $SU(3)$. The HYP [69] smearing used for our action is a generalization of the APE smearing in all the directions

$$\bar{U}_{\mu,\nu\sigma}(n) = P_{SU(3)}\left[(a-\alpha_3)U_\mu(n) + \frac{\alpha_3}{2}\sum_{\rho\neq\pm(\mu,\nu,\sigma)} S_\rho(n)\right], \tag{2.11}$$

$$\tilde{U}_{\mu,\nu}(n) = P_{SU(3)}\left[(a-\alpha_2)U_\mu(n) + \frac{\alpha_2}{4}\sum_{\sigma\neq\pm(\mu,\nu)} \bar{S}_\sigma(n)\right], \tag{2.12}$$

$$V_\mu(n) = P_{SU(3)}\left[(a-\alpha_1)U_\mu(n) + \frac{\alpha_1}{6}\sum_{\nu\neq\pm\mu} \tilde{S}_\nu(n)\right], \tag{2.13}$$

where $\bar{S}$ is built from $\bar{U}$ using Eq. (2.9) and $\tilde{S}$ is defined from $\tilde{U}$. Other smearing solutions can be found, for example, in [70–76].

Wilson fermions are affected by discretization errors determined by a non-negligible cut-off. An $O(a)$ improvement is obtained by adding to the Wilson action a clover term, where $F_{\mu\nu}$ is a lattice version of the field strength tensor (Fig. 2.3) [77]

$$S_{imp} = S_W + a^5 \sum_x c_{SW}\bar{\psi}(x)\frac{1}{8i}[\gamma_\mu,\gamma_\nu]F_{\mu\nu}(x)\psi(x), \tag{2.14}$$

with

$$F_{\mu\nu}(x) = \frac{1}{2}(P_{\mu\nu}(x) - P^{\dagger}_{\mu\nu}(x)) \tag{2.15}$$

and

$$\begin{aligned} P_{\mu\nu}(x) = {} & U_\mu(x)U_\nu(x+\hat{\mu})U^{\dagger}_\mu(x+\hat{\nu})U^{\dagger}_\nu(x) \\ & + U_\nu(x)U^{\dagger}_\mu(x-\hat{\mu}+\hat{\nu})U^{\dagger}_\nu(x-\hat{\mu})U_\mu(x-\hat{\mu}) \\ & + U^{\dagger}_\mu(x-\hat{\mu})U^{\dagger}_\nu(x-\hat{\mu}-\hat{\nu})U_\mu(x-\hat{\mu}-\hat{\nu})U_\nu(x-\hat{\nu}) \\ & + U^{\dagger}_\nu(x-\hat{\nu})U_\mu(x-\hat{\nu})U_\nu(x+\hat{\mu}-\hat{\nu})U^{\dagger}_\mu(x). \end{aligned} \tag{2.16}$$

Other types of quark smearing exist. Among them the distillation method plays a crucial role in modern calculations and will be extensively discussed in Section 3.4.

2.2 Monte Carlo

The discretization on a Euclidean space-time has the advantage of reducing the quantum fields of the original theory to a countable number of classical variables. Even though sophisticated algorithms and vast computing resources are needed, a numerical evaluation of the discretized QCD path integral becomes possible.
The vacuum expectation values are written as

$$\langle O \rangle = \frac{1}{Z}\int D[U]D[\bar{\psi}\psi]O[U,\bar{\psi},\psi]e^{S_G[U]}e^{S_F[\bar{\psi},\psi]}, \tag{2.17}$$

with

$$Z = \int D[U]D[\bar{\psi}\psi]e^{S_G[U]}e^{S_F[\bar{\psi},\psi]}, \tag{2.18}$$

where the path integral is computed as integral over all the possible field configurations. This sum is approximated using Monte Carlo methods [78], where the fermion and gluon actions are the weight factors that enter the importance sampling when the Markov chain of configurations is generated.
The fermion action, however, requires a special treatment: the quark fields are spinors obeying the Pauli principle and have to be treated as Grassmann variables, which are not very suitable for computer simulations. It is crucial to notice that S_F is bilinear in ψ and $\bar{\psi}$, which can be integrated out analytically so that

$$Z_F[U] = \int D[\psi\bar{\psi}]e^{-\sum_f \bar{\psi}D[U]\psi} = \det D^{N_f}[U] \tag{2.19}$$

and in general

$$Z = \int D[U] Z_Q[U] e^{-S_G[U]} = \int D[U] e^{-S_G[U]} \left(\det D[U]\right)^{N_f} . \tag{2.20}$$

For $N_f = 2$ degenerate fermions the term $(\det D)^2$ is always positive, therefore it can be included in the importance sampling, even though the simulation becomes very expensive in terms of computational time due to the non-locality of the Dirac operator.

2.3 Advantages and disadvantages of the discretization

The lattice discretization provides a non-perturbative regularization of QCD, where the lattice spacing serves as ultraviolet cut-off and a numerical evaluation of the path integral is possible. Therefore Lattice QCD (LQCD) allows to calculate predictions from first principles: the only parameters that have to be fixed are the number and the mass of the quark flavors, together with the coupling constant.
Even if LQCD represents a powerful tool, it is affected by limitations that have to be kept in mind when a physical interpretation of the results is done. The main limitation to LQCD calculations is connected to the availability of computer resources and the efficiency of the algorithms: they determine the size of the systematic errors (finite volume, large lattice spacing, unphysical quark masses) and statistical errors (Monte Carlo integration) and therefore the possibility of producing reliable predictions.
In the last three decades the field experienced revolutionary improvements: large dedicated high performance computers became available, time-effective algorithms were developed and a deeper understanding of the limitations of the method made LQCD one of the most powerful approaches for the study of QCD.

One of the aspects where great interest is devoted is the study of the QCD spectrum, its excited states and the decays processes. The ingredients that are needed in a lattice hadron spectroscopy study are

- an observable that can be measured on the lattice with statistical precision;
- techniques that allow to produce high resolution data;
- an approach that allows to transform the results obtained from lattice calculations into data which can be compared with experiments such as mass and width;

and will be explained in details in Chapter 3 and Chapter 4.

Chapter 3

Hadron spectroscopy on the lattice

3.1 Euclidean correlation function

Due to the finiteness of the spatial volume the energy spectrum of the correlation functions is discrete. The energy levels corresponding to the eigenstates of the Hamiltonian on the lattice can be determined by evaluating the following observable:

$$C(t) = \langle O(t)\,\overline{O}(0)\rangle \ , \tag{3.1}$$

the Euclidean correlation function between the initial state at time $t = 0$ (source) created by the operator $\overline{O}(0)$ and the final state which is annihilated by $O(t)$ (sink). Each operator (in this context called interpolator) lives on the corresponding Euclidean time slice.

The contribution from each state of the spectrum can be visualized by inserting a complete set of eigenstates of the Hamiltonian in Eq. (3.1), with the corresponding eigenvalues

$$C(t) = \langle O(t)\,\overline{O}(0)\rangle = \sum_n \langle O(t)|n\rangle \mathrm{e}^{-E_n t}\langle n|\overline{O}(0)\rangle \ , \tag{3.2}$$

where the sum runs over all the states with the same quantum numbers of the source/sink operators.
Due to the form of Eq. (3.2), which involves an exponential decay in the time direction, the contribution of different states $|n\rangle$ changes for different values of t:

$$C(t) = A_0 e^{-E_0 t} + A_1 e^{-E_1 t} + A_2 e^{-E_2 t} + ... \tag{3.3}$$

from which is clear that the ground state dominates at large time extents, but at small values of t the contributions from the higher states cannot be neglected. In Section 3.3 we will explain how to disentangle them. Now we focus on the ground state.

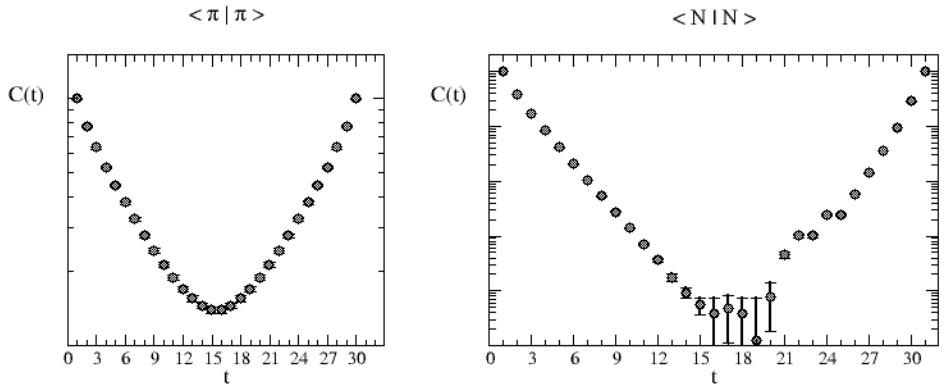

FIGURE 3.1: The diagonal correlation function. We observe that $C(t)$ is symmetric for mesons (LHS) except for statistical fluctuations. In the case of baryon correlation functions which have been parity projected (RHS) we observe the propagation of N^+ in $t = (0 \to N_t/2)$ and the propagation of N^- in the opposite direction $t = (N \to N_t/2)$. Note that the correlator is plotted in logarithmic scale.

For mesons the correlator shows a completely symmetrical behavior and the propagation in t and $N_T - t$ is the same, except from a possible minus sign which depends on the choice of the interpolators:

$$C(t) = A_0\, e^{-E_0 t} \pm A_0\, e^{-E_0 (N_T - t)}. \tag{3.4}$$

The baryon case is different: if a parity projection is performed on the interpolator (see Appendix B), the correlator will be asymmetric, with one parity propagating in one direction and its parity partner propagating in the opposite time direction (see Fig. 3.1)

$$C(t) = A_0^+\, e^{-E_0^+ t} \pm A_0^-\, e^{-E_0^- (N_T - t)}. \tag{3.5}$$

The estimation of the eigenstates is made easier if the interpolators used in the evaluation of the correlation function are constructed so that their overlap with the states of interest is maximized. In this way the asymptotic behavior of the correlator starts at earlier time enhancing the accuracy in the determination of the energies.

The construction of the interpolators has to follow some basic steps to guarantee correct quantum numbers and the fulfilling of the spatial symmetries on the lattice. Nevertheless a large amount of freedom is still left and it will be used in Section 3.4 to rewrite the interpolators and combine the traditional approach with a new smearing technique.

j	Irrep
0	A_1
$1/2$	G_1
1	T_1
$3/2$	H
2	$E + T_2$
$5/2$	$G_2 + H$

TABLE 3.1: Reduction of SU_2 to ${}^2O_h$ [79].

3.2 Interpolator design and momentum projection

The interpolators have to be constructed from gauge invariant object and they have to resemble the properties of the particle that they are designed to represent.

The properties that the interpolators have to satisfy are:

- quark flavor content and spin structure;
- color singlet;
- transformations under C and P as defined in Appendix B;
- spin properties: they must transform following the correct scalar/spinorial irreducible representation of the discrete symmetry group;
- definite momentum.

All the interpolators are designed to maximize the overlap with the physical states and at the same time minimize the number of propagators involved in the calculation.
Using the quarks as building blocks we can easily define operators with the correct quark content and isospin properties. The Dirac structure is chosen so that transformations under parity and charge conjugation give the expected result (after the projection to zero momentum is performed).

An example of a simple meson interpolator is

$$O_M(n) = \bar{q}(n)\Gamma q(n) = \bar{q}(n)^{(c)}_{\alpha}(\Gamma)_{\alpha\beta}\, q(n)^{(c)}_{\beta}, \tag{3.6}$$

where $n = (\mathbf{n}, n_4)$ and the sum over color and Dirac indices is implied. It is a color singlet and in the rest frame it transforms as an element of one of the irreducible representations of O_h (see Table 3.1). Its parity and charge conjugation properties are computed explicitly in Appendix B.

A meson correlator will have the form

$$\begin{aligned}\langle O_M(n)\bar{O}_M(m)\rangle &= \langle \bar{q}_1(n)\Gamma q_2(n)\bar{q}_2(m)\Gamma q_1(m)\rangle = \\ &= -\mathrm{Tr}\,[\Gamma D^{-1}_{q_1}(n|m)\Gamma D^{-1}_{q_2}(m|n)],\end{aligned} \tag{3.7}$$

where the evaluation of the propagators D^{-1} implies the inversion of the Dirac matrix whose entries are $N_M = N_S^3 \times N_T \times N_C \times N_D$ (space, time, color and Dirac indices respectively). The inverse of the Dirac operator (the quark propagator) is evaluated on prepared quark sources and the inversion is obtained by solving iteratively

$$G = D^{-1}S \qquad\qquad DG = S. \tag{3.8}$$

Many different strategies have been developed for this purpose [80–83].
An analogous process can be followed to construct the baryon interpolators

$$O_B(n) = \epsilon_{abc}\,\Gamma^{(1)}\,q_1(n)_a\,\left(q_2(n)^T_b\,\Gamma^{(2)}\,q_3(n)_c\right), \tag{3.9}$$

where q_2 and q_3 are usually combined in a so called *diquark* which has no dynamical meaning, but helps in defining the total isospin of the interpolator.

As a consequence the baryon correlator reads

$$\begin{aligned}\langle O_B(n)\bar{O}_B(m)\rangle &= \langle\,\Gamma^{(1)}\,q_1(n)\,\left(q_2(n)^T\,\Gamma^{(2)}\,q_3(n)\right)\,\left(\bar{q}_3(m)^T\,\Gamma^{(2)^\dagger}\,\bar{q}_2(m)\right)\,\bar{q}_1(m)\,\Gamma^{(1)^\dagger}\,\rangle = \\ &= \mathrm{Tr}\,\left[\Gamma^{(1)}\,\Gamma^{(1)^\dagger}\,D^{-1}_{q_1}(n|m)\,\left(D^{-1}_{q_2}(n|m)\,\Gamma^{(2)}\,\Gamma^{(2)^\dagger}\,D^{-1}_{q_3}(n|m)\right)\right].\end{aligned} \tag{3.10}$$

The final step that has to be implemented is a momentum projection. The interpolator with definite spatial momentum is obtained by Fourier transforming the original $O(n)$

$$O(\mathbf{p}, n_t) = \sum_{\mathbf{n}} O(\mathbf{n}, n_t)\,e^{i\,a\,\mathbf{np}} \tag{3.11}$$

which is defined on each time slice n_t.

3.3 Variational method

Extracting the energy levels from Eq. (3.2) can be done in different ways. If the interest is focused on the ground state, which dominates the asymptotic behavior for large t, one exponential fit to the correlator will be sufficient. However if excited states are subject of study, different techniques have to be applied.

For the evaluation of the spectrum in our work we use the variational method [13–16] which is one of the most popular techniques used in hadron spectroscopy for the extraction of a tower of excited energy states.
Other approaches are the *Bayesian analysis* [84–86] and the *Maximum entropy method* [87]. However, they usually require data with higher statistics to produce solid results. On the other hand the variational method works even if the quality of the data is not excellent, which is the situation in most of the calculations in lattice QCD where the evaluation of correlation functions is numerically extremely expensive.

The distinctive characteristic of the variational method is the requirement of evaluating a matrix of cross correlators $C(t)$ which spans over a set of different interpolators $O_i(t)$

$$C_{ij}(t) = \langle O_i(t)\, \bar{O}_j(0)\rangle = \sum_n \langle O_i|n\rangle e^{-E_n t}\langle n|\bar{O}_j\rangle\,, \tag{3.12}$$

The choice of the number and the type of the interpolators has to be made carefully. The interpolators at sink and source respectively must have the same quantum number, in other words they should couple to the same state or eventually its decay product, otherwise C_{ij} will be statistically compatible with zero. The cross correlation matrix is diagonalized to extract different eigenstates, i.e., energy levels of the selected sector of the spectrum. In principle if many interpolators are used in the analysis, many excited states will be computed. In reality using a too wide basis of interpolators introduces additional noise. An equilibrate choice has to be made.

Once C_{ij} is computed, we need to solve the generalized eigenvalue problem

$$C(t)\vec{u}_n(t) = \lambda_n(t)C(t_0)\vec{u}_n(t), \tag{3.13}$$

to disentangle the eigenstates $|n\rangle$ with the eigenvalues

$$\lambda_n(t,t_0) \sim e^{-E_n(t-t_0)}\left(1 + O(e^{-\Delta E_n(t-t_0)})\right), \tag{3.14}$$

where ΔE_n is the gap between the energy level E_n and the next. The energy values are extracted using correlated fits of the eigenvalues to one or two exponentials. The two exponential fits start at smaller t and are meant to verify that the extracted levels agree with the results obtained from one-exponential fits starting at larger t: there is the possibility that contributions from higher states of the spectrum bias the one exponential fit and what is thought to be an asymptotic behavior might be in reality only an intermediate plateau. On the other hand, if the signal drops early in time (the statistical quality of $C(t)$ is often an issue), a two exponential fit might not be possible. The reliability of the evaluated energy levels decreases for higher $|n\rangle$, the ground state being the most reliable one.

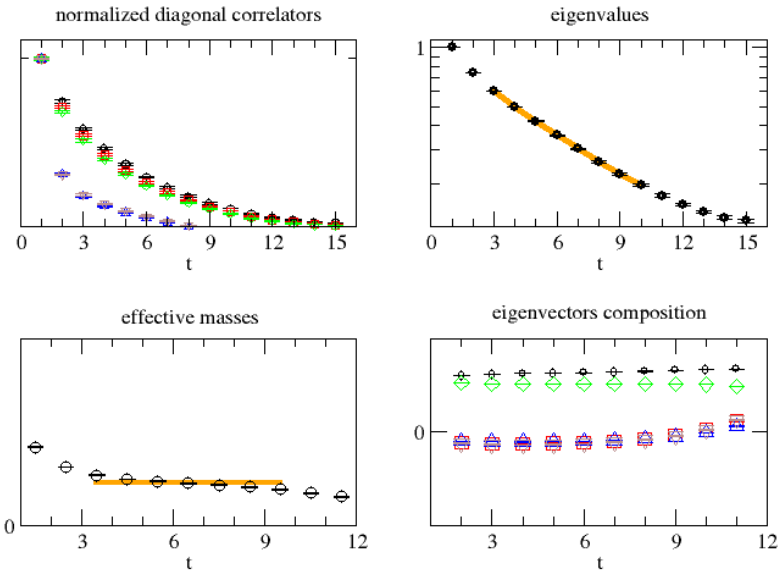

FIGURE 3.2: Example of the variational method steps for the determination of the pion mass. (1) Top-left: the diagonal correlation function is evaluated. It has the expected exponential decay behavior. (2) Top-right: from the diagonalization of the correlation matrix it is possible to plot the eigenvalues relative to different eigenstates. Here we show those for the lower level. The fit (orange band) that leads to the final result is performed on the eigenvalues. (3) Bottom-left: the effective masses are plotted. They serve to guide the eye in the choice of the fit range and to locate the plateau. (4) Bottom-right: a physical interpretation for the observed state can be inferred from the study of the eigenvectors.

A source of systematic error is the choice of the fit range in t. In order to guide the eye in the choice of the fit range we plot the so-called effective energies

$$E_n(t) = \log \frac{\lambda_n(t)}{\lambda_n(t+1)}, \tag{3.15}$$

which we expect to exhibit a plateau-like behavior.

The final check is done with the eigenvector composition of each state: ideally each interpolator couples to one state and it is orthogonal to the others. In reality it might happen that each state has contributions from different interpolators.

The eigenvector analysis provides information concerning the nature of the state, which can be inferred from the interpolators it couples to. We expect one state to be well defined and identifiable where its eigenvectors composition is stable. The fit range will be chosen to fulfill this requirement (see Fig. 3.2 for an example of the whole process).

3.4 Distillation method

As we have just seen, the physically relevant signal in the correlation function evaluated on the lattice has an exponential decay that makes the evaluation of the energy levels hard if not impossible, due to the fact that the statistical fluctuations of the Monte Carlo calculation completely dominate over the signal. Since we are interested in extracting excited states, the quality of the signal plays a fundamental role and a solution has to be found. A way to overcome the problem, or at least to improve the quality of the signal, is to make use of smearing techniques. In this section we will see that a specific kind of non-local smearing can be applied to the quark fields in the interpolators in order to improve the evaluation of the spectrum [12].
The main features that make this technique an extremely powerful approach and an extraordinary useful tool in our study can be summarized as follows:

- the procedure is numerically accessible and flexible: all the information relative to the specific form of the interpolator are factored out;
- it projects onto the lowest part of the spectrum, which is the one we are interested in;
- thanks to this approach the evaluation of the correlation function becomes easier. The point-to-all is replaced by a propagators where the whole time-slice contributes. This improves the statistics and allows the evaluation of disconnected diagrams.

The role of this method called *Distillation* is to provide a shortcut for the evaluation of the correlators and therefore allow demanding calculations that would be otherwise not accessible. This method has been successfully applied in several studies, including baryon correlation functions [8, 9, 17, 20, 21, 88, 89].
Lattice calculations are in general extremely expensive in CPU time and an improvement in the computation approach can make the difference between a project which has to be discarded as impossible due to computing resources reasons and a project that can be actually realized.

As discussed in Section 3.1 the freedom in the choice of the interpolators allows us, for instance, to apply a smearing operator to the quark fields before the interpolator is constructed.
The distillation process consists in applying a smoothing function which is chosen to be a truncated expansion of the three dimensional Laplacian operator. The Laplacian is

defined on our lattice as

$$-\nabla^2_{xy}(t) = 6\,\delta_{xy} - \sum_{j=1}^{3}\left(\tilde{U}_j(x,t)\,\delta_{x+\hat{j},y} + \tilde{U}_j^{\dagger}(x-\hat{j},t)\,\delta_{x-\hat{j},y}\right), \tag{3.16}$$

where $\tilde{U}$ are the gauge fields.
Once the Laplacian operator is defined, a smearing operator can be constructed as

$$J_{\sigma,n_\sigma}(t) = \left(1 + \frac{\sigma\nabla^2(t)}{n_\sigma}\right)^{n_\sigma} \to_{(n_\sigma\to\infty)} \to \exp\left(\sigma\nabla^2(t)\right), \tag{3.17}$$

where σ and n_σ are parameters to be fixed. It is clear that for high n_σ the highest modes of the Laplacian operator are mainly suppressed due to the exponential, therefore replacing ∇ with its truncated expansion (discarding the highest modes) represents a good approximation and fits in the definition of smearing as a tool to suppress the non relevant contributions. The distillation operator is therefore defined as

$$\Box_{xy}(t) = \sum_{k=1}^{N_v} v_x^{(k)}(t)\, v_y^{(k)\,\dagger}(t), \tag{3.18}$$

and it projects the fields onto the subspace spanned by the first N_v eigenvectors of the Laplacian (sorted by eigenvalue). Note that summing over all eigenvectors reproduces the delta function, the spectral representation of unity.
The distillation operator can in principle be constructed starting from the truncated representation of any lattice operator, however using the Laplacian operator guarantees that all the symmetry properties of the original interpolator are conserved after the distillation process, thanks to the fact that ∇ transforms as a scalar under rotations, it is invariant under P and C transformations and it is gauge covariant.

In that way we introduce on each given time slice a set of separable quark smearing sources in the form

$$\begin{aligned} q_{c,\alpha}(\vec{x}) &\to \sum_{\vec{x}'} \Box_{cd}(\vec{x},\vec{x}')q_{d,\alpha}(\vec{x}') \\ &\equiv \sum_{\vec{x}'}\sum_{i}^{N_v} v_c^i(\vec{x})v_d^{i*}(\vec{x}')q_{d,\alpha}(\vec{x}'), \end{aligned} \tag{3.19}$$

where c, d and α denote color and Dirac indices and summation over the paired indices is implied. The value of N_v depends on the physical size of the lattice and values in the range $N_v = (32 - 96)$ were found suitable for our lattice setup [17].

Instead of quark propagators $G_{c\mu;d\nu}(x, x_0)$ from one source located at x_0 to other points on the lattice we are now computing propagators between eigenmode sources, so-called

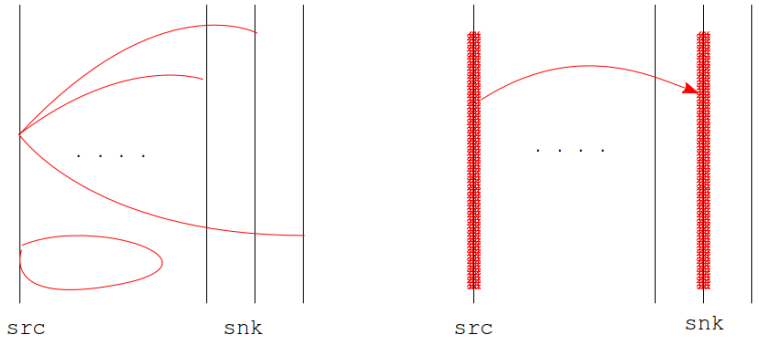

FIGURE 3.3: Graphic explanation of the differences between a traditional one-to-all approach and the distillation method. Left: the one-to-all approach works very well with connected diagrams. The quark lines are estimated using one fixed source and all the time-slices as sink. When a backtracking loop has to be estimated, however, the approach transforms into a one-to-one method and it does not give statistically reliable results. Right: after distillation each time-slice results globally smeared and the eigenvectors which enter the smearing process are used as source/sink of the propagators. In this way an all-to-all approach becomes affordable.

perambulators (see Fig. 3.3)

$$\tau_{\mu\nu}(j, t_{\rm snk}; i, t_{\rm src}) \equiv v_d^{j*}(\vec{x}, t_{\rm snk}) G_{d\mu;c\nu}(\vec{x}, \vec{y}) v_c^i(\vec{y}, t_{\rm src}) \ . \tag{3.20}$$

The computation of the propagators becomes much more affordable: instead of inverting the entire Dirac matrix of size $N_M = N_T\, N_S^3\, N_C$ (where N_C is the number of colors, N_S is the spatial size of the lattice and N_T the temporal one), thanks to the distillation technique only $N_D = N_T N_v$ inversions are needed. The gain is evident once one notices that

$$N_S^3 \sim 12000, \qquad\qquad N_v = 32, 64, 96. \tag{3.21}$$

It should be pointed out that the suitable value of N_v has to be estimated independently for each lattice and it unfortunately scales with the physical volume N_S^3, therefore for large lattices this method has to be combined with different techniques like the stochastic estimation of the eigenvectors [90, 91].

A meson correlation function can be written as

$$\begin{aligned} C(t_{\rm snk}, t_{\rm src}) =& \langle O_M(t_{\rm snk}) O_M^\dagger(t_{\rm src}) \rangle \\ =& \phi_{\mu\nu}(n, k; t_{\rm src}) \tau_{\nu\alpha}(k, t_{\rm src}; i, t_{\rm snk})\, \phi_{\alpha\beta}(i, j; t_{\rm snk}) \tau_{\beta\mu}(j, t_{\rm snk}; n, t_{\rm src}), \end{aligned} \tag{3.22}$$

where O_M is given in Eq. (3.6). Summation over the source indices (i, j, k, n) pairs and the Dirac indices $(\alpha, \beta, \mu, \nu)$ pairs is implicit. Due to γ_5-hermiticity of the Dirac action

FIGURE 3.4: Connected and disconnected diagrams for a meson correlator.

the perambulator for sink to source can be expressed in terms of the one connecting the two time-slices in the opposite direction:

$$\tau_{\nu\alpha}(k, t_{\rm src}; i, t_{\rm snk}) = \gamma_{5,\alpha\alpha'} \tau^{\dagger}_{\alpha'\nu'}(i, t_{\rm snk}; k, t_{\rm src}) \gamma_{5,\nu'\nu} \ . \tag{3.23}$$

All the details concerning the type of meson interpolator are specified in the function ϕ, which is defined for each time-slice and has indices running over the eigenvectors used for the distillation smearing

$$\begin{aligned} \phi_{\alpha\beta}(i,j;t) &= D_{\alpha\beta} \sum_{\vec{x},\vec{y}} v_d^{i*}(\vec{y}) F_{dc}(\vec{y},\vec{x}) v_c^j(\vec{x}) \\ &\equiv D_{\alpha\beta} \ \widehat{\phi}(i,j;t) \ . \end{aligned} \tag{3.24}$$

The factors D and F represent the Dirac structure and momentum projection or derivative terms related to the quantum numbers of the meson.

The advantage of the distillation approach lies in its versatility. The interpolator structure results completely decoupled from the calculation of the perambulators, which can be therefore computed only once and then used to explore the whole hadron spectrum by recombining them in different Wick contractions and different Dirac structures.

The final meson correlator relative to a connected diagram (Fig. 3.4 (a)) will have the form

$$C_M(t_{snk}, t_{src}) = Tr[\phi(t_{snk})\tau(t_{snk}, t_{src})\phi(t_{src})\tau(t_{src}, t_{snk})], \tag{3.25}$$

while for backtracking loops (Fig. 3.4 (b)) the correlator splits into two independent traces to be evaluate at t_{src} and t_{snk} respectively

$$C_M(t_{snk}, t_{src}) = Tr[\phi(t_{src})\tau(t_{src}, t_{src})]Tr[\phi(t_{snk})\tau(t_{snk}, t_{snk})]. \tag{3.26}$$

For baryon interpolators, which involve combinations of 3-quarks, the ϕ are rewritten in a different form and the contribution to the correlation function are of the type

$$\begin{aligned} C_{\mu\nu}(t_{\rm snk}, t_{\rm src}) &= \langle N_\mu(t_{\rm snk})\overline{N}_\nu(t_{\rm src})\rangle \\ &= \phi_{\mu\alpha\beta\gamma}(i,j,k;t_{\rm snk})\,\tau_{\alpha\alpha'}(i,t_{\rm snk};i',t_{\rm src})\,\tau_{\beta\beta'}(j,t_{\rm snk};j',t_{\rm src}) \\ &\quad \tau_{\gamma\gamma'}(k,t_{\rm snk};k',t_{\rm src})\,\phi^\dagger_{\nu\alpha'\beta'\gamma'}(i',j',k';t_{\rm src})\ . \end{aligned} \tag{3.27}$$

For an interpolator N (without derivatives) as in Eq. (3.10) ϕ assumes the form

$$\begin{aligned} \phi_{\nu\alpha\beta\gamma}(i,j,k;t) &= D_{\nu\alpha\beta\gamma}\sum_{\vec{x}}\epsilon_{abc}v^i_a(\vec{x})v^j_b(\vec{x})v^k_c(\vec{x})F(\vec{x}) \\ &\equiv D_{\nu\alpha\beta\gamma}\widehat{\phi}(i,j,k;t)\ . \end{aligned} \tag{3.28}$$

Again D carries the Dirac structure and F possible total momentum projection factors. The evaluation of correlation functions where meson-baryon states are included, involves terms obtained by the combination of the meson and the baryon contribution. Each correlator can be schematically written in the general form

$$C_M(t_{snk}, t_{src}) = Tr[\phi_M(t_{snk})\phi_B(t_{snk})\tau(t_{snk}, t_{src})\tau(t_{src}, t_{snk}) \tag{3.29}$$

$$\tau(t_{snk}, t_{src})\tau(t_{src}, t_{snk}\tau(t_{snk}, t_{src})\phi_M(t_{src})\phi^\dagger_B(t_{src})], \tag{3.30}$$

where $\phi_M(t)$ and $\phi_B(t)$ are the functions ϕ for meson and baryon respectively. This is how all the results presented in this work have been obtained.

3.5 Lattice artifacts

The hadron spectrum evaluated from lattice calculations cannot be directly compared with experiments. The lattice setup affects the final results in different ways that we now try to summarize.

- Unphysical pion mass: Lattice calculations are usually characterized by large quark masses and therefore large pion masses. It is observed that this leads to an upwards shift of the whole spectrum. The only way to have a complete control of this phenomenon is to perform the same calculation for different m_π and extrapolate to a physical pion mass.

- Continuum limit: A mass measured on the lattice depends on the lattice spacing a

$$M(a) = M_{phys}(1 + O(a^\alpha)), \tag{3.31}$$

where all the quantities are expressed in physical units and the exponent α depends on the action. In the case of Wilson fermions it has been found in [92] that a quadratic contribution has to be expected.

- Finite size: All the lattice simulations are obviously performed at finite volumes. Usually the time extent is chosen big enough so that finite size effects in this direction (i.e., finite temperature effects) are negligible. The limited spatial extent affects the wave functions, which are squeezed in the small volume, leading to a shift of the evaluated mass. In addition the masses are affected by corrections of the order $O\left(\exp(-Lm_\pi)\right)$ due to the leading pion-interaction around the spatial torus.
  It has to be mentioned that sometimes finite volume properties happen to be a useful tool to extract additional information from the calculation. An example is the Lüscher formula (see Chapter 4).

Chapter 4

Multi-particle states on the lattice

Hadron spectroscopy in lattice QCD is a well established research field, but many steps forward still need to be done in order to have a complete understanding of the baryon resonances in the QCD spectrum.
Traditionally in LGT all the particles have been treated as stable states, even though most of the components of the hadron spectrum are not asymptotic states: they are resonances and they decay into two or more lighter particles.
As long as quenched configurations, small volumes and considerably high pion masses are used in the lattice calculations, many resonances are indeed stable states. However when the pion mass becomes low enough to allow the decay, a study of the coupled scattering system is needed in order to obtain results that can be compared with experiments.
Due to practical reasons, lattice simulations are restricted to relatively small volumes, usually few times the interaction length. As a consequence the observation of freely propagating intermediate states is in reality not possible, but an indirect study based on finite size effects can be performed.
In this chapter all the issues concerning the presence of two particle on our lattice will be considered. A method to extract the phase shift from the lattice data (originally proposed by Lüscher) is introduced and a summary of the steps of our study is presented.

4.1 Energy levels in a finite volume

The eigenstates of the Hamiltonian in finite space are the asymptotic states of the field theory (namely the final decay product), and the energy spectrum measured on the lattice is a characteristic of the spatial volume.
In the energy region of the resonance, where the scattering phase shift assumes the value of $\pi/2$, the so-called avoided level crossing can be observed (see Fig. 4.1): the energy

levels of the finite volume system are rearranged in a way that depends on the volume. This phenomenon can serve as a marker for the presence of the resonance.

Lüscher introduced a method to derive the infinite volume phase shift from the study of the two-particle energy spectrum in a finite size system [14, 23–25]. The finiteness of the volume is no more a disadvantage, but an effective tool to extract the phase shift and consequently the resonance mass and width, which can be finally compared with experiments without uncontrolled finite size effects.
After Lüscher's proposal, many other works extended the approach to non zero momentum [19, 32, 35, 36, 93], with the advantage that a larger set of data points can be extracted from one single lattice, overcoming the necessity of using many ensembles with different volumes. Another advantage of using non-zero momentum frames is connected to the fact that the avoided level crossing in P-wave occurs at a much smaller volume, making it more accessible than the $\mathbf{p} = \mathbf{0}$ case (see Fig.(4.2)).
The main disadvantage of studying the scattering of two particles with different masses and non-vanishing momenta is that the evaluation of the phase shift becomes extremely complicated up to the point that a rigorous analysis in certain cases might not be possible: partial waves of different scattering channels and different spin sectors might mix. In these cases what can be done is a qualitative analysis of the measured energy levels.

4.2 Two particles in finite volume

Let us consider a cubic lattice with periodic boundary conditions, spatial volume L^3 and infinite time extent.
The finiteness of the box and its boundary condition require the total momentum of the system to be quantized

$$\mathbf{P_{tot}} = \mathbf{p_1} + \mathbf{p_2} = \frac{2\pi}{L}\mathbf{d}, \qquad \mathbf{d} \in Z^3. \tag{4.1}$$

In the above equation all the quantities are expressed in terms of the laboratory frame (i.e. the lattice box) which moves with a velocity equal to

$$\mathbf{v} = \frac{\mathbf{P_{tot}}}{E}, \qquad \gamma = \frac{1}{\sqrt{1-v^2}}, \tag{4.2}$$

with respect to the center of mass frame (CMF or *). Being able to rewrite all the quantities measured on the lattice in terms of CMF quantities turns out to be crucial for the study of the phase shift δ_l.

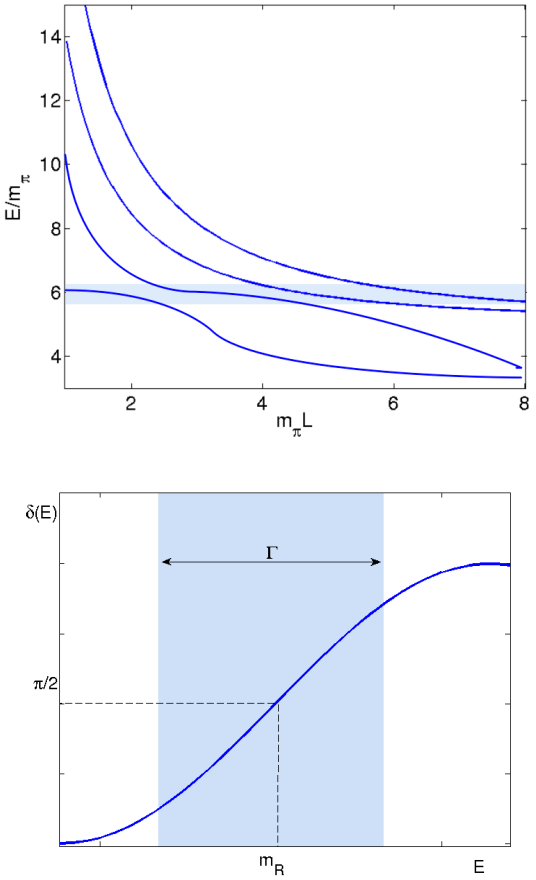

FIGURE 4.1: On the top a sketch of the *avoided level crossing* is presented: in the area influenced by the resonance (blue horizontal band), the levels are distorted. On the bottom we can observe how the phase shift of an elastic scattering behaves in presence of a resonance: $\delta(E)$ rapidly crosses the value $\pi/2$ at the resonance mass.

4.2.1 Non-interacting case

The non-interacting case is trivial: the individual momenta of the two particles independently satisfy the imposed boundary condition with

$$E = \sum_{i=1}^{2} \sqrt{\mathbf{p_i}^2 + m_i^2}, \qquad \mathbf{P_{tot}} = \sum_{i=1}^{2} \mathbf{p_i}, \qquad \mathbf{p_i} = \frac{2\pi}{L}\mathbf{n_i}, \qquad \mathbf{n_i} \in Z^3 \tag{4.3}$$

and the spectrum is computed by summing the single particle energies. The CMF energy squared of the system can be easily estimated as

$$s = E^2 - P^2, \tag{4.4}$$

and it provides relevant information about the energy region interested by the scattering state. As mentioned in (4.1), the presence of the resonance alters the position of the energy levels in its vicinity. In order to reliably extract the phase shift from the energy

levels E_n measured on the lattice, we need these to be in the *interesting kinematic region*, which we define as $m_R \pm \Gamma$ where Γ is the physical width of the resonance and m_R is its mass (it corresponds to the blue band in Fig. 4.1).
This approach will be used in Chapter 5, 6 and 7 in order to justify the choice of the momenta made for the evaluation of the spectrum in S- and P-wave.

Before concluding this section it is useful to write an explicit expression for the quantized momenta in the CM frame, since they will define the mesh that determines the residual discrete symmetries in the non-vanishing total momentum case and they will enter the final formula for the evaluation of the phase shift

$$\mathbf{p}^* = \mathbf{p_1}^* = -\mathbf{p_2}^*, \tag{4.5}$$

using basic Lorenz transformations

$$\mathbf{p}^* = \gamma^{-1}\mathbf{p_1} - \mathbf{v}E_1^* = \gamma^{-1}(\mathbf{p_1} - \gamma\frac{2\pi}{L}\frac{E^*}{2E}[1 + \frac{m_1^2 - m_2^2}{E^{*2}}]\mathbf{d}) = \gamma^{-1}(\mathbf{p_1} - \frac{1}{2}A\mathbf{P_{tot}}), \tag{4.6}$$

where we defined the coefficient A as

$$A = 1 + \frac{m_1^2 - m_2^2}{E^{*2}}, \tag{4.7}$$

which differs from 1 in the case of two particles with different masses and it plays a relevant role when studying the symmetries of the system and the transformation properties of the interpolators (see Section 6.4).
If we define the CMF momenta in terms of the dimensionless quantity $\mathbf{q}$

$$\mathbf{p}^* = \frac{2\pi}{L}\mathbf{q}, \tag{4.8}$$

then the quantization constraint on $\mathbf{q}$ (i.e. the allowed values in the box for the non interacting case) is

$$\mathbf{q} = \mathbf{r} \qquad \text{with} \qquad \mathbf{r} \in P_d = \left\{\mathbf{r} | r = \gamma^{-1}(\mathbf{n} - \frac{1}{2}A\mathbf{d})\right\}, \qquad \mathbf{n} \in Z^3, \tag{4.9}$$

where P_d is the set of vectors which define the mesh and the consequent symmetries.

4.2.2 Interacting case

In case of two interacting particles the picture changes: the energy levels are shifted due to the presence of the potential $V(\mathbf{x}^*)$ which depends on the relative distance between the two particles.

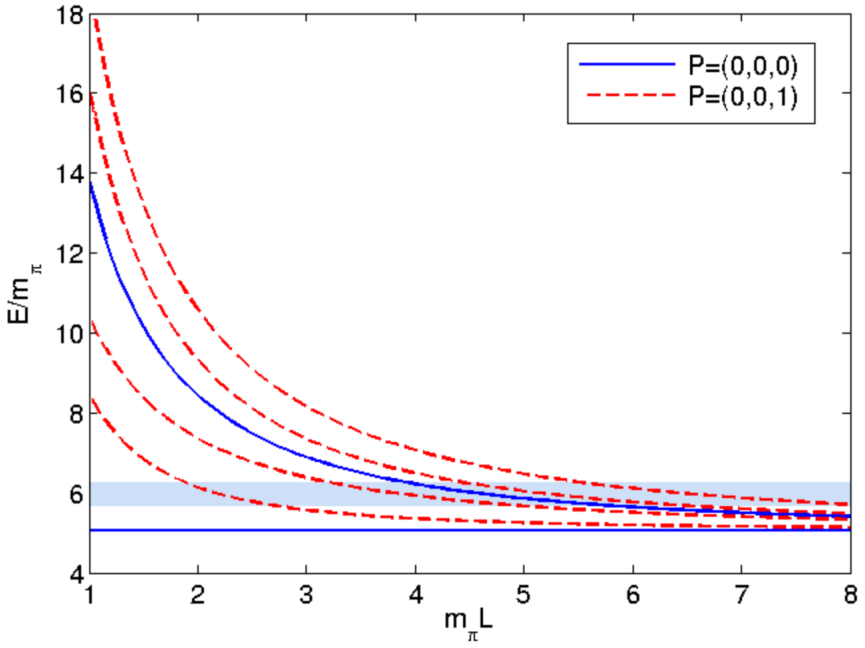

FIGURE 4.2: The energy levels of the non-interacting pion-nucleon system in different momentum setups calculated on our lattice: $m_\pi = 266$ MeV, $m_\pi = 1080$ MeV, $a = 0.1239$, $L = 16$. In blue the energy levels for the total momentum $\mathbf{P} = \mathbf{0}$ and in red the energy levels corresponding to $\mathbf{P} = (0, 0, 1)$. The blue band crossing the plot horizontally represents the location of the expected Roper resonance (shifted up w.r.t. the physical one due to the unphysical pion mass). It is clear that a non-rest frame is needed if one is interested in exploring the positive parity excitation of the nucleon: the spectrum is more dense, increasing the probability of hitting the *interesting region*.

In QCD the interacting potential is not known and the eigenstates of the Hamiltonian

$$H\psi(x_1, x_2) = E\psi(x_1, x_2) \tag{4.10}$$

cannot be calculated ab initio. However some considerations on the scattering theory can lead to a relation between the scattering phase shift and the spectrum evaluated in a box, based on the constraints imposed by the boundary condition.

The traditional approach to a scattering study consists in considering the initial and final states as asymptotically free states. We assume that in the exterior region the potential vanishes

$$V(\mathbf{x}^*) = 0 \qquad \text{for} \qquad |\mathbf{x}^*| > R \qquad \text{and} \qquad R < L/2, \tag{4.11}$$

where we required the interaction range to be considerably smaller than the lattice size. In this region the solution of the Helmholtz equation provides a description of the scattering without interaction

$$(\nabla^2 + p^{*2})\phi_{CM}(\mathbf{x}^*) = 0 \qquad\qquad x^* > R\,, \tag{4.12}$$

$$E^* = \sqrt{(p^*)^2 + m_1^2} + \sqrt{(p^*)^2 + m_2^2} = \gamma^{-1} E \,. \tag{4.13}$$

The solution $\phi_{CM}(\mathbf{x}^*)$ will depend on the phase shifts $\delta_l(p^*)$ between the initial and the final state of the scattering process. The phase shift encodes the unknown information concerning the interaction.

In a finite box the solution $\phi_{CM}(\mathbf{x}^*)$ has to satisfy the **d**-periodic boundary conditions (a derivation can be found in [35])

$$\phi_{CM}(\mathbf{x}^*) = (-1)^{A\mathbf{nd}} \phi_{CM}(\mathbf{x}^* + \gamma \mathbf{n} L) \qquad \mathbf{n} \in Z^3 \,, \tag{4.14}$$

where **d** is the normalized total momentum. Solutions to this condition have been computed in [25], [32], [34] and can be re expressed as a condition on the phase shift (which ϕ depends on).
According to [25] the scattering phase shifts δ can be evaluated solving the determinant equation for meson or baryon resonances

$$\det(M - \cot \delta) = 0 \,, \tag{4.15}$$

where for simplicity all the indices have been suppressed. This equation relates the phase shift δ in the infinite volume to the energy levels of the lattice Hamiltonian in a finite cubic box. The matrix M and the matrix $\cot(\delta)$ have the form

$$M_{lm,l'm'} = M^{\mathbf{d}}_{lm,l'm'}(q^2) \,, \qquad \cot(\delta)_{lm,l'm'} = \cot(\delta_l(p^*))\delta_{ll'}\delta_{mm'} \tag{4.16}$$

and the indices (l, m) run over different partial waves (l) and spins (m). It has to be noticed that in case of small p^* the high partial waves can be neglected since $\delta(p^*) \propto (p^*)^{2l+1}$. In general only S, P and D wave are considered, however in many channels D-waves are not present in the lower part of the spectrum.

The matrix M can be evaluated once the symmetry group and the specific irreducible representation involved are known, for each different little group of symmetry defined by the deformed mesh due to the non-vanishing total momentum. The elements of M are normally expressed in terms of

$$w_{lm} = \frac{1}{\pi^{3/2}\sqrt{2l+1}} \frac{1}{\gamma q^{l+1}} Z^{\mathbf{d}}_{lm}(1; q^2) \,, \tag{4.17}$$

where the modified zeta functions are defined as

$$Z^{\mathbf{d}}_{lm}(s; q^2) = \sum_{r \in P_d} \frac{\mathcal{Y}_{lm}(\mathbf{r})}{(r^2 - q^2)^s} \tag{4.18}$$

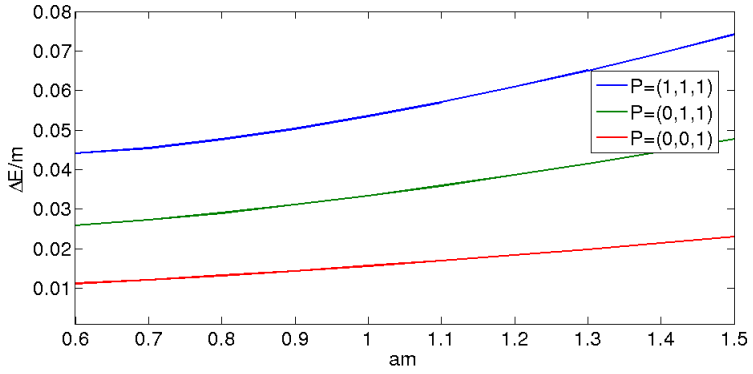

FIGURE 4.3: The difference between the energy evaluated via Eq. (4.3) and Eq. (4.20) is presented as a ratio over the mass. On the horizontal line the mass is given in lattice units. The selected range covers the energy region where the nucleon excited states are expected: between 950 and 2300 MeV. The discrepancy lies below 8% for most of the cases, being therefore comparable to the statistical error of our calculations.

and

$$\mathcal{Y}_{lm}(\mathbf{x}) = x^l Y_{lm}(\theta\phi)\,, \tag{4.19}$$

with Y_{lm} being the spherical harmonics. The evaluation of the coefficients can be found in [35, 36].

The quantization condition of the momenta in the finite box establishes a relation between the phase shift [23] and the spectrum of the finite size system which holds up to $O\left(e^{-m_\pi L}\right)$. Therefore a strict requirement for this setup to work is that $m_\pi L >> 1$. It also has to be reminded that the current considerations are for a finite box in a continuum theory and the lattice artifacts might appear as $O(a^2)$ corrections. A dispersion relation different from Eq.(4.3) should be used when large momenta are involved. For Wilson fermions we use [32]

$$\cosh E(\mathbf{p}) - \cosh m = \sum_{i=1}^{3}(1 - \cos p_i) \tag{4.20}$$

and we note that the results in our setup become sensitive to this distinction only for high masses and high momenta, as shown in Fig. 4.3.

4.3 Consequences of $P_{tot} \neq 0$

In case of non-zero total momentum, the lattice mesh is distorted due to relativistic effects and part of the cubic symmetry is broken. The residual symmetry group is called little group and it can be determined once $\vec{P}_{tot}$ is known.
The symmetry group plays an important role for two main reasons:

- We require the interpolators to transform under a well defined irreducible representation of the symmetry group of our system in order to mimic the properties of the corresponding operators in the continuum. If the symmetry group changes due to $\vec{P}_{\text{tot}\neq 0}$, then a redefinition of the interpolators might be needed.
- We mentioned that the evaluation of M and the final form of Lüscher's formula depend on the symmetries of the system, therefore we will have different equations to be solved for different total momenta.

When $\vec{P}_{\text{tot}}$ is non zero (see Chapter 6), a projection of the interpolators to a definite spin and partial wave sector is not possible. This brings complications in the evaluation of the spectrum: extracting many excited states is a delicate procedure and the superposition of different sectors of the QCD spectrum might affect the possibility of identifying the states that are measured.

4.4 Conclusions

Let us summarize the steps that have to be followed in order to guarantee a coherent treatment of the two particle system on our lattice and the possibility to obtain information on the resonances.

- The presence of a resonance affects the distribution of the energy levels in a finite box and generates the *avoided level crossing* phenomenon. This happens in the vicinity of the resonance, while the rest of the spectrum is left invariant. It is important to identify the *interesting region* to make sure that we are exploring the correct area of the spectrum.
- Due to the kinematics of the available lattice, the momenta are quantized and very often the smallest momentum is already considerably large. As a consequence the two particle energy levels are largely spaced from each other. This reduces enormously the chances of hitting the *interesting region*. Taking into account $\vec{P}_{\text{tot}} \neq 0$ helps in making the two particle spectrum more dense and increase the number of possible choices. The disadvantage is that systems in non-rest frames have reduced symmetries and this has to be carefully taken into account.
- Our task is to compute correlation matrices of systems that include both one and two particle states. We require that the two interpolators have the same quantum numbers and transform under the same irreducible representation. Constructing the correct operator is essential for a reliable extraction of the spectrum.

Setup

All the lattice simulations are performed using an ensemble of 280 approximately independent gauge configurations with $n_f = 2$ mass degenerate dynamical quarks of improved Wilson-Clover type, with gauge links smeared using one level of normalized hypercubic smearing (nHYP smearing). The valence u/d quarks have the same mass as the sea u/d quarks. The pion mass is $m_\pi = 266$ MeV and the $16^3 \times 32$ lattices have spatial extent of 1.98 fm with $Lm_\pi \sim 2.68$ (for details see Table 4.1 and [17, 20]).
These configurations have been generated for the study of re-weighting techniques [66, 67] and they have been generously provided by the authors.

$N_S^3 \times N_T$	β	a[fm]	L[fm]	$L\,m_\pi$	#configs	m_π[MeV]
$16^3 \times 32$	7.1	0.1239(13)	1.98	2.68	280	266(3)(3)

TABLE 4.1: Parameters of the configurations used for the current study. $N_S^3 \times N_T$ denote the volume of the lattice, and $L = N_S a$ is the spatial size in physical units.

Two main consequences of this choice have to be noticed:

- The mass of the pion is unphysical (roughly 130 MeV higher than the physical one), therefore we expect all the estimated masses to be shifted upwards with respect to their experimental values.
- The value $Lm_\pi \sim 2.7$ is relatively small and might produce finite size effects.

Both the finite size effects and the consequences of working with an unphysical pion mass cannot be identified in this study, since only one set of lattice configurations is available.

Chapter 5

N^*: Pion - Nucleon scattering in S-wave

The negative parity sector of the nucleon spectrum couples to the pion-nucleon system in S-wave and isospin $I = 1/2$. Lattice simulations of $N\pi$ scattering have been performed for two flavors of mass degenerate light quarks.
The novelty of this calculation is represented by the fact that for the first time meson-baryon (4+1)-quark interpolators enter the correlation matrix together with the standard 3-quarks baryon operators. The distillation method and the variational analysis are used to determine the energy levels of the spectrum in the specified (I, J^P) sector and a clearer picture of the negative parity nucleon spectrum emerges.
The results of the study published in [94] are presented in this chapter.

5.1 N^- sector

The negative parity N^* channel becomes quickly inelastic (see, e.g., [95–98]). According to the Particle Data Group [2]

$N^*(1535)$	$N^*(1650)$
$\longrightarrow N\pi \quad (35-55)\%$ $\longrightarrow N\eta \quad (10-42)\%$	$\longrightarrow N\pi \quad (50-90)\%$ $\longrightarrow N\pi \quad (5-15)\%$ $\longrightarrow \Lambda K \quad (3-11)\%$
$\longrightarrow N\pi\pi \quad (1-10)\%$	$\longrightarrow N\pi\pi \quad (10-20)\%$

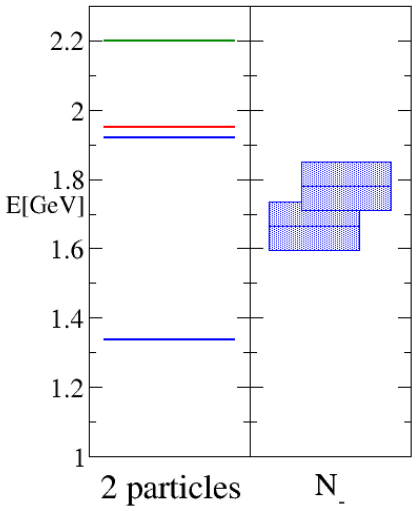

FIGURE 5.1: The energy levels of two-particle states estimated with the parameters of our lattice are compared with the mass of the two resonances N^* which have been shifted up of $\Delta E \sim 130$ MeV according to the expected behavior. In blue the $N\pi$ S-wave states: both particles at rest and with back to back unit momenta. In addition $N\eta$ (red) and ΛK (green) have been plotted. All the energies have been estimated starting from the values of m_π and m_N measured on our lattice.

the main decay channel is $N\pi$, followed by $N\eta$ and ΛK for for $N^*(1650)$. In addition the inelastic channel $N\pi\pi$ plays an important role for both the resonances. For a calculation with a fine lattice and physical quark masses all these channels should be included, but this is not the case in our setup.

On our lattice (see section 4.4), where only two degenerate valence quarks are present, the pseudoscalar meson η manifests itself in one state with a mass larger than 800 MeV [99, 100]. In addition Λ and K would have masses larger than 1600 MeV and 600 MeV respectively [101]. With the parameters of the lattice used in the current study the before mentioned channels would have too high threshold to be involved in the decay of N^* and will be therefore discarded. The same argument holds for $N\pi\pi$ and for any S-wave which involves non-vanishing momenta such as $N(\mathbf{p})\pi(-\mathbf{p})$ (see Fig. 5.1).

Thus we consider the neglection of such interpolators safe: the energies of these two particle states are far from the energy region interested by N^* and their absence in the calculation is not affecting a reliable interpretation of the measured states.

5.2 Interpolators

In the current chapter our attention is focused on $J^P = 1/2^-$ and $I = 1/2$: the N^- sector. In order to guarantee the effectiveness of the variational method, we are required to compute a correlation matrix where only the interpolators with the correct quantum numbers are taken into account. For this reason the construction of the $N\pi$ interpolator requires special care.

For the charged nucleon 3-quark interpolator at zero momentum we use the operator

$$(N_{\pm}^{(i)})_{\mu} = \sum_{\vec{x}} \epsilon_{abc} \left(P_{\pm}\,\Gamma_1^{(i)}\,u_a(\vec{x})\right)_{\mu} \left(u_b^T(\vec{x})\,\Gamma_2^{(i)}\,d_c(\vec{x})\right) \tag{5.1}$$

on every given time slice. The neutral nucleon has the same form, but a different quark composition: u, u, d is replaced by d, u, d. The combination (Γ_1, Γ_2) can assume the three values $(\mathbb{1}, C\gamma_5)$, (γ_5, C) and $(\mathrm{i}\mathbb{1}, C\gamma_t\gamma_5)$ for $i = 1, 2, 3$. $P_{\pm} = \frac{1}{2}(1 \pm \gamma_t)$ denotes the parity projector, C is the charge conjugation matrix and γ_t the Dirac matrix in the time direction. The projection onto definite zero momentum is guaranteed by the sum over all points of each time slice. In addition, summation over the color indices a, b, c and the implicit Dirac indices is implied. No isospin symmetrization is implemented since all the quark fields are subject to the same smearing (see Appendix C).
Since the distillation approach is implemented (see Section 3.4), all the quark sources are additionally smeared combining a different number N_v of eigenvectors. For the 3-quark nucleon interpolators we use $N_v = 32$ and $N_v = 64$ (corresponding to different smearing widths) for each of the three $N^{(i)}$, obtaining a total of six operators.

The meson-baryon interpolators are built starting from the single particle interpolators $\left\{\pi^{\pm}, \pi^0, N^{(i)}\right\}$, which have to be appropriately projected onto the right parity and isospin channel.

The pion interpolators read

$$\begin{aligned} \pi^+(\vec{p}=0) &= \sum_{\vec{x}} \overline{d}_a(\vec{x})\gamma_5 u_a(\vec{x}) \,, \\ \pi^0(\vec{p}=0) &= \sum_{\vec{x}} \frac{1}{\sqrt{2}} \left(\overline{u}_a(\vec{x})\gamma_5 u_a(\vec{x}) - \overline{d}_a(\vec{x})\gamma_5 d_a(\vec{x})\right) \,, \end{aligned} \tag{5.2}$$

where summation over the color index a and the Dirac indices is implied.

The simulations are performed considering the $N\pi$ system in the rest frame where the leading S-wave contribution is expected to come from the interpolator with both particles at rest, namely

$$(N\pi)^{(i)}(\vec{p}=0) = \gamma_5 N_+^{(i)}(\vec{p}=0)\pi(\vec{p}=0) \,, \tag{5.3}$$

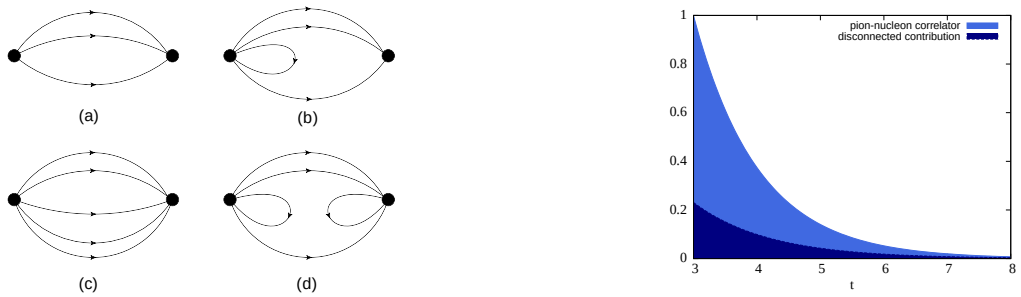

FIGURE 5.2: Left: Different types of contributions included in the correlation matrix. Connected diagrams (a),(c); partially disconnected diagrams (b), (d).
Right: Normalized contribution of the disconnected diagrams (d) to the total correlation function $\langle N\pi|N\pi\rangle$.

where $i = \{1, 2, 3\}$, $N_+^{(i)}$ denotes the positive parity nucleon and the factor γ_5 ensures that the $N\pi$ interpolators transform as N^- under parity transformations (for details about the effects of parity transformations on the interpolators see Appendix B).
In the context of the distillation approach we smear every quark source of the $N\pi^{(i)}$ interpolators with $N_v = 32$ so that, thanks to the different Dirac structures, three two-particle interpolators are included into the correlation matrix .

One last step is required in order to obtain the final form for the $N\pi$ interpolator: the isospin projection.
The $N\pi$ system is a superposition of isospin $\frac{1}{2}$ and $\frac{3}{2}$ states and, in order to select the $N^-(I = \frac{1}{2})$ states we project to isospin $\frac{1}{2}$ by choosing the combination (see Appendix C)

$$O_{N\pi}(I = \frac{1}{2}, I_3 = \frac{1}{2}) = p\pi^0 + \sqrt{2}\, n\pi^+ \,, \tag{5.4}$$

with p and n denoting the charged and the neutral nucleon according to (5.1).

5.3 Evaluation of the correlation matrix

Including the (4+1) quark interpolators provides new information on the states of the nucleon spectrum in the negative parity channels, but it requires the evaluations of partially disconnected diagrams (see Fig. 5.2, LHS) which are computationally extremely expensive: for a statistically significant computation of the latter, evaluations at many different t_{snk} and t_{src} turn out to be necessary.

The relevance of these diagrams is however seen by a simple comparison of the disconnected vs connected contributions (see Fig. 5.2, RHS): the contribution of diagrams involving backtracking loops over the total correlator $\langle N\pi|N\pi\rangle$ is between 20 and 30%, so it cannot be neglected.

Thanks to the distillation method, which allows to reorganize the terms in the correlation function and save a considerably amount of CPU time, we explicitly evaluate all the diagrams (i.e. Wick contractions) which contribute to the total correlator (see Appendix D) including $\langle N|N\rangle$, $\langle N\pi|N\rangle$ and $\langle N|N\pi\rangle$.

5.4 Effective masses: N

The spectrum of the positive and negative parity nucleon is first determined via the analysis of a set of six 3-quarks interpolators with the variational method, as discussed in Section 3.3.

$$\begin{aligned} &\mathcal{O}_1,\, \mathcal{O}_2,\, \mathcal{O}_3 = N^{(1)},\, N^{(2)},\, N^{(3)} && \text{with } N_v = 32\ , \\ &\mathcal{O}_4,\, \mathcal{O}_5,\, \mathcal{O}_6 = N^{(1)},\, N^{(2)},\, N^{(3)} && \text{with } N_v = 64, \end{aligned} \tag{5.5}$$

where the parity is defined performing a parity projection (see Appendix B).

5.4.1 N^+ spectrum

In the positive parity sector we can extract at least two stats with good reliability. The first state is without doubts the ground state nucleon and it couples exclusively to $N^{(1)}$ type operators. It is evident from the effective masses plateau behavior (Fig. 5.3) that the signal is stable and its energy can be extracted with high precision, being independent of the choice of one or two exponential fit. Our best estimate for the ground state nucleon is $a\,m_N = 0.672(4)$, which is equivalent to $m_N = 1068(6)$ MeV in physical units. Due to the fact that only one lattice ensemble is available, an extrapolation to physical pion mass is not possible. However this result is in agreement with other studies which use configurations with similar parameters [101]. The mass of the nucleon on this specific lattice is ~ 130 MeV higher than the physical one, following the behavior of the pion mass. Based on this consideration, we will expect the whole spectrum to be shifted up of roughly the same quantity.

The first excited state observed in this sector mainly couples with $N^{(2)}$ and it is considerably higher than the expected Roper resonance. This observation is shared by other studies (see, e.g., [6, 9]) but disputed [7, 42]. One of the reasons of this result may be connected to the nature of the Roper resonance and it might suggest that different interpolators should be included in order to enhance the coupling with this state.
This possibility will be discussed in Chapter 6.

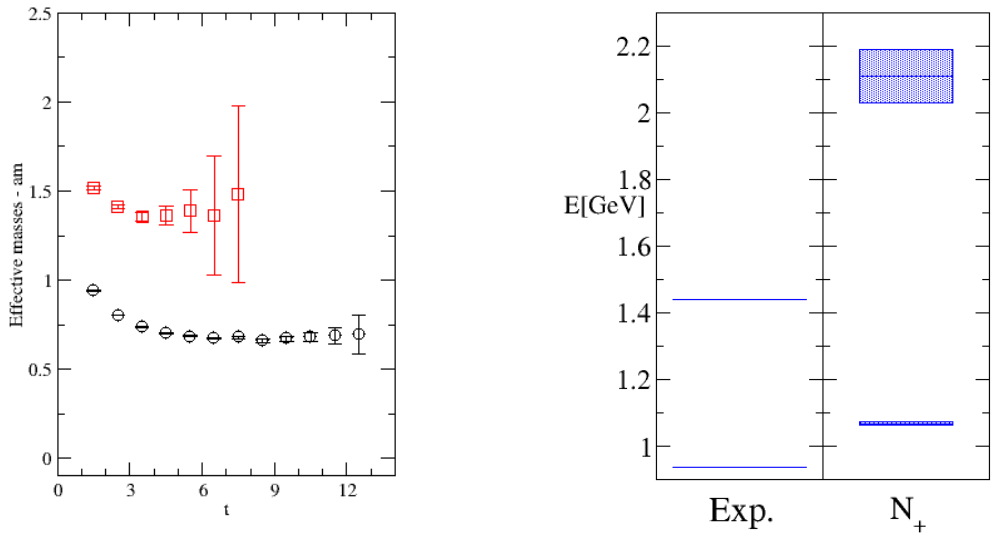

FIGURE 5.3: LHS: The effective energy values for the $N(\frac{1}{2}^+)$ channel (with 3-quark interpolators) in lattice units. RHS: Comparison between the experimental values of the N^+ low-lying spectrum and the results obtained in this study.

5.4.2 N^- spectrum

The negative parity sector of the nucleon spectrum can also be computed from a correlation matrix that includes only 3-quark baryon interpolators.

Let us first consider results for the subset of 3-quark interpolators $\{\mathcal{O}_1 - \mathcal{O}_6\}$: it seems that including the interpolators of type $N_-^{(3)}$ does not improve the quality of the diagonalization results. We therefore use only the subset $\{(\mathcal{O}_1, \mathcal{O}_2, \mathcal{O}_4, \mathcal{O}_5)\}$.
We reproduce the usual (see, e.g. [9, 10]) pattern of energy levels (see left hand plot of Fig. 5.6): we observe two energy levels: at $1.359(43)$ GeV (exponential fit, fit range $6-10$) and $1.709(29)$ GeV (fit range $4-9$). The situation is shown in Fig. 5.7 (middle). This picture might, at first sight, look satisfying: in the experiments two resonances are detected in this sector, $N(1535)$ and $N(1650)$ [2]. However some details must be noticed: in Fig. 5.7 (two leftmost columns) we compare the value of the state measured on the lattice in physical units, with the corresponding experimental values.
The lowest measured energy state lies below the experimental value and very close to the non-interacting $N\pi$ state (red dashed line in the rightmost column).
In addition it has been observed in [101] that towards small pion masses the lower

level moves close to the expected $N\pi$ threshold and thus unexpectedly lower than the experimental mass of $N^*(1535)$.
A possible explanation for the observed spectrum might be that 3-quark interpolators are not sufficient to describe the physics of the system: the resonant nature of the N^* states is not taken into account and the inclusion of $N\pi$ interpolators might completely change the picture.

5.5 Effective masses: $N\pi$

The masses of the free pion and the ground state nucleon $N(\frac{1}{2}^+)$ have to be estimated with very high precision in order to perform the subsequent analysis. For the gauge configurations used here the pion was carefully studied in [17, 20]. We use the result of that analysis: the pion mass in lattice units corresponds to $a\,m_\pi = 0.1673(2)$.

In the following sections the results of the two particle system are presented.

5.5.1 Pion and nucleon, non-interacting

In order to test the method and the technical basis which are used to study the coupled $(N, N\pi)$ system, we first study the pion-nucleon system in a non-interacting regime.
We evaluate the correlation function

$$C(t, t_0) = \langle O_{N\pi}(t) | O_{N\pi}(t_0) \rangle, \tag{5.6}$$

using only the two diagrams (Appendix D, diagrams D1,D2) where the two particles propagate independently, i.e., the quark lines exclusively connect quarks that belong to the same hadron.
Fig. 5.4 represents a valid consistency check: the non-interacting pion-nucleon system behaves exactly as expected: the effective masses computed using Eq.(5.6) converge to the same energy level which represents the value of the pion and the nucleon masses naively summed. We can be confident that the chosen theoretical setup is well understood and it guarantees a good control of the physical problem.

In Fig. 5.5 we compare the energy levels obtained from a single particle study in the N^- energy levels: the latter appears to be close enough to the first N^- measured level to allow doubts concerning the nature of this state. On the right hand side of the figure we show the eigenvector composition of these two states.

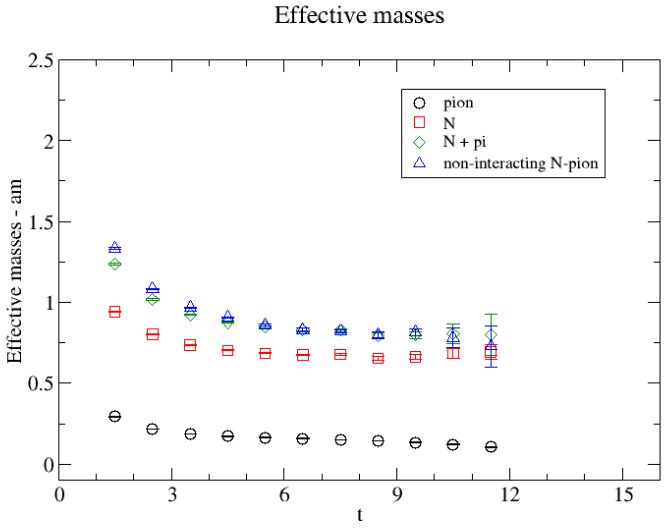

FIGURE 5.4: The effective energy values for the pion and the ground states nucleon, compared to the values computed from the evaluation of Eq.(5.6) (blue triangles). The green diamonds represent the naive sum of the effective masses of the pion and the nucleon for each time separation. All values are expressed in lattice units.

5.5.2 Interacting $N\pi$ system

The final step consists in the computation of the full correlation matrix for the following operators:

$$\begin{aligned} &\mathcal{O}_1,\, \mathcal{O}_2,\, \mathcal{O}_3 = N_-^{(1)},\, N_-^{(2)},\, N_-^{(3)} && \text{with } N_v = 32\,, \\ &\mathcal{O}_4,\, \mathcal{O}_5,\, \mathcal{O}_6 = N_-^{(1)},\, N_-^{(2)},\, N_-^{(3)} && \text{with } N_v = 64\,, \\ &\mathcal{O}_7,\, \mathcal{O}_8,\, \mathcal{O}_9 = O_{N\pi}^{(1)},\, O_{N\pi}^{(2)},\, O_{N\pi}^{(3)} && \text{with } N_v = 32\,. \end{aligned} \tag{5.7}$$

with the definition from (5.1) and (5.3). The results are presented in Fig. 5.6.
The right hand plot shows the effective energy levels resulting from the analysis of a (7×7) correlation matrix, where $\{\mathcal{O}_1, \mathcal{O}_2, \mathcal{O}_4, \mathcal{O}_5, \mathcal{O}_7, \mathcal{O}_8, \mathcal{O}_9\}$ are included. The outcome of the exponential fits and the corresponding energy levels in physical units are listed in Table 5.1.
On the left hand side of Fig. 5.7 the effective masses extracted from the single particle analysis are shown for a comparison.
When the two particle interpolators are included in the study, the energy levels appear rearranged. A new plateau appears in the energy region of interest and the signals are affected by consistently less fluctuations, allowing a more reliable extraction of the energy values.

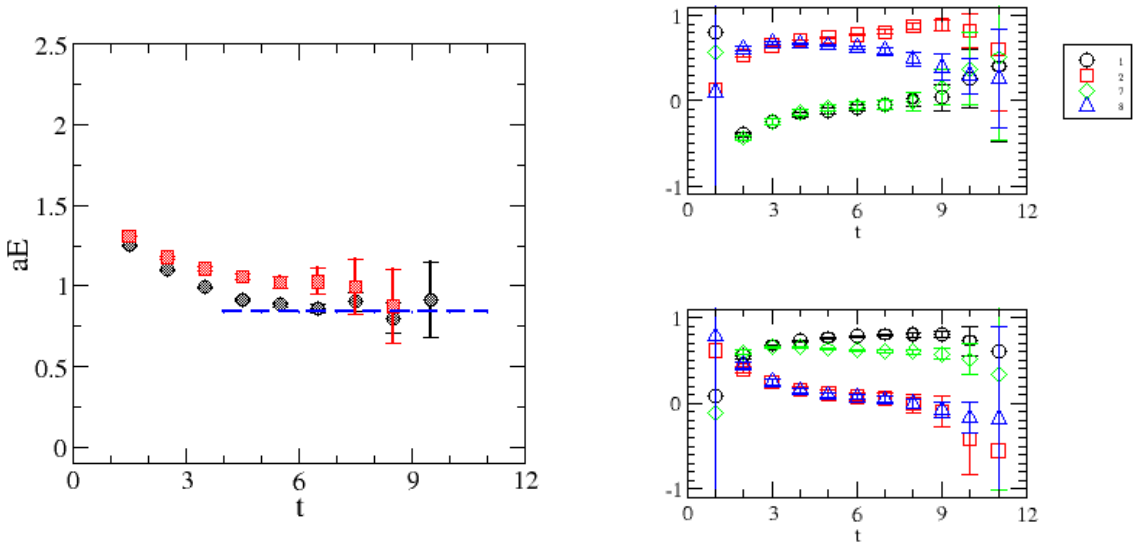

FIGURE 5.5: The effective energy values for the $N(\frac{1}{2}^-)$ channel (with 3-quark interpolators) in lattice units. The blue line represents the energy value of the non-interacting pion-nucleon system. On the right hand side the eigenvector composition of these two states is shown.

level n	fit range	$a\,E_n = a\,\sqrt{s}$	$E = \sqrt{s}$ [GeV]	$\frac{\chi^2}{d.o.f.}$	$a\,p^*$	δ [degrees]
1	6-12	0.800(5)	1.272(8)	6.12/5	0.0985(57) i	68(59)i
2	4-8	1.045(19)	1.662(30)	2.46/3	0.2726(155)	89(9)
3	4-8	1.127(18)	1.792(29)	0.67/3	0.3362(134)	47(10)

TABLE 5.1: Final results for the lowest three energy levels of the coupled $N\pi$ system with the interpolators $\mathcal{O}_1, \mathcal{O}_2, \mathcal{O}_4, \mathcal{O}_5, \mathcal{O}_7, \mathcal{O}_8, \mathcal{O}_9$. For the values given in GeV we use the lattice spacing $a = 0.1239$ fm (Sommer parameter $r_0 = 0.48$ fm).

In order to clarify the features emerging from the two particle system study, we now focus on Fig. 5.7: the experimental values (left) of the N^* are compared to the results of the 3-quark interpolators case (middle) and the combined analysis of 3 and (4+1) quark interpolators (right).

The results of the central column display a clear discrepancy with the experimental values, while the (4+1) quark study shows a much more reliable picture with three states which can be identified as the two-particle state, $N(1535)$ and $N(1650)$ respectively. The lowest level lies slightly below threshold, a feature typical for attractive S-wave [20, 21]. As we explained in Chapter 4 the levels distribution is modified by the interaction and the presence of a resonance.

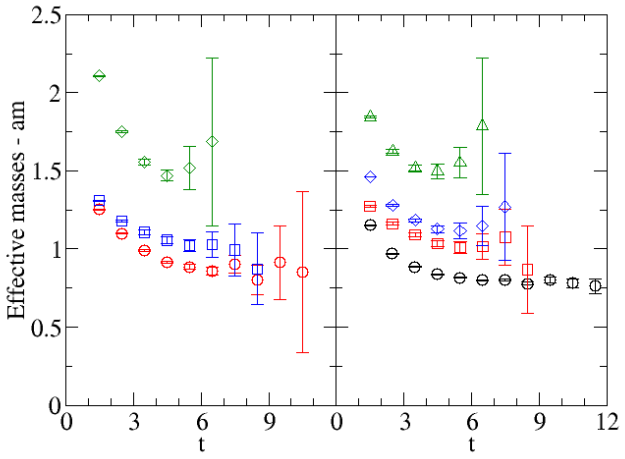

FIGURE 5.6: Effective energy values without $N\pi$ contribution (Left) and including $N\pi$ interpolators (Right). The horizontal broken line indicates the threshold value $m_N + m_\pi$. All the masses are given in lattice units.

The next two levels are characterized by energies lying approximately 130 MeV above the physical resonance positions of $N^*(1535)$ and $N^*(1650)$, which agrees with the behavior of the ground state nucleon. This interpretation for the measured spectrum is also supported by the analytic analysis which will be presented in Section 5.6 and Fig. 5.9, where a single elastic resonance parameterization has been used, shows excellent agreement for the lowest two energy levels.

A further inspection of the states can be performed studying the eigenvectors. The eigenvectors describe the coupling of each state with the different interpolators. Ideally each state should mainly couple to only one interpolator and the fit range for each state should be chosen so that the eigenvector composition remains stable: in this way one can be sure to identify one definite state.
Once it is known which are the interpolators that a certain state couples with, a physical interpretation of the state can be carried out.

Fig. 5.5 shows that when only 3-quark interpolators are used, each measured state has contributions from different interpolators, some of which vanish just at large time scales, while the picture changes when $O_{N\pi}$ are included: Fig. 5.8 shows the eigenvector components of the three lowest eigenstates. Note that the eigenvectors have unit norm, but the absolute normalization of the (4+1)-quark operators compared to the 3-quark ones is not known. For this reason only the comparison between different levels holds a physical meaning.

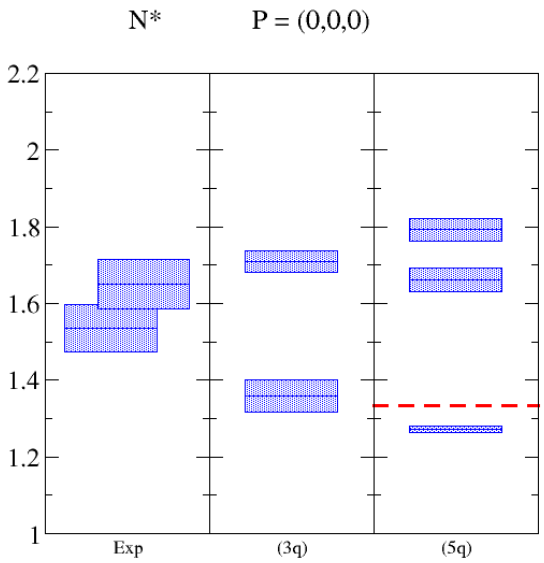

FIGURE 5.7: Comparison of the energy levels. Left: physical mass values (experiment). Middle: result when using only 3-quark interpolators. Right: result when including pion-nucleon interpolators.

The $\mathcal{O}_{N\pi}$ contribution to the ground state is significantly larger than the higher levels, supporting the identification of this state with the two-particle state.
The second state is clearly dominated by $N_-^{(2)}$ type interpolators, with a contribution from two particle $N_-^{(2)}\pi$ interpolators.
The third state is predominantly a $N_-^{(1)}$ state.

The comparison of Fig. 5.7 combined with the newly acquired knowledge on the composition of each state suggests that the incompleteness of the picture arising from the 3-quark analysis is due to the incompleteness of the interpolator basis. It seems that the two lowest states of the 3-quark system interpolate between the three lowest states of the complete system. This would explain the instability of the signal and the mixed eigenvector composition of the states. A realistic picture can be reconstructed only when the $N\pi$ system is explicitly taken into account.

5.6 Interpretation of the energy levels

As discussed in Chapter 4, the Lüscher type approach allows to extract the values of the phase shift in the continuum, starting from the spectrum of a finite volume system, but Eq. (4.15) can be inverted and used to predict the expected levels, once a parametrization for the phase shift is available.

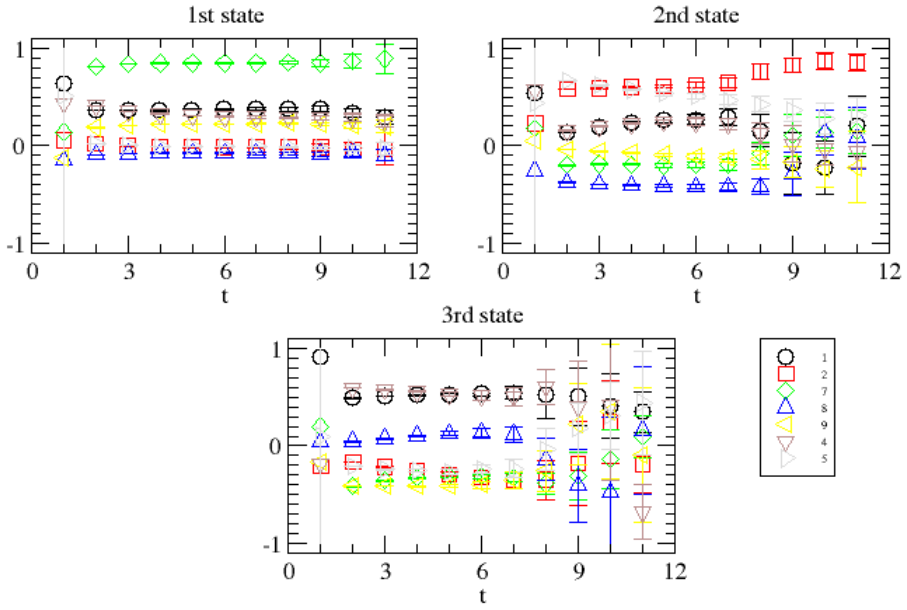

FIGURE 5.8: The (normalized) eigenvector components for the lowest three observed eigenstates to be compared with the eigenvectors of the states computed in the 3-quark sector (Fig. 5.5). In the legends the operator numbers according to Eq. (5.7) are given.

.

For each energy value that is measured on our lattice we compute the total energy of the system as

$$E = \sqrt{s} = \sqrt{(p_N + p_\pi)^2} = \sqrt{p^{*2} + m_\pi^2} + \sqrt{p^{*2} + m_N^2} \tag{5.8}$$

and we extract the momentum $p^* = |\mathbf{p}^*|$ in the CMF with

$$p^{*2} = \frac{[s - (m_N + m_\pi)^2][s - (m_N - m_\pi)^2]}{4s} \,, \tag{5.9}$$

which will be used to relate the discrete spectrum to the phase shift.

For a system of non-interacting pions and nucleons and a given lattice size, the energy levels can be straightforwardly computed (dotted lines in Fig. 5.9).
In presence of interaction these levels are modified and their behavior is encoded in the Lüscher formula under the constraint of elastic region and localized interaction [14, 23–25]

$$\tan\delta(q) = \frac{\pi^{3/2} q}{\mathcal{Z}_{00}(1; q^2)} \qquad \text{for } \mathbf{P} = 0 \,, \tag{5.10}$$

where q is the dimensionless product of the momentum and the spatial lattice size defined in Eq. (4.9). The generalized zeta functions Z_{lm} are defined in Eq. (4.18) and computed in [24].

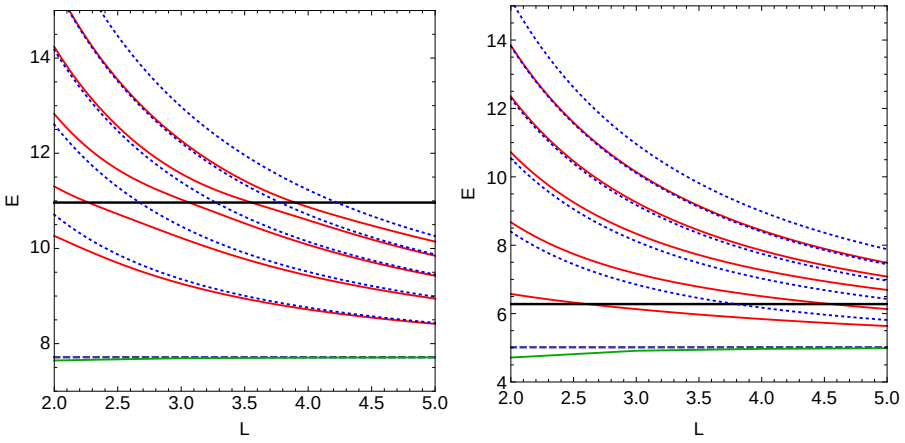

FIGURE 5.9: Lowest energy levels vs. the spatial lattice size (both in units of the pion mass). Left: physical pion, nucleon and $N^*(1535)$ masses, comparing the non-interacting levels (dotted) with the levels distorted due to interaction (full lines); the broken horizontal line indicates the threshold, the horizontal thick line the $N^*(1535)$-mass; the N^* is parametrized as an elastic resonance with a decay width of 150 MeV. Right: Unphysical values for $m_\pi = 266$ MeV, $m_N = 1068$ MeV; for N^* the mass is chosen as 1670 MeV without changing the coupling strength. In both cases the lowest possible state is $N(0)\pi(0)$, which coincides with the threshold in the non-interacting case. For attractive interaction the level moves slightly below the threshold to negative values of q^2.

Considering the actual parameters of the simulations we may assume an elastic S-wave scattering and then derive the corresponding values of the phase shift.
The S-wave amplitude can be written as

$$T = \mathrm{e}^{\mathrm{i}\delta} \sin\delta = \frac{1}{\cot\delta - \mathrm{i}}, \tag{5.11}$$

and, using the effective range parametrization near threshold, we obtain

$$\sqrt{s}\,\rho_0(s) = \frac{1}{a_0} + \mathcal{O}(p^{*2}) \;, \tag{5.12}$$

where a_0 is the scattering length and we also define conveniently

$$\rho_0(s) = \frac{p^*}{\sqrt{s}} \cot\delta = \frac{2Z_{00}(1;q^2)}{L\sqrt{s\pi}} \;, \tag{5.13}$$

The $N(\frac{1}{2}^-)$ (s-wave) scattering amplitude is shown in the data analysis of [95] and has an intricate behavior, becoming quickly inelastic and hard to reliably parametrize.
One possibility to simplify the problem consists in taking into account only the first of the two resonances as a Breit Wigner resonance and focus on the energy region in its

vicinity. In this case ρ_0 can be approximated linearly,

$$\rho_0(s) = \frac{1}{\gamma}(s_R - s), \tag{5.14}$$

where s_R denotes the resonance position and γ is related to the width and to the coupling constant

$$\Gamma = \frac{p^*(s_R)}{s_R}\gamma, \qquad \gamma = g^2/6\pi. \tag{5.15}$$

Assuming a phase shift parameterization, one can numerically invert Eq. (5.10) and obtain the spectrum of the interacting system with the modified energy levels due to the avoided level crossing.
On the left hand side of Fig. 5.9 the distribution of the energy levels in the physical case can be observed: a resonance of mass $m_R = 1535$ MeV and $\Gamma = 150$ MeV has been used to model the phase shift and obtain the spectrum in finite volume. On the right hand side of Fig. 5.9 we present the analogous case with parameters that have been adjusted to coincide with our setup: the mass of the pion is set to $m_\pi = 266$ MeV (which is used as unit mass in the plot), the ground state nucleon has mass $m_N = 1068$ MeV (as earlier evaluated) and the resonance lies on $m_R = 1670$ MeV. The coupling strength γ at the resonance position is unchanged.
Let us now focus on $Lm_\pi = 2.7$ (the value corresponds to our lattice parameters) and compare the two pictures.
If physical masses are involved, different combinations of $N(\mathbf{p})\pi(-\mathbf{p})$ would be eligible for coupling with the resonance. However in the real case (RHS) only $N(\mathbf{0})\pi(\mathbf{0})$ lies below m_R. In the non-interacting case the $N\pi$ level coincides with the threshold, while for attractive interaction the level moves slightly below the threshold.

The two lowest energy levels can be related to ρ_0 and therefore to the scattering length. In Table 5.1 the values of ρ_0 from Eq. (5.13) can be found together with the resulting values of the phase shift, assuming elasticity. The second energy level lies close to the point where the phase shift crosses $\pi/2$ (this value is included within the errorbars). As discussed, the kinematic situation (pion mass and lattice size) allows the assumption to be in the elastic domain and thus one is tempted to assume validity of Eq. (5.14). The zero of the line connecting the values of ρ_0 at the two lowest energy levels gives the resonance position $a^2 s_R = 1.114(135)$ corresponding to a resonance mass $m_R = 1.678(99)$ GeV. This is ~ 140 MeV above the physical value, but not surprising due to the unphysical pion and nucleon masses, in fact, a similar shift as for the nucleon. Also note, that the $N\pi$ system in nature is already inelastic and the linearity assumption not justified in that case.

The third eigenstate has a phase shift of 47° ($\simeq 227^\circ$, since the $\arctan$ is defined modulo 180°), indicating a resonance lying closely above that energy value of 1.79 GeV – again under the unphysical assumption of elastic scattering.

Due to the closeness of the threshold to the resonance in our setting as compared to nature, we cannot expect physical values for scattering length or decay width. With Eq. (5.12) we can estimate the scattering length from the point close below threshold s_{thr}. We find a value $a_0 \simeq 5.3(\pm 1.4)$ GeV^{-1} roughly four times larger than, e.g., the leading order Chiral Perturbation Theory value $m_\pi/(4\pi F_\pi^2)$ [102, 103].

Choosing interpolators with non-zero total momentum allows in principle to obtain further energy levels and thus additional values of the phase shift. However, as seen in Chapter 3 and further explored in Chapter 5, when $\mathbf{P_{tot}} \neq 0$ new complications emerge and the mixing of different spin and momenta makes the high precision determination of the spectrum a computationally demanding task.

It might be also argued that the level $N(\mathbf{1})\pi(-\mathbf{1})$ is close enough to the second N^* resonance and should be included for a convincing analysis of the spectrum. However from the eigenvectors analysis of the combined 3 and 5 quark correlation matrix there is no hint that the third measured level might be trying to interpolate between two different states: the eigenvector composition results are stable in the fit range.

Note that Lüscher's relation holds in the elastic region. Most often inelasticity sets in early due to coupled channels. The presently pursued alternative is the inverse procedure, starting with a (unitarized) coupled channel parameterization of the scattering matrix in the continuum and then determining the expected discrete energy levels on finite volumes, see, e.g., [26–29]. The lattice results for the energy levels then can be interpreted along these lines.

5.7 Conclusions

In this chapter we presented the study of the $N\pi$ scattering in the negative parity, isospin $\frac{1}{2}$ sector in an ab initio lattice QCD calculation. We use both 3-quark and meson-baryon (5 quark) interpolators , highlighting the significant differences between the two different setups.

The overall behavior reminds to what has been found in other meson-meson studies, [20, 21]: when the two-particle interpolators are included in the variational analysis, the energy levels are rearranged in a way that better describes the experimental observations. This work represents a first step into that direction. More data (moving frames, different

volumes, further coupled channels) would fill the gap between elastic and inelastic threshold and allow the comparison with experiment and continuum models.

Chapter 6

$N\pi$ scattering in P-wave: the Roper sector

After the study of the $N\pi$ scattering in S-wave, we face the challenge of the P-wave in the same spin and isospin channel.
We will explain which are the main difficulties that have to be overcome, connected to the choice of a non-rest frame due to kinematic considerations.
As we have seen in Chapter 4, being in a rest frame allows to avoid problems related to the reduced symmetry group and the subsequent properties of the interpolators. However sometimes a $\mathbf{P_{tot}} = \mathbf{0}$ is not a possible choice.

6.1 P-wave kinematics

The task of the current study is to explore the positive parity sector of the nucleon spectrum including the $N\pi$ system in the analysis. This approach provides interesting information only if the pion-nucleon lower energy levels lie in the *interesting region* defined in Chapter 4.
Let us now explore the kinematics of different momenta combinations on our lattice and find an answer for the following questions:

- Which choice of the momenta is in agreement with our *interesting region constraint* combined with the necessity of a P-wave?
- Which are the properties of the symmetry groups in the selected moving frame?

- How do we write the $N\pi$ interpolator so that it transforms as the single particle operator?

From parity conservation considerations it is clear that the N^+ sector couples to the pion-nucleon system in P-wave:

$$P_{TOT} = P_1 \times P_2 \times (-1)^L \,, \tag{6.1}$$

with

$$P(N^+) = +1 \qquad P(\pi) = -1 \,, \tag{6.2}$$

which requires

$$L = 1 \longrightarrow P\text{-wave} \,. \tag{6.3}$$

Let us now have a look at the energy levels of the different P-waves that can be generated on our lattice.
The parameters of our lattice

$$m_N = 1080 \text{ MeV} \,, \qquad m_\pi = 266 \text{ MeV} \,, \qquad a = 0.1239 \qquad L = 16 \,,$$
$$p_{\text{Lab}} = |p| \frac{2\pi}{L} \frac{197}{0.1239} \,, \tag{6.4}$$

imply that the smallest momentum available is $p_{\text{Lab}} = 624$ MeV. It drastically restricts our possible choices.

$$E^i_{\text{Lab}} = \sqrt{m_i^2 + p_i^2} \,, \qquad E_{\text{CM}} = \sqrt{E^2_{\text{Lab}} - p^2_{\text{Lab}}} \,, \tag{6.5}$$

where E_{CM} is the energy of the non interacting system and $E_{\text{Lab}} = E_N + E_\pi$.

Here follows a list and a graphic representation of possible momenta combinations (see Fig. 6.1). Only those inside the energy region of our interest are actually listed. Note that the following results are only meant as a rough estimate of the energy region involved and are computed using naive kinematics formulas valid in the continuum.

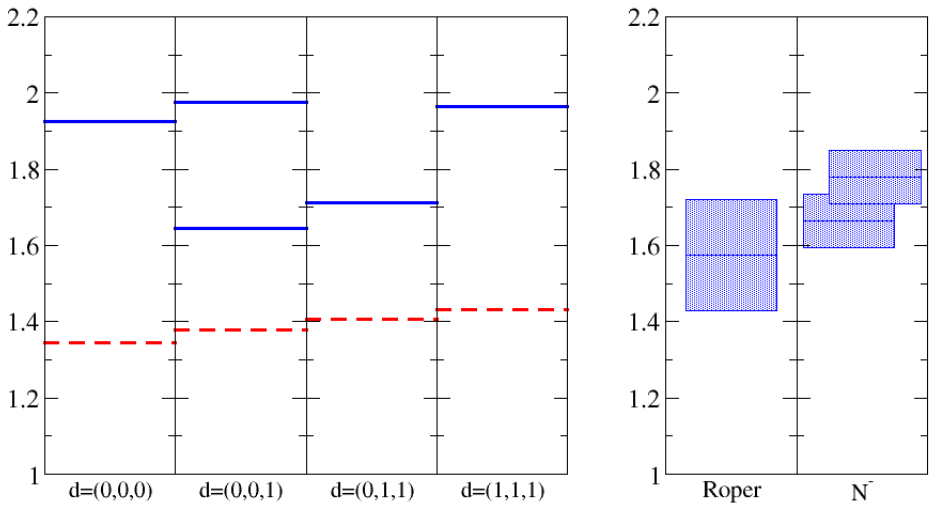

FIGURE 6.1: Pion-nucleon system energy levels in the CMF estimated on our lattice (left) compared with the expected nucleon spectrum (right). The dashed lines correspond to the levels with the pion at rest.

$\vec{d}$	$\vec{p}_N$	$\vec{p}_\pi$	E_{CM}
$(0,0,0)$	$(0,0,1)$	$(0,0,-1)$	1926 MeV
$(0,0,1)$	$(0,0,1)$	$(0,0,0)$	1379 MeV
$(0,0,1)$	$(0,0,0)$	$(0,0,1)$	1644 MeV
$(0,1,1)$	$(0,1,1)$	$(0,0,0)$	1407 MeV
$(0,1,1)$	$(0,0,1)$	$(0,1,0)$	1711 MeV
$(1,1,1)$	$(1,1,1)$	$(0,0,0)$	1431 MeV

Table: Pion-nucleon system energy levels in the CMF. $\vec{P}_{tot} = 2\pi/L\vec{d}$. The momenta of the pion and the nucleon are given in $2\pi/L$ units.

It is obvious that $\mathbf{P_{tot}} = (0,0,0)$ does not allow us to access the information we are interested in, therefore a non-rest frame has to be chosen.

The Roper resonance has mass $m = 1440$ MeV and width $\Gamma = 300$ MeV and its main decay channel is $N\pi$ in P-wave $(55-75\%)$.

Since we are working at unphysical pion mass and our nucleon has a mass that is roughly 130 MeV higher than the experimental one, we can naively expect that the same applies to the other particles (see also Chapter 5). We would therefore expect the Roper to have

a mass around 1570 MeV on our lattice.

This implies that the *interesting region* lies between 1420 MeV and 1720 MeV. Choosing any of the low lying setup should guarantee to observe one or more states in the right energy region.

6.2 Non-rest frames

In the case of $\vec{d} \neq (0,0,0)$, the symmetry O_h of the lattice is partially broken and we are left with a smaller symmetry group, the *Little group* (see Chapter 4).

Group	d	Little group
O_h	$(0,0,1)$	C_{4v}
	$(1,1,0)$	C_{2v}
	$(1,1,1)$	C_{3v}
${}^2O_h$	$(0,0,1)$	${}^2C_{4v}$
	$(1,1,0)$	${}^2C_{2v}$
	$(1,1,1)$	${}^2C_{3v}$

For different little groups, the mesh (our lattice grid, deformed due to non zero CM velocity) is invariant under a different subgroup of transformations and the interpolators have to be constructed so that they transform under irreducible representation of the new symmetry group [36].

6.2.1 $d = (0,0,1) \quad \rightarrow \quad {}^2C_{4v}$

The entries of M in Eq.(4.15) can be computed from the transformation properties of the interpolators. For each (J^P, I) combination we need to list the irreducible representations according to which the interpolators transform.

In the case of ${}^2C_{4v}$ for spin $\frac{1}{2}$ the representations $\Gamma^{(l)}$ available for the l-wave are

$$\begin{aligned} \Gamma^{(0)} &= G_1\,, \\ \Gamma^{(1)} &= G_1\,, \end{aligned} \tag{6.6}$$

while for spin $\frac{3}{2}$ we have

$$\begin{aligned} \Gamma^{(1)} &= G_1 \oplus G_2 \,, \\ \Gamma^{(2)} &= G_1 \oplus G_2 \,, \end{aligned} \tag{6.7}$$

Interpolators of particles with different spins transform according to the same irreducible representations (Irreps). To be more precise [36]

Γ	$dim\,\Gamma$	J	l
G_1	2	$\frac{1}{2}$	0
G_1	2	$\frac{1}{2}$	1
G_1	2	$\frac{3}{2}$	1
G_2	2	$\frac{3}{2}$	1
G_1	2	$\frac{3}{2}$	2
G_2	2	$\frac{3}{2}$	2

Therefore the two irreducible matrices M^{Γ} for a generic Irrep will have entries for spin $\frac{1}{2}$ and $\frac{3}{2}$, together with contributions from S- and P-waves, while D-waves ($l = 2$) will be from now on neglected due to the fact that we do not expect substantial contributions in the lower part of the spectrum.

This results in

$$M^{\Gamma}_{Jl,J'l'} = \begin{pmatrix} M_{\frac{1}{2}0,\frac{1}{2}0} & M_{\frac{1}{2}0,\frac{1}{2}1} & M_{\frac{1}{2}0,\frac{3}{2}1} \\ M_{\frac{1}{2}1,\frac{1}{2}0} & M_{\frac{1}{2}1,\frac{1}{2}1} & M_{\frac{1}{2}1,\frac{3}{2}1} \\ M_{\frac{3}{2}1,\frac{1}{2}0} & M_{\frac{3}{2}1,\frac{1}{2}1} & M_{\frac{3}{2}1,\frac{3}{2}1} \end{pmatrix}, \tag{6.8}$$

with

$$M^{G_1} = \begin{pmatrix} w_{00} & iw_{10} & i\sqrt{2}w_{10} \\ -iw_{10} & w_{00} & \sqrt{2}w_{20} \\ -i\sqrt{2}w_{10} & \sqrt{2}w_{20} & w_{00}+w_{20} \end{pmatrix}, \tag{6.9}$$

6.2.2 $d = (1,1,0) \quad \rightarrow \quad {}^2C_{2v}$

In this case there is a strong mixing between partial waves and different spin states, since all the half-integer spin operators transform under G_1.

Here follows a table that shows the correspondence between particles and Irreps (as already mentioned, the D-waves are not taken into account).

Γ	$dim\,\Gamma$	J	l
G_1	2	$\frac{1}{2}$	0
G_1	2	$\frac{1}{2}$	1
G_1	2	$\frac{3}{2}$	1
G_1	2	$\frac{3}{2}$	1

Given the irreducible representation D^l of the rotation group of total angular momentum l, the irreducible representation G_1 occurs twice in D^1 for $J = \frac{3}{2}$ (with two different couples of basis vector which are listed in [36]). This explains why G_1 is listed twice in the lower part of the Table.

The matrix M^{G_1} reads

$$M^{G_1}_{Jl[n],J'l'[n']} = \begin{pmatrix} M_{\frac{1}{2}0,\frac{1}{2}0} & M_{\frac{1}{2}0,\frac{1}{2}1} & M_{\frac{1}{2}0,\frac{3}{2}11} & M_{\frac{1}{2}0,\frac{3}{2}12} \\ M_{\frac{1}{2}1,\frac{1}{2}0} & M_{\frac{1}{2}1,\frac{1}{2}1} & M_{\frac{1}{2}1,\frac{3}{2}11} & M_{\frac{1}{2}1,\frac{3}{2}12} \\ M_{\frac{3}{2}11,\frac{1}{2}0} & M_{\frac{3}{2}11,\frac{1}{2}1} & M_{\frac{3}{2}11,\frac{3}{2}11} & M_{\frac{3}{2}11,\frac{3}{2}12} \\ M_{\frac{3}{2}12,\frac{1}{2}0} & M_{\frac{3}{2}12,\frac{3}{2}2} & M_{\frac{3}{2}12,\frac{3}{2}11} & M_{\frac{3}{2}12,\frac{3}{2}12} \end{pmatrix}, \tag{6.10}$$

where n, n' are running from 1 to 2 in the case of G_1 ($l = 1, J = 3/2$) for the reason explained before.

6.2.3 $d = (1,1,1) \quad \rightarrow \quad {}^2C_{3v}$

Here we present the correspondence between spin, partial waves and Irreps for ${}^2C_{3v}$.

Γ	$dim\,\Gamma$	J	l
G_1	2	$\frac{1}{2}$	0
G_1	2	$\frac{1}{2}$	1
G_1	2	$\frac{3}{2}$	1
K_1	1	$\frac{3}{2}$	1
K_2	1	$\frac{3}{2}$	1

In this case the matrix M^{Γ} has the following entries.

$$M^{\Gamma}_{Jl,J'l'} = \begin{pmatrix} M_{\frac{1}{2}0,\frac{1}{2}0} & M_{\frac{1}{2}0,\frac{1}{2}1} & M_{\frac{1}{2}0,\frac{3}{2}1} \\ M_{\frac{1}{2}1,\frac{1}{2}0} & M_{\frac{1}{2}1,\frac{1}{2}1} & M_{\frac{1}{2}1,\frac{3}{2}1} \\ M_{\frac{3}{2}1,\frac{1}{2}0} & M_{\frac{3}{2}1,\frac{1}{2}1} & M_{\frac{3}{2}1,\frac{3}{2}1} \end{pmatrix}, \tag{6.11}$$

with

$$M^{G_1} = \begin{pmatrix} w_{00} & \frac{\sqrt{6}}{2}(1-i)w_{10} & i\sqrt{6}w_{10} \\ \frac{\sqrt{6}}{2}(1+i)w_{10} & w_{00} & \sqrt{6}(1+i)w_{22} \\ -i\sqrt{6}w_{10} & \sqrt{6}(1-i)w_{22} & w_{00}-i\sqrt{6}w_{22} \end{pmatrix}. \tag{6.12}$$

6.3 $N\pi$: the favorable channels

The choice of the momenta setup has to be carefully made. Due to the large amount of CPU time that the simulations require, only few setups can be evaluated.

It has been seen in the previous section that the reduced symmetry affects the properties of the interpolators: it is not possible to construct a spin $1/2$ interpolator that disentangles spin and S/P-waves. As a consequence we expect that different sectors of the spectrum will appear in our measurements on the lattice, since some of the quantum numbers of the interpolator are not well defined.
A closer look to the experimental spectrum of the nucleon sector turns out to be helpful in understanding the problem.

It is clear from Fig.6.2 that the first $(J = 3/2, l = 1)$ state lies far above the energy region of our interest. Therefore it is reasonable to neglect its contribution and its influence on

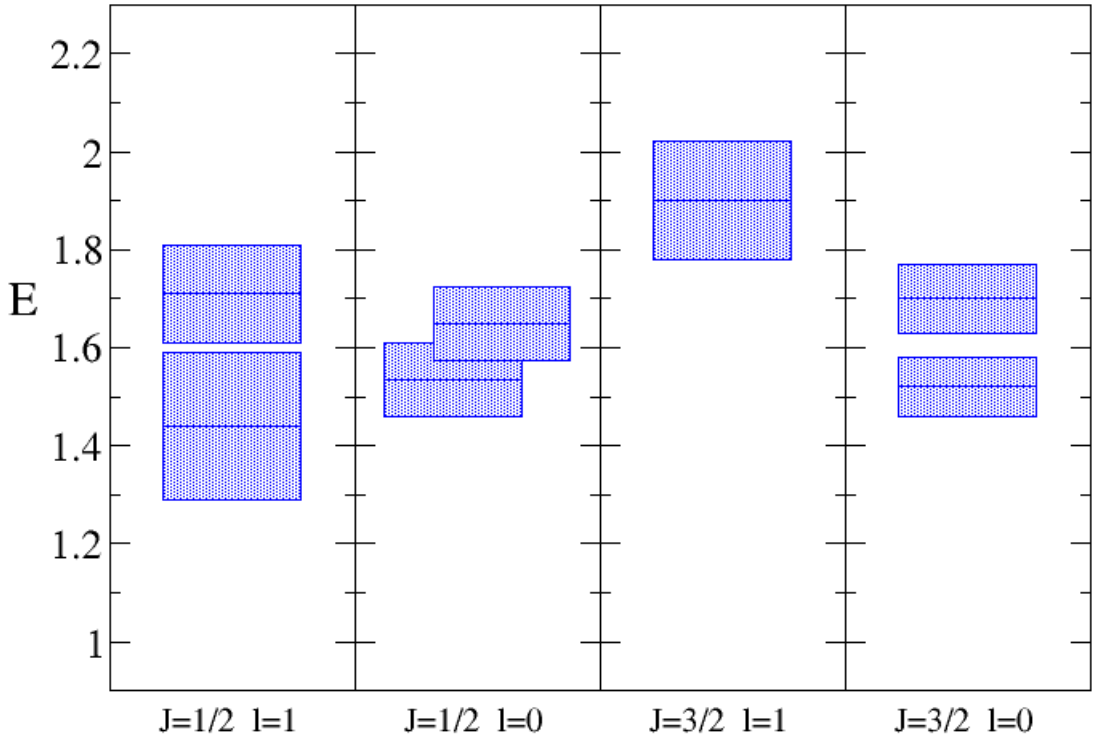

FIGURE 6.2: Nucleon states in different spin and parity sectors. The error bars represent the experimental widths.

the lower part of the spectrum [36]. On the other hand $(J = 3/2, l = 0)$ states do not mix with $(J = 1/2, l = 1)$ and do not represent a reason of concern.

As seen in the previous section, however, the two resonances $N(1440)$ and $N(1535)$, in P and S wave respectively, cannot be disentangled from each other neither from analytical considerations (every G_1 interpolator mixes the two waves) based on experimental evidences (the two resonances lie too close to each other to neglect the contribution of one of them).
In order to extract reliable information we need to compute the energy levels for both the S-wave and the P-wave of this channel.

Let us go through case by case and explicitly write the Lüscher's formula for the different momenta, keeping in mind that we neglect the $J = 3/2$ contribution:

$\mathbf{d} = (\mathbf{0}, \mathbf{0}, \mathbf{1})$

$$\det \begin{pmatrix} w_{00} - \cot \delta_{\frac{1}{2}0} & iw_{10} \\ -iw_{10} & w_{00} - \cot \delta_{\frac{1}{2}1} \end{pmatrix} = 0. \tag{6.13}$$

$\mathbf{d} = (\mathbf{1}, \mathbf{1}, \mathbf{0})$

$$\det \begin{pmatrix} w_{00} - \cot \delta_{\frac{1}{2}0} & \sqrt{2}(i-1)r_{11} \\ \sqrt{2}(i+1)r_{11} & w_{00} - \cot \delta_{\frac{1}{2}1} \end{pmatrix} = 0, \tag{6.14}$$

where $r_{11} = Re(w_{11})$.

$\mathbf{d} = (\mathbf{1}, \mathbf{1}, \mathbf{1})$

$$\det \begin{pmatrix} w_{00} - \cot \delta_{\frac{1}{2}0} & \frac{\sqrt{6}}{2}(1-i)w_{10} \\ \frac{\sqrt{6}}{2}(1+i)w_{10} & w_{00} - \cot \delta_{\frac{1}{2}1} \end{pmatrix} = 0. \tag{6.15}$$

Independently of the setup, we have to solve a similar equation which involves both $\delta_{\frac{1}{2}1}$ and $\delta_{\frac{1}{2}0}$. Computing high quality data on both of the phase shifts in order to perform the Lüscher analysis seems nowadays beyond our possibility (see the attempt made for the S-wave), therefore we will focus on a qualitative study of the energy levels, keeping in mind that the numerical values might be shifted due to the level crossing and this shift cannot be now estimated.

6.4 $N\pi$ interpolators

We chose to use $\vec{d} \neq \vec{0}$ and we need to write an interpolator which describes the two particle states and transforms according to the same Irrep of the single particle interpolator O_N.

We will explicitly study the case $\vec{d} = (0,0,1), \vec{p_N} = (0,0,1), \vec{p_\pi} = (0,0,0)$.

For $d = (0,0,1)$ the little group is C_{4v} for integer spin and its double cover ${}^2C_{4v}$ for half-integer spin. O_N transforms like G_1 and we will construct a $N\pi$ operator with the same properties under group transformations.

Let us call $\hat{R}$ a transformation belonging to the little group and Ω a transformation in its double cover. The behavior of the interpolators under these transformation will tell us about the irreducible representation they belong to.

The pion interpolator transforms according to A_1:

$$\pi(\mathbf{x}, t) = \bar{\psi}(\mathbf{x}, t)\gamma_5\psi(\mathbf{x}, t), \tag{6.16}$$

$$\pi(\mathbf{p},t) = \sum_{\mathbf{x}} e^{-i\mathbf{p}\mathbf{x}}\pi(\mathbf{x},t), \tag{6.17}$$

$$\pi(\mathbf{p},t) \longrightarrow \ \pi(\hat{R}\,\mathbf{p},t). \tag{6.18}$$

The Nucleon interpolator transforms under G_1:

$$N_\alpha(\mathbf{x},t) = \Gamma_{\alpha\beta}(\psi(\mathbf{x},t)\psi(\mathbf{x},t)\Gamma\psi(\mathbf{x},t))_\beta, \tag{6.19}$$

$$N_\alpha(\mathbf{p},t) = \sum_{\mathbf{x}} e^{-i\mathbf{p}\mathbf{x}}N_\alpha(\mathbf{x},t), \tag{6.20}$$

$$N_\alpha(\mathbf{p},t) \longrightarrow \Omega_{\alpha\beta}\ N_\beta(\hat{R}\,\mathbf{p},t). \tag{6.21}$$

The pion-nucleon interpolator is

$$O_\alpha(\mathbf{p_{tot}},\mathbf{p},t) = N_\alpha(\mathbf{p},t)\pi(\mathbf{p_{tot}}-\mathbf{p},t) = \sum_{\mathbf{x},\mathbf{y}} e^{-i(\mathbf{p_{tot}}-\mathbf{p})\mathbf{x}-i\mathbf{p}\mathbf{y}}\pi(\mathbf{x},t)N(\mathbf{y},t). \tag{6.22}$$

It transforms as

$$O_\alpha(\mathbf{p_{tot}},\mathbf{p},t) \longrightarrow \Omega_{\alpha\beta}\ O_\beta(\hat{R}\,\mathbf{p_{tot}},\hat{R}\,\mathbf{p},t) \tag{6.23}$$

and from the definition of $O = N\pi$

$$RO_\alpha(\mathbf{p_{tot}},\mathbf{p},t)R^{-1} = R\,N_\beta(\hat{R}\,\mathbf{p},t)R^{-1}\ R\,\pi(\hat{R}\,(\mathbf{p_{tot}}-\mathbf{p}),t)R^{-1}. \tag{6.24}$$

The correct transformation properties of the interpolators can be easily shown if the momenta of the two particles are written as a sum of a vector parallel to the unitary boost vector $\mathbf{d}$ and one perpendicular $\mathbf{u} \perp \mathbf{d}$.

In general we would have

$$\mathbf{p_{tot}} = \mathbf{d}, \qquad \mathbf{p_N} = \mathbf{d}+\mathbf{u}, \qquad \mathbf{p}_\pi = -\mathbf{u}. \tag{6.25}$$

then

$$O(\mathbf{p_{tot}}) = N(\mathbf{d}+\mathbf{u})\pi(-\mathbf{u}) \tag{6.26}$$

In the CM frame

$$p^* = \gamma^{-1}(\mathbf{p_N} - \frac{1}{2}A(\mathbf{p_N}+\mathbf{p}_\pi)) = \gamma^{-1}(\mathbf{d}+\mathbf{u}-\frac{1}{2}A\mathbf{d}) = \gamma^{-1}(\Lambda\mathbf{d}+\mathbf{u}) = \alpha\mathbf{d}+\beta\mathbf{u}, \tag{6.27}$$

where $A, \Lambda, \alpha, \beta$ are coefficients which depend on the masses of the two particles and the momentum.

The $N\pi$ interpolator in the CMF

$$O_{CM} = N(\alpha\mathbf{d} + \beta\mathbf{u})\pi(-(\alpha\mathbf{d} + \beta\mathbf{u})) \tag{6.28}$$

and we want to understand how it transforms under the transformations of ${}^2C_{4v}$:

$$\rightarrow R\,O(\hat{R}\mathbf{d}, \hat{R}\mathbf{u})\,R^{-1}. \tag{6.29}$$

Our case is trivial:

$$\mathbf{p_{tot}} \propto \mathbf{d} = (0,0,1), \qquad \mathbf{p_N} \propto \mathbf{d}, \qquad \mathbf{p}_\pi = \mathbf{0}, \tag{6.30}$$

then

$$O(\mathbf{p_{tot}}, \mathbf{p}) = N(\mathbf{d})\pi(\mathbf{0})), \tag{6.31}$$

but, since in this case $\mathbf{u} = \mathbf{0}$, then

$$\mathbf{p}^* = \alpha\mathbf{d} \tag{6.32}$$

and

$$O_{CM} = N(\alpha\mathbf{d})\pi(-\alpha\mathbf{d})). \tag{6.33}$$

Since $\mathbf{d}$ is invariant under $\hat{R}$ and so is $\pi(\mathbf{p})$ (which transforms as A_1), then

$$\hat{R}O(\mathbf{d},\mathbf{u})\hat{R}^{-1} = \hat{R}N(\mathbf{d})\pi(-\mathbf{d})\hat{R}^{-1} = \hat{R}N(\mathbf{d})\hat{R}^{-}1\hat{R}\pi(-\mathbf{d})\hat{R}^{-1} = \hat{R}N(\mathbf{d})\hat{R}^{-1}\pi(-\mathbf{d}), \tag{6.34}$$

from which it is clear that $O(\mathbf{d},\mathbf{u})$ transform exactly like $N(\mathbf{d})$, which is in G_1. In other words, with a pion at rest we can only build operators transforming according to $G_1 \otimes A_1 = G_1$.

To summarize: for $\mathbf{d} = (0,0,1)$, given that the pion is at rest, any interpolator

$$O_{N\pi}(\mathbf{p},t) = N(\mathbf{p},t)\pi(\mathbf{0},t) \tag{6.35}$$

will always transform under G_1. The same result would have been obtained if the pion had non zero momentum, but still parallel to $\mathbf{d}$.

An analogous result is obtained for interpolators transforming under G_1 in ${}^2C_{2v}$ or ${}^2C_{3v}$.

6.5 Effective masses

We have studied the spectrum of the nucleon for one-particle and two-particle systems in moving frames, namely $\mathbf{P_{tot}} = (0,0,1)$ and $\mathbf{P_{tot}} = (1,1,1)$ (with suitable symmetrization in the spatial directions).
As mentioned in the previous sections, a definite parity projection of the interpolators is not possible (see Appendix B, therefore we compute the spectrum using unprojected operators and taking into account that a superposition of the N_+ and N_- spectrum has to be expected.

For the analysis we use a set of 6 interpolators:

$$\begin{aligned} &\mathcal{O}_1,\, \mathcal{O}_2 = N^{(1)},\, N^{(2)} && \text{with } N_v = 32, \\ &\mathcal{O}_4,\, \mathcal{O}_5 = N^{(1)},\, N^{(2)} && \text{with } N_v = 64, \\ &\mathcal{O}_7,\, \mathcal{O}_8 = O_{\pi N^{(1)}},\, O_{\pi N^{(2)}} && \text{with } N_v = 32, \end{aligned} \tag{6.36}$$

with 3 and (4+1) quarks. Interpolators of type $N^{(3)}$ or $\pi N^{(3)}$ have been discarded since they did not bring any improvement in the diagonalization of the correlation matrix.

6.5.1 Single particle spectrum for $\mathbf{P_{tot}} = (0,0,1)$

In Fig. 6.3 (on the left hand side) we present the results due to the diagonalization of a (4×4) correlation matrix, where only 3-quark interpolators have been used. We observe three states: two of them are relatively stable, while the third signal is quickly decaying and it will not be considered in the further analysis, but it will serve as reference point for the comparison with the two-particle system.

The lowest state is without doubts the ground state nucleon. It mainly couples to interpolators of type $N^{(1)}$ (see Fig. 6.4 LHS) and its mass in the CMF in physical units corresponds to $1040(6)$ MeV, very close to the evaluation made for $\vec{P}_{tot} = (0,0,0)$ (see Chapter 5).
The second state corresponds to $1538(42)$ MeV in the CMF and could be either a positive or a negative nucleon excitation. Having a closer look at the results of the previous chapter helps us in identifying this state. In Fig. 5.3 we present the 3-quark interpolators spectrum for N^+ and $\vec{P}_{\text{tot}} = (0,0,0)$. We observe a ground state nucleon followed by a state which is far above the energy region that we are now inspecting. The only difference between those results and the ones presented now in Fig. 6.3 consists in a different total momentum and we do not expect that this could be responsible for a complete revolution in the spectrum. Therefore we assume that this state is not a 3-quark N^+ state.

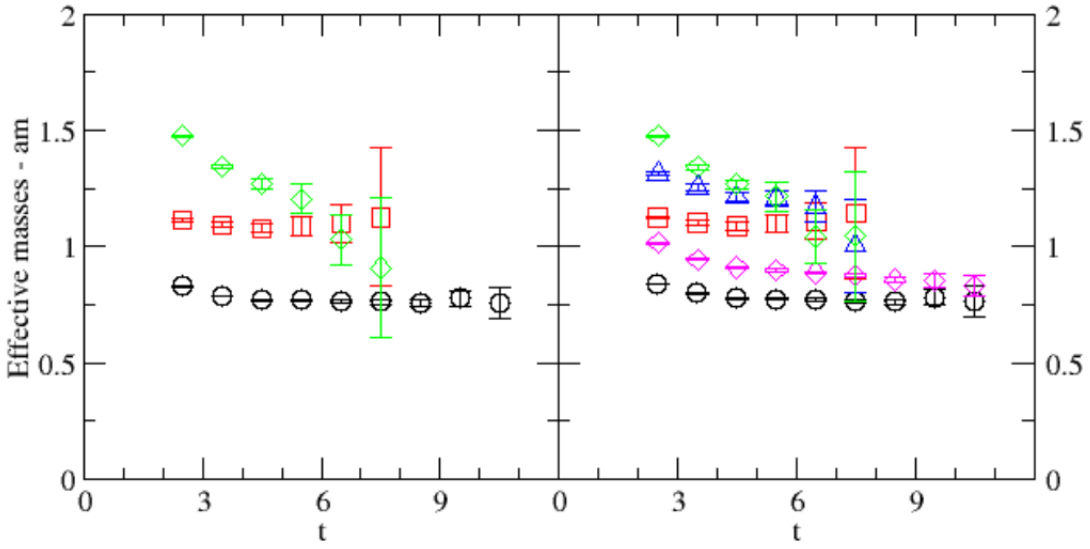

FIGURE 6.3: Comparison between the effective masses evaluated in the 3-quark setup and the result of the 5-quark system setup for $\vec{P}_{tot} = (0, 0, 1)$. All the masses are given in lattice units. Note that when the $(4 + 1)$ quark interpolators are included in the analysis two more states appear: the magenta and the blue state.

Let us now have a look at the first N^- state measured in the 3-quark sector (see Fig. 5.5): similarly to the state that we are now analyzing, that state has an energy that lies below the $N(1535)$ and it mainly couples to $N^{(2)}$ type interpolators. Another common feature is the instability of the eigenvectors composition observed in both Fig. 5.5 (RHS) and Fig. 6.4 if compared with the results obtained in the 5-quark case. Therefore we identify this state (the red one in Fig. 6.3 LHS) as a N^- state.

6.5.2 Two-particle spectrum

When two-particle interpolators are included in the analysis, some unexpected modifications to the spectrum are observed (see Fig. 6.3 RHS): not only one, but two new levels appear. The analysis of the eigenvectors composition is crucial for the interpretation of the energy levels.

1st state

The first lower state can be clearly interpreted as the ground state nucleon: it mainly couples to $N^{(1)}$ type interpolators and its mass in the CMF is compatible with the corresponding level computed in the previous chapter for $\vec{P}_{tot} = \vec{0}$.

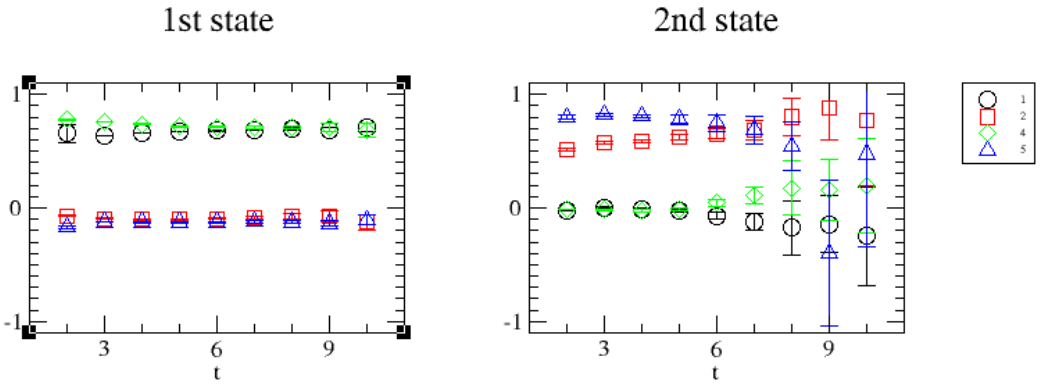

FIGURE 6.4: Eigenvectors of the first and second state of the spectrum evaluated from a 3quark interpolators and $\vec{P}_{tot} = (0, 0, 1)$. Remember that no parity projection is performed and the evaluated states can be either positive or negative parity. Interpolators $\{1, 7\}$ are of type $N^{(1)}$, while interpolators $\{2, 8\}$ are of type $N^{(2)}$.

2nd state

The second state has a very stable signal and its energy can be evaluated with high precision (see Fig. 6.6). Its eigenvector composition leaves no doubts about its nature: this state is clearly a pion-nucleon state: it is dominated by $\pi N^{(1)}$ type interpolators, with an additional small coupling with $N^{(1)}$. This behavior has already been observed in the S-wave analysis. From Fig. 6.6 we see that in the CMF this state lies below the $N\pi$ threshold, however it is not surprising for a two particle system with attractive interaction (the same happens for S-wave).

3rd state

This state seem to correspond to the first N^- state. The main contribution to this level are from $N^{(2)}$ interpolators, with a minor contribution from $\pi N^{(2)}$. This is exactly the same signature of the state measured in the previous chapter (see Fig. 5.6 RHS 2nd state and Fig. 5.8). The eigenvector composition of this level shows good stability as compared with the 3-quark case and the same pattern can be recognized in the previous chapter. It has to be kept in mind that, due to the reduced choice in irreducible representations for the interpolators and the absence of a coherent parity projection, a mix of S and P wave in this channel is expected, therefore it is not surprising that also the N^- sector is affected by the coupling with the pion-nucleon system.

4th state

The most interesting state in our study is the fourth state measured in this (J, I) sector. This state appears when pion-nucleon interpolators are included and it was absent in the

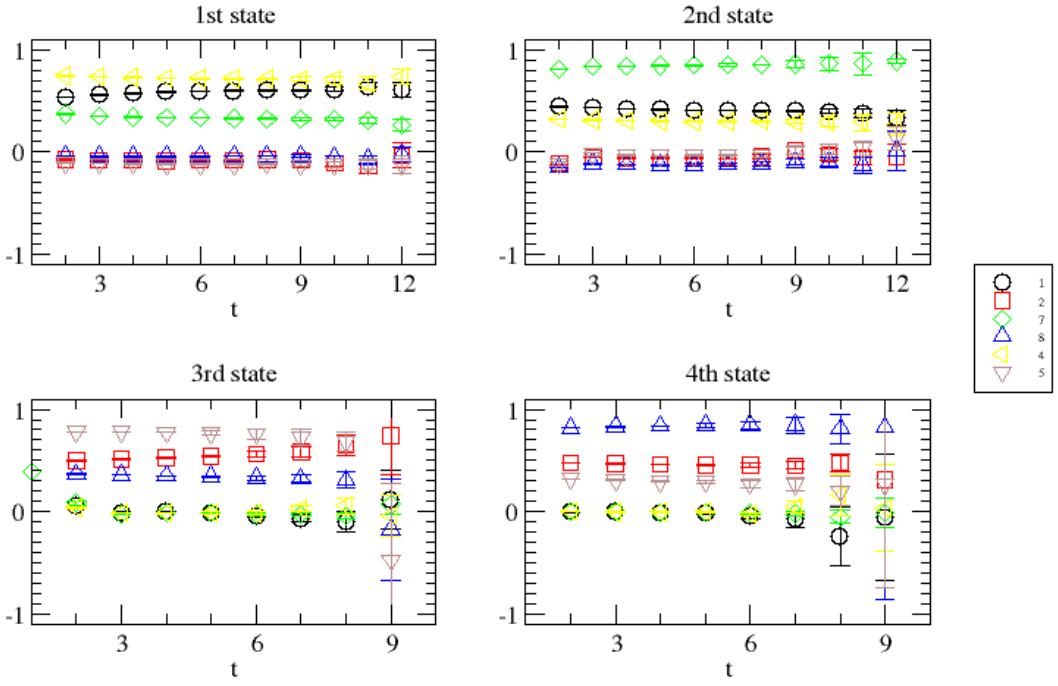

FIGURE 6.5: Eigenvectors of the four lowest states of the spectrum of the coupled $\{N, N\pi\}$ system with $\mathbf{P_{tot}} = (0,0,1)$. Interpolators $\{1,4\}$ are of type $N^{(1)}$, interpolators $\{2,5\}$ are of type $N^{(2)}$ and interpolators $\{7,8\}$ are of type $(N^{(1)}\pi)$ and $(N^{(2)}\pi)$ respectively.

one-particle study of the same problem. From Fig. 6.5 we see that it mainly couples to $(4+1)$ interpolators of type $\pi N^{(2)}$, plus additional contributions from $N^{(2)}$ interpolators. In order to interpret this state we will go through different hypothesis and the already known information that are available on the nucleon spectrum thanks to our previous study.

The possibility of this state to correspond to $N^{-}(1650)$ has to be excluded: in Chapter 5 we have seen that this state couples to $N^{(1)}$ and mildly with $\pi N^{(1)}$. Obviously some fluctuations in the eigenvectors composition could be admitted as possible, however a coupling with completely different interpolators is not an option when the only difference in the setup is the total momentum.

Another possibility for this state, due to the fact that it couples to two particle interpolators, is to be a pion-nucleon state with different momenta than those assigned by hand in our simulations. In Fig. 6.6 LHS we see that the state $N(0)\pi(0,0,1)$ lies in the same energy region (middle green dashed line in Fig. 6.6 leftmost column). This state is a combination of a pion with a ground state nucleon and the ground state nucleon is

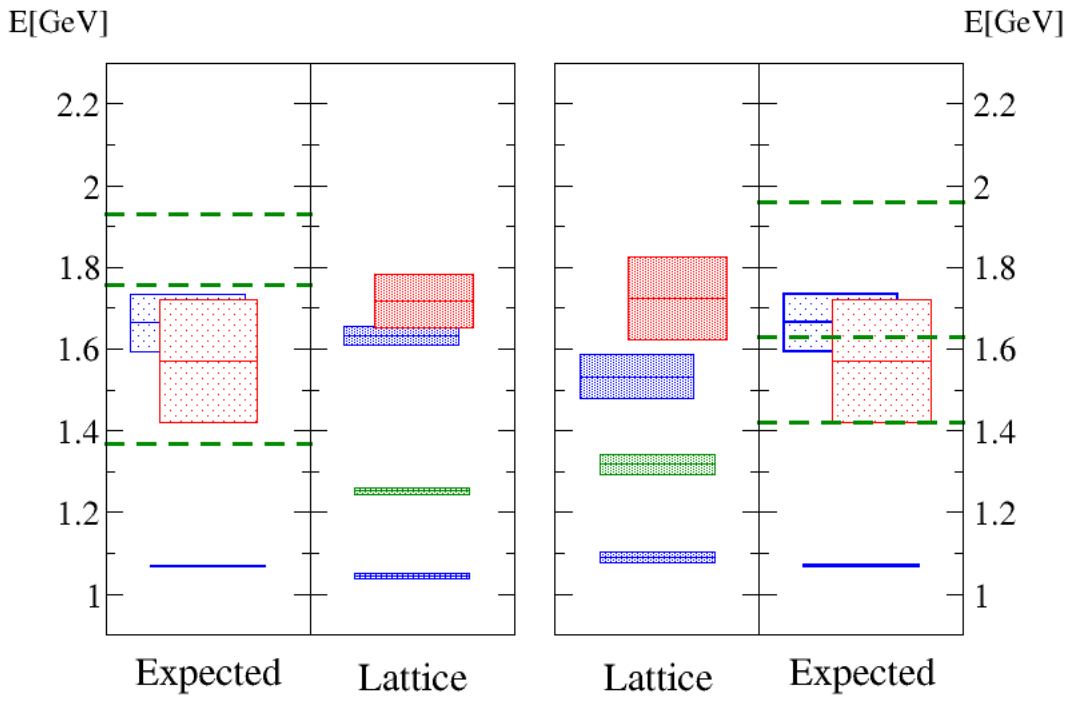

FIGURE 6.6: Results obtained in the CMF on our lattice compared with the expected values (i.e. the physical values of the masses are shifted up of $\Delta E \sim 130$ MeV and the error bars correspond to the experimental width [2]). The green dashed lines correspond to the expected energy values of the non-interacting $N\pi$ system on our lattice: from lower to higher values of the energy we find $\{N(0,0,1)\pi(0),\ N(0)\pi(0,0,1),\ N^*(0,0,1)\pi(0)\}$ for $\vec{P}_{tot} = (0,0,1)$ (left) and $\{N(1,1,1)\pi(0),\ N(1,1,0)\pi(0,0,1),\ N^*(1,1,1)\pi(0)\}$ for $\vec{P}_{tot} = (1,1,1)$ (right). Note that in the *expected values* column $N^*(1650)$ has not been plotted since our interest is focused in the lower part of the spectrum and from the analysis of the eigenvectors it is clear that none of the energy levels plotted the the *Lattice* column can be associate to the resonance.

not affected at all by $N^{(2)}$ interpolators, therefore $N(0)\pi(0,0,1)$ would couple to $\pi N^{(1)}$ interpolators, which is not the case for the state we observe.
Due to the eigenvector signature of the observed level, it might be argued that this state could be a $\pi N(1535)$ state, the energy value of which is plotted in Fig. 6.6 (highest green dashed line in the leftmost column). Due to the fact that it is considerably high with respect to our 4th state, we consider it safe to exclude this option.

A possible interpretation for this state is its identification with the Roper resonance. The nature of this state has been discussed in many different contexts [45–48] [49–51] and one of the hypothesis suggests a pentaquark nature for this resonance. This picture is supported by the fact that the contribution of the $(4+1)$quark interpolator to this state is considerably higher than the other single particle states and we excluded the possibility

for it to be a $N\pi$ state. In addition this would explain the fact that the N^+ spectrum measured using 3-quark interpolators does not provide any candidate for this resonance. It has to be noticed that the interpolators have no absolute normalization, therefore a statement concerning the dominance of one compared to two particle interpolators cannot be done. Nevertheless a comparison with the other states of the observed spectrum is allowed.

This study has also been performed for a different total momentum: $\vec{P}_{tot} = (1,1,1)$ and the results are plotted in the right hand side of Fig. 6.6. Due to the instability of the signal, obtaining a high precision estimation for the different energy levels is beyond the possibility of this study, however it is clear that the emerging picture is completely compatible with the $\vec{P}_{tot} = (0,0,1)$ study. The states appear with the same ordering and the same eigenvector composition, therefore all the considerations just made for the other momentum setup hold also in this case.

The evaluation of the spectrum for two different total momenta is important to exclude mistakes in the interpretation of the states. The fact that the states appear with the same order and the same eigenvector signature supports our conclusions.

6.6 Conclusions

We have computed the pion-nucleon spectrum using nucleon interpolators and pion-nucleon in non zero total momentum. With this choice S and P waves (and therefore positive and negative parity) are mixed and the interpretation of the evaluated energy levels has to be done with special care.
We observe, as expected, that including the two-particle interpolators determines the presence of a πN state with a clear and stable signal. However also the rest of the spectrum is subject to a major modification: a new state appears. This state strongly couples to the (4+1)quark interpolators, but it seems not to be compatible with any 2-particle state. A possible interpretation consists in connecting this state to the Roper resonance. The state, however, still appears above the state identified as the $N(1535)$. It is possible that an extrapolation to physical masses leads to the inversion of the mass ordering, however this cannot be done in the context of the current study.

Chapter 7

$\Delta - N\pi$ coupled system

Following the pattern already explained in the previous chapters, we now study the delta baryon $\Delta(1232)$ treating the particle as a resonance, therefore including the pion-nucleon system in the analysis.
The delta couples to an $N\pi$ system in P-wave and a non-vanishing total momentum is required for kinematic reasons. All the tools developed in Chapter 6 concerning the study of resonances in a finite box for non-rest frame will be applied to this case.

7.1 Kinematics and favorable channels

The delta $\Delta(1232)$ is a resonance and it decays almost exclusively into a pion-nucleon P-wave. It has a very narrow width of $\Gamma \sim 120$ MeV and a very characteristic phase shift (see Fig. (7.1)), therefore we expect its features to be detectable with a phase shift analysis of the coupled $\Delta - N\pi$ system.
First of all an analysis of the kinematics of the system on our lattice is necessary: we need to detect the energy region that is interested by the presence of the resonance and therefore useful for the extraction of the resonance parameters.

Due to the unphysical pion mass we expect an overall shift up of the hadron spectrum that we measure on our lattice. We fix this shift to $\Delta E = 130$ MeV in order to compute a rough estimate of the expected energy levels.
Assuming that the delta will manifest itself at roughly 1232 MeV $+ \Delta E = 1362$ MeV, we compute the possible momenta combinations for the pion-nucleon system in order to hit the *interesting energy region* which we define as

$$m_\Delta \pm \Gamma \sim [1300 - 1420] \text{ MeV}. \tag{7.1}$$

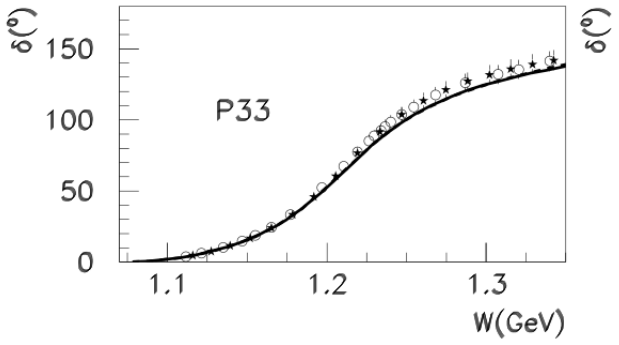

FIGURE 7.1: Phase shift of the P_{33} wave of the pion-nucleon system from [1].

The pion-nucleon systems that have compatible energies are

Little group	$\vec{d}$	$\vec{p}_N$	$\vec{p}_\pi$	E_{CM}
${}^2C_{4v}$	$(0,0,1)$	$(0,0,1)$	$(0,0,0)$	1379 MeV
${}^2C_{2v}$	$(0,1,1)$	$(0,1,1)$	$(0,0,0)$	1407 MeV
${}^2C_{3v}$	$(1,1,1)$	$(1,1,1)$	$(0,0,0)$	1431 MeV

Tab. A: Pion-nucleon system energy levels in the CMF. $\vec{P}_{tot} = 2\pi/L\vec{d}$. The momenta of the pion and the nucleon are given in units of $2\pi/L$.

All the combinations that involve a pion with non-zero momentum are far above the energy region of interest.

We now analyze the consequences of the broken symmetries in non-rest frames in order to find the most favorable channels for our calculation. This information is essential in the construction of the interpolators.

Little group	Irreps compatible with Δ : (J,l)
${}^2C_{4v}$	$G_1 : (1/2,0), (1/2,1), (3/2,2)...$, $G_2 : (3/2,1), (3/2,2)$
${}^2C_{2v}$	$G_1 : (1/2,0), (1/2,1), (3/2,2)...$
${}^2C_{3v}$	$K_1 : (3/2,1), (3/2,2)...$, $K_2 : (3/2,1), (3/2,2)...$, $G_1 : (1/2,0), (1/2,1), (3/2,2)...$

Tab. B: This table is extrapolated from the information found in [36].

In all the three little groups the $(\frac{3}{2}^+)$ sector is involved in mixing of spins or partial waves. Some of the irreducible representations (see Tab. B) do not mix states with different spin.

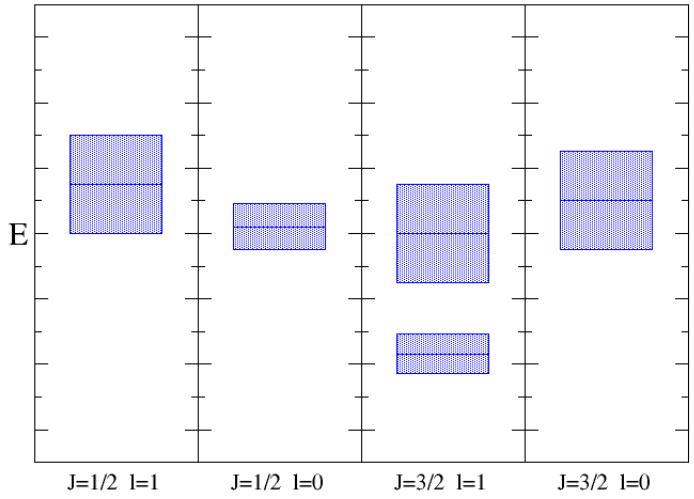

FIGURE 7.2: Experimental energies of the Δ spectrum. The error bars represent the experimental width. Note that the $J = 3/2\, l = 0$ states shown in the last column never happen anyway to mix with the other states in the formulas for the evaluation of the phase shift.

Unfortunately it is not possible to construct an interpolator which transforms according to any of these Irreps: their properties under symmetry transformations would require interpolators with a pion not at rest, which is not an available choice. The coarseness of our lattice is such that the $N\pi$ energy levels would lie too far above the resonance to be of any interest. The only suitable possibility is G_1.

The irreducible representation G_1 implies, in all the little groups, a mixing among all the channels. As a consequence solving the phase shift equation

$$\det(\cot\delta - M) = 0 \tag{7.2}$$

results to be a hard challenge: the presence of several unknown variables (the different δ_{lm}) would prevent from achieving a numerically reliable result. Eq.(7.2) can be nevertheless simplified by looking at the experimental spectrum of the delta baryon.

In Fig. (7.2) we present the energy levels of the delta in various channels. The ground state delta $\Delta(1232)$ lies far below all the other resonances and, considering its very narrow width it is unlikely that any of the other states can have any influence on the phase shift of the low lying delta. (The same argument is used in [36] for the Roper resonance).
If we assume that in the region of interest the phase shift of the pion-nucleon P_{33} wave is only determined by the presence of the $\Delta(1232)$, the terms in the Lüscher's formula

which depend on the other resonances can be dropped. A setup like $\mathbf{d} = (0, 0, 1)$ which seemed unfavorable from a merely analytic point of view, reveals itself to be a good choice for the study of this resonance.

7.2 Phase shift

Here follows a summary of the simplified phase shift formulas. They are obtained by taking into account the isolation of the $\Delta(1232)$ in its energy region. The contributions from the rest of the spectrum are neglected and the only term that survives in the phase shift formula is the $(J = 3/2, l = 1)$ one.

- $d = (0, 0, 1)$
  The phase shift equation reduces to

$$w_{00} + w_{20} - \cot \delta_{\frac{3}{2}1} = 0. \tag{7.3}$$

- $d = (1, 1, 0)$
  Due to the double occurrence of G_1, the matrix M cannot be reduced completely and it therefore represents a non-favorable channel.

- $d = (1, 1, 1)$
  In this sector, once we project the Δ interpolator on the representation G_1 we are left with

$$w_{00} - i\sqrt{6}w_{22} - \cot \delta_{\frac{3}{2}1} = 0, \tag{7.4}$$

  which is another favorable option.

7.3 G_1 Interpolators

Due to the forced choice of having a pion at rest, we are restricted to pion-nucleon interpolators in G_1 (see Chapter 6 for further discussion on the topic and an explicit derivation of the $O_{N\pi}$ properties under discrete transformations). We need to construct a two-particle interpolator and a single particle interpolator with the same quantum numbers in order to guarantee compatibility and a non-zero correlation function.

7.3.1 $N\pi$

In Chapter 6 we have shown that any interpolator of the type

$$O_{N\pi}(\mathbf{p}, t) = N(\mathbf{p}, t)\pi(\mathbf{0}, t) \tag{7.5}$$

transforms according to G_1 in all the three *Little Groups* of interest: ${}^2C_{4v}$,${}^2C_{2v}$,${}^2C_{3v}$.
As mentioned in Chapter 6 and explained in Appendix B, the parity of an operator in a moving frame is not a well defined property, therefore we do not introduce any parity projection in the construction of our interpolators.
The isospin projection is also trivial in this case: we chose $(I = 3/2, I_3 = 3/2)$ so that

$$O_{N\pi} = p\pi^+ , \tag{7.6}$$

where p is the positive charged nucleon (with quark content (uud)). In the two-particle sector we use in total three pion-nucleon interpolators:

$$\mathcal{O}_3,\, \mathcal{O}_4,\, \mathcal{O}_5 = O_{\pi N^{(1)}},\, O_{\pi N^{(2)}},\, O_{\pi N^{(3)}} , \qquad \text{with } N_v = 32. \tag{7.7}$$

7.3.2 Δ

The delta interpolator is usually defined as

$$\Delta^i_\alpha = \epsilon_{abc} P^{\pm}_{\alpha\beta} \psi^a_\beta \; \psi^b_\gamma (C\gamma^i)_{\gamma\delta} \, \psi^c_\delta . \tag{7.8}$$

Due to its $3/2$ spin, a Rarita-Schwinger projection is needed. The interpolator $\Delta^{(i)}$ is multiplied by the projector

$$P^{3/2}_{\mu\nu}(p) = \delta_{\mu\nu} - \frac{1}{3}\gamma_m u\gamma_\nu - \frac{1}{3p^2}\left(\gamma \cdot p\gamma_\mu p_\nu + p_\mu \gamma_n u\gamma \cdot p\right) , \tag{7.9}$$

where p is the four-momentum of the particle. The projector reduces to a trivial combination of gamma matrices for a particle at rest $(\mathbf{p} = 0)$ since the explicit momenta in the third term of Eq.(7.9) cancels out.
When the three-momentum is different from zero, however, the p^2 term does not cancel and it determines the impossibility of a well defined projection.

Not performing a Rarita-Schwinger projection implies that the mixing between spin $1/2$ and spin $3/2$ states cannot be avoided. However, as discussed in Section 7.1, the ground state delta $\Delta(1232)$ lies far below all the other $(I = 3/2)$ states in the different channels and an interpolator which mixes the sectors is not supposed to affect the extraction of the low lying energy value.

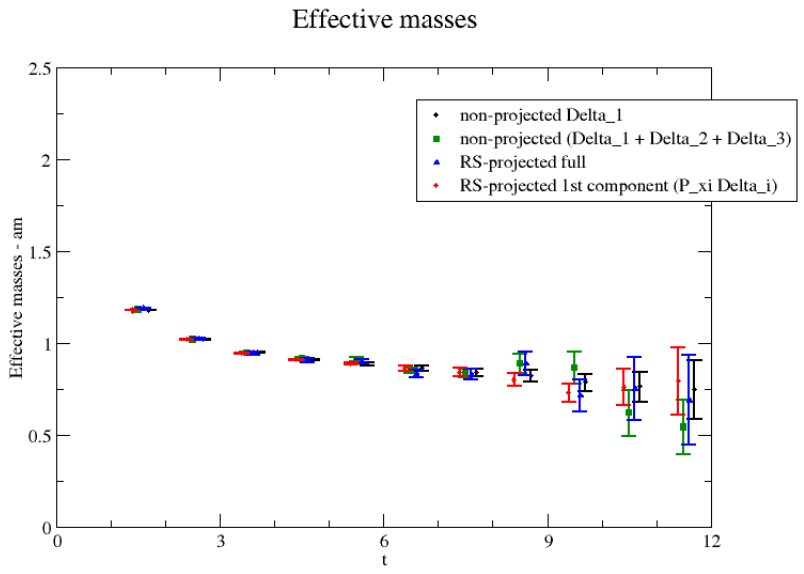

FIGURE 7.3: Comparison of the signal of the ground state obtained with different delta interpolators. No difference is manifest.

In order to support this assumption we have performed the calculation of a simple diagonal correlator relative to a single particle interpolator for the Δ with and without Rarita projection in total zero momentum. The results can be seen in Fig. (7.3): there is no sensible difference between the state extracted from the interpolator which has been projected to spin $3/2$ and the results relative to the operator defined in Eq.(7.8) with spin mixing. No significant difference arises from the comparison. Another interesting fact is that the $\left(\sum_{i=1}^{3} \Delta^{(i)}\right)$ signal is compared with $\Delta^{(1)}$ and again no evident difference is manifest. All the differences (if any) are washed away by the statistical error, giving high quality and compatible results for the fit of all the four signals.

Considering what we have just observed in the rest frame, we have no reason to assume that the situation in a non-rest frame would be different, therefore we use as single particle interpolator

$$\mathcal{O}_1, \mathcal{O}_2 = \Delta^{(z)} \quad \text{with} \quad N_v = 32, 64, \tag{7.10}$$

where $\Delta^{(z)}$ is the third component of Eq.(7.8) without parity projection and it corresponds to the third component of the delta interpolator projected onto G_1 (see [36] for details).

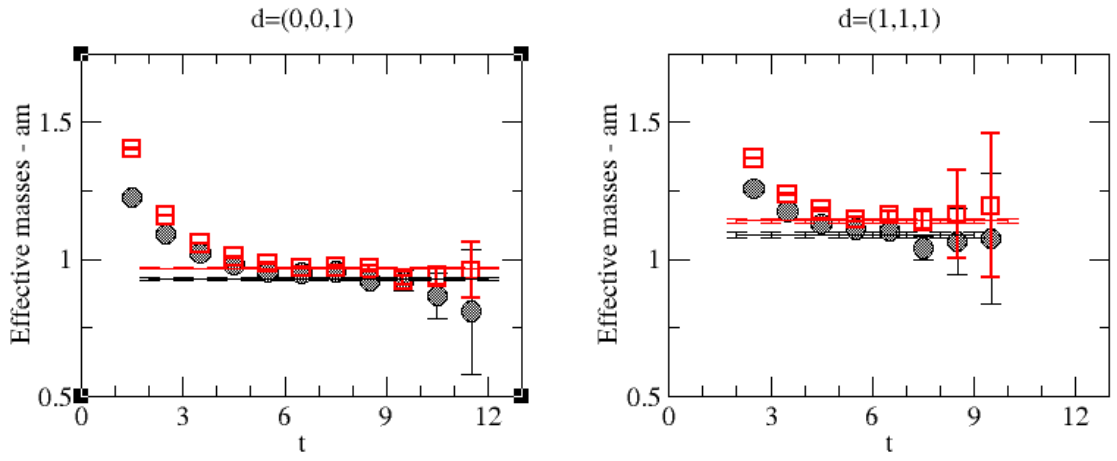

FIGURE 7.4: Effective masses measured in the Δ channel coupled to $N\pi$ in P-wave for different values of the total momentum.

.

7.4 The $\Delta(1232)$ resonance

In this section we present the analysis of the energy levels extracted from the study of the coupled $\Delta - N\pi$ system in P-wave, performed using five interpolators $\{\mathcal{O}_1, \mathcal{O}_2, \mathcal{O}_3, \mathcal{O}_4, \mathcal{O}_5\}$ as defined in Eq.(7.7) and Eq.(7.10). For the calculation all the possible Wick contractions have been taken into account (see Appendix D for a comprehensive list).

We have evaluated the first two energy levels of the low lying spectrum of the $\Delta \to N\pi$ system in two different total momentum frames: $\mathbf{d} = (0,0,1)$ and $\mathbf{d} = (1,1,1)$.

The eigenvector composition and the numerical values of these energy levels leave no doubts about their nature: we are looking at $\Delta(1232)$ (black signal in Fig.7.4) and the $N\pi$ in P_{33} wave (red signal in Fig. 7.4). When the $N\pi$ interpolators are included the $N\pi$ level appears and no sensible shift on the other state is observed (as on the contrary was observed for the N^* states in Chapter 5).

The values of E_n measured on the lattice (see Table 7.1) are plugged into the phase shift equations computed in Section 7.2 and the phase shift is extracted.
Using a Breit Wigner parametrization of the resonance we can now proceed to extract its parameters, even though it is clear from the phase shift behavior (see Fig. 7.5) that the width will be much smaller than the experimental one.

The resonance appears to be extremely narrow and squeezed at the right end of the expected *interesting region*. This can be explained with the fact that, due to the kinematics

$\vec{d}$	level	aE_n	$a^2 s$	fit range	$\frac{\chi^2}{d.o.f.}$	ρ	δ [rad]
$\mathbf{d} = (0,0,1)$	1st	0.927(5)	0.725	2-10	7.8/5	0.014(12)	0.016(2)
$\mathbf{d} = (0,0,1)$	2nd	0.968(3)	0.805	2-9	4.1/4	-0.009(4)	2.867(33)
$\mathbf{d} = (1,1,1)$	1st	1.088(10)	0.794	2-9	10.7/6	-0.0021(1)	2.38(16)
$\mathbf{d} = (1,1,1)$	2nd	1.139(8)	0.915	2-9	1.93/5	–	–

TABLE 7.1: Final results for the lower two energy levels of the coupled $\Delta - N\pi$ system (relative to two exponential fits). The values of s have been computed using the lattice dispersion relation of Eq. (4.20). The last state is not included in the phase shift analysis since it is too far from the energy region of interest. The second and third state enter the analysis with the real part of the phase shift.

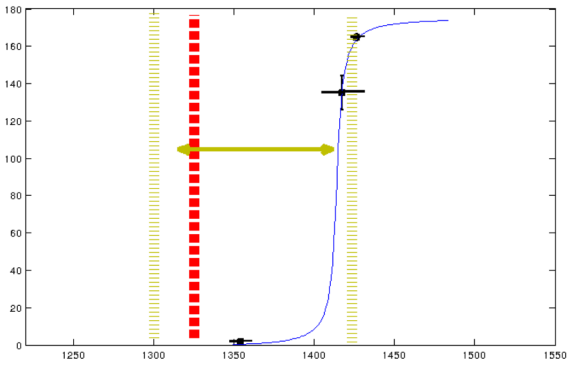

FIGURE 7.5: Values of the phase shift computed using the phase shift formula (black points). The green horizontal arrow indicates the energy range that we identified as the *interesting energy region*. The red vertical dashed line represents the $N\pi$ threshold.

of our system and the unphysical pion mass, the Δ resonance lies too close to the $N\pi$ threshold, which artificially affect its properties.

For convenience we define

$$\rho(s) = \frac{(p^*)^3}{\sqrt{s}} \cot(\delta) \tag{7.11}$$

from which we extract the value of the resonance mass $m_R = 1396(19)$ MeV.
The value of the coupling constant is computed as

$$g^2 = (s_R - s)\frac{6\pi}{\rho(s)} \tag{7.12}$$

and leads to the value $g_{N\pi\Delta} = 9.2(4)$ which is 40% off from the physical value $(g_{phys}) \sim 16$. As a consequence the width computed from

$$\Gamma = \frac{(p^*)^3(s_R)}{s_R}\frac{g^2}{6\pi} \tag{7.13}$$

turns out to be too narrow as expected (~ 11 MeV).

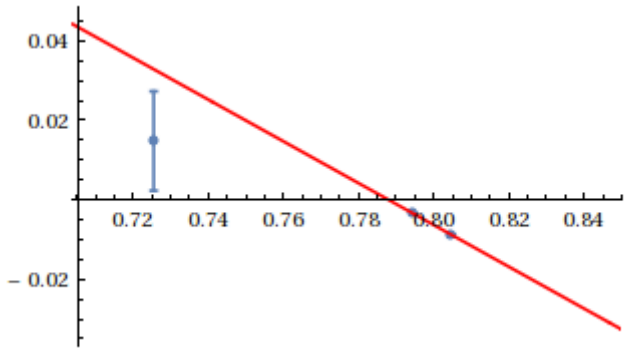

FIGURE 7.6: Values of $\rho(s)$. The red line represents the fit we have used to extract the resonance parameters.

To conclude we perform an effective range parametrization near threshold form which we extract the P_{33} scattering length (or more appropriately *scattering volume*)

$$\sqrt{s}\,\rho(s) = \frac{1}{a} + O(p^{*2}) \tag{7.14}$$

and we obtain the value of $a_{33}m_\pi^2 = 0.29(5)$ which is compatible with the experimental one: $a_{33}m_\pi^2 = 0.214$.

7.5 Conclusions

In this chapter we have presented the results of the study of the coupled $\Delta - N\pi$ channel. The two-particle P-wave is introduced in the system and the resulting spectrum is used to evaluate the properties of the Δ resonance as well as the scattering length. We obtain a physical value for a_{33}, while the picture arising from the study of the resonance is unphysical: what we observe on the lattice is a very narrow resonance squeezed at the far upper end of the energy region which we expected to be influenced by the resonance (the *interesting region:* $M \pm \Gamma/2$), considering its experimental width. The reason for this behavior could be hidden in the kinematics of the system: due to our unphysical pion mass and the coarseness of our lattice, the $N\pi$ threshold lies too close to the Δ resonance to give a realistic picture of the latter. Additional studies on different ensemble would be needed to extract the physical value Γ. Nevertheless the assumption made in Sections 7.1 and 7.2 concerning the possibility of simplifying the phase shift seems to lead to a valid picture of the system and can be used in further studies, since it implies a considerable cut in the computational costs.

Summary

In this work we have focused our attention on the study of the pion-nucleon system in the context of lattice QCD, which allows to perform ab initio calculation and compute predictions starting from a discretized version of Quantum Chromodynamics. The interest in the $N\pi$ system is due to its role as decay product of most of the baryon resonances in the low lying energy spectrum of QCD. These resonances have been traditionally treated as stable states in lattice studies and here for the first time we explicitly include their decay product in the analyzed system.

The process of extracting resonance parameters on the lattice is extremely difficult: it requires the determination of the phase shift from the discrete spectrum, which turns out to be a hard task due to the few available data points and the complications due to eventual moving frames. Despite the technical limits of the approach, we study three different (J, I) channels and we shed some light on diverse properties of the studied resonances.

In the negative parity nucleon sector (see Chapter 5) we show that the inclusion of $(4 + 1)$-quark interpolators is crucial for a reliable picture of the spectrum: using only 3-quark operator is not sufficient for describing the N^* states.

In Chapter 6 we study the pion-nucleon scattering in S-wave and we perform a qualitative analysis of the results. We observe the presence of an unexpected energy level when $N\pi$ interpolators are included in the analysis and we explain that this could be a candidate for the Roper resonance.

Chapter 7 is devoted to the study of the $\Delta(1232)$ resonance. The vicinity between the resonance and the $N\pi$ threshold (due to the unphysical pion mass) determines a squeezing of the resonance width, however the mass extracted is compatible with the expected value.

This work is meant to be a first step in the direction of reproducing the properties of baryon resonances in LQCD, which still represents an outstanding challenge.

Appendix A

Dirac matrices

The Dirac matrices on a four dimensional Euclidean space can be derived from the Minkowski gamma matrices. They obey the anti-commutation relation

$$\{\gamma_\mu, \gamma_\nu\} = 2g_{\mu\nu}\mathbb{1}, \tag{A.1}$$

where $g_{\mu\nu} = \delta_{\mu\nu}$ in the Euclidean space and $\mu = 1, 2, 3, 4$ (the fourth component represents by convention the temporal direction). The gamma matrices obey

$$\gamma_\mu = \gamma_\mu^\dagger = \gamma_\mu^{-1}. \tag{A.2}$$

We adopt the chiral representation of the gamma matrices where

$$\gamma_5 = \gamma_1\gamma_2\gamma_3\gamma_4 \tag{A.3}$$

is diagonal. In addition we recall that

$$\gamma_5^2 = \mathbb{1} \quad \text{and} \quad \{\gamma_5, \gamma_\mu\} = 0 \quad \forall\, \mu. \tag{A.4}$$

The charge conjugation matrix is defined as

$$C = i\gamma_2\gamma_4, \tag{A.5}$$

with

$$C\gamma_\mu C^{-1} = -\gamma_m u^T. \tag{A.6}$$

In the chiral representation the gamma matrices read

$$\gamma_1 = \begin{bmatrix} 0 & 0 & 0 & -i \\ 0 & 0 & -i & 0 \\ 0 & i & 0 & 0 \\ i & 0 & 0 & 0 \end{bmatrix}, \gamma_2 = \begin{bmatrix} 0 & 0 & 0 & -1 \\ 0 & 0 & 1 & 0 \\ 0 & 1 & 0 & 0 \\ -1 & 0 & 0 & 0 \end{bmatrix}, \gamma_3 = \begin{bmatrix} 0 & 0 & -i & 0 \\ 0 & 0 & 0 & i \\ i & 0 & 0 & 0 \\ 0 & -i & 0 & 0 \end{bmatrix},$$

$$\gamma_4 = \begin{bmatrix} 0 & 0 & 1 & 0 \\ 0 & 0 & 0 & 1 \\ 1 & 0 & 0 & 0 \\ 0 & 1 & 0 & 0 \end{bmatrix}, \gamma_5 = \begin{bmatrix} 1 & 0 & 0 & 0 \\ 0 & 1 & 0 & 0 \\ 0 & 0 & -1 & 0 \\ 0 & 0 & 0 & -1 \end{bmatrix}.$$

Appendix B

Interpolator properties under parity transformations

The action of the parity transformation P on the fermionic fields is defined as follows

$$\psi(\vec{x}) \longrightarrow \gamma_4 \psi(-\vec{x}), \tag{B.1}$$

$$\bar{\psi}(\vec{x}) \longrightarrow \bar{\psi}(-\vec{x})\gamma_4. \tag{B.2}$$

The effect of P on different particle interpolators has to be computed case by case in order to ensure that the chosen operator has the correct quantum numbers of the particle it couples to.

B.0.1 The 3-quark N interpolator

We define the nucleon interpolator as

$$N^{(i)}(\vec{x}) = \Gamma_1^{(i)}\, u(\vec{x})\, u^T(\vec{x})\, \Gamma_2^{(i)}\, d(\vec{x}). \tag{B.3}$$

With different Dirac structures (i.e. different combinations of (Γ_1, Γ_2)), antisymmetrization on the (omitted) color indices and eventual isospin symmetrization are implied. Under parity transformation it transforms as

$$P: \qquad N^{(i)}(\vec{x}) \longrightarrow \Gamma_1^{(i)}\, \gamma_4 u(-\vec{x})\, u^T(-\vec{x})\gamma_4\, \Gamma_2^{(i)}\, \gamma_4 d(-\vec{x}) = \tag{B.4}$$

$$= s_1 s_2\ \gamma_4 \Gamma_1^{(i)}\, u(-\vec{x})\, u^T(-\vec{x})\, \Gamma_2^{(i)}\, d(-\vec{x}), \tag{B.5}$$

where

$$\Gamma_1\gamma_4 = s_1\gamma_4\Gamma_1 \qquad \text{and} \qquad \Gamma_2\gamma_4 = s_2\gamma_4\Gamma_2. \tag{B.6}$$

$$\tag{B.7}$$

To summarize

$$P: \qquad N^{(i)}(\vec{x}) \longrightarrow \gamma_4 N^{(i)}(-\vec{x}). \tag{B.8}$$

It is only the momentum projection to $\vec{p} = \vec{0}$ that ensures parity to be a definite quantum number for this interpolator:

$$N(\vec{p}) = \sum_x e^{-ipx} N(\vec{x}) \longrightarrow \gamma_4 \sum_x e^{ipx} N(\vec{x}), \tag{B.9}$$

$$N(\vec{0}) \longrightarrow \gamma_4 N(\vec{0}). \tag{B.10}$$

Therefore the interpolators for positive and negative parity nucleons at rest read

$$(N^{(i)}_{\pm})_\mu = \sum_{\vec{x}} \epsilon_{abc} \left(P_\pm \, \Gamma_1^{(i)} \, u_a(\vec{x}) \right)_\mu u_b^T(\vec{x}) \, \Gamma_2^{(i)} \, d_c(\vec{x}), \tag{B.11}$$

with $P_\pm = (1 \pm \gamma_4)/2$.
An analogous calculation can be done for the delta baryon interpolator leading to the same results.

B.0.2 The $N\pi$ interpolator with zero momentum

The $N\pi$ interpolator is constructed from the single particle N and π interpolators.
The pion interpolator transforms under parity as

$$\pi(\vec{x}) = \bar{u}(\vec{x})\gamma_5 d(\vec{x}) \longrightarrow -\bar{u}(-\vec{x})\gamma_5 d(-\vec{x}) \tag{B.12}$$

and after zero momentum projection $\pi(\vec{p})$ has definite negative parity

$$P: \qquad \pi(\vec{p}) \longrightarrow -\pi(\vec{p}). \tag{B.13}$$

The pion-nucleon interpolator can be naively written as

$$O_{N\pi}(\vec{p}) = \sum_x N(\vec{x}) e^{-ipx} \sum_y \pi(\vec{x}) e^{-ipy} \tag{B.14}$$

which, after projection to zero momentum, transforms under parity as

$$O_{N\pi}(\vec{0}) \longrightarrow -\gamma_4 N(\vec{0})\pi(\vec{0}), \tag{B.15}$$

or equivalently

$$O^{\pm}_{N\pi} = P_{\mp} N\pi. \tag{B.16}$$

Since we aim to evaluate the correlation function of the coupled system $\{N, N\pi\}$, we need $O_{N\pi}$ to transform under parity in the same way of N, otherwise the off diagonal terms of the correlation function will artificially vanish due to the mutual annihilation of the parity projectors. For example the matrix element related to the negative parity nucleon would read

$$\langle P_- N | P_+ N\pi \rangle = 0. \tag{B.17}$$

We decide to insert an extra γ_5 in our definition of $O_{N\pi}$ so that it transforms according to N under parity transformations:

$$O^{\pm}_{N\pi} = P_{\pm}\gamma_5 N\pi. \tag{B.18}$$

In this way the diagonal two-particle correlator stays unchanged and the off-diagonal terms do not vanish:

$$\langle P_+ N\pi | P_+ N\pi \rangle = \langle P_-\gamma_5 N\pi | P_-\gamma_5 N\pi \rangle, \tag{B.19}$$

$$\langle P_- N | P_-\gamma_5 N\pi \rangle \neq 0. \tag{B.20}$$

B.0.3 Parity transformations in non-rest frame

We have already mentioned that parity represents a good quantum number only after a projection to zero momentum. Now we address the issue of defining a particle interpolator in a non-rest frame.

For single particle interpolators we have seen that

$$N(\vec{p}) \longrightarrow \gamma_4 N(-\vec{p}) \qquad \text{and} \qquad \pi(\vec{p}) \longrightarrow -\pi(-\vec{p}) \tag{B.21}$$

do not have definite parity. The same happens to two-particle interpolators with non-zero momenta:

$$N(\vec{p_1})\pi(\vec{p_2}) \longrightarrow -\gamma_4 N(-\vec{p_1})\pi(-\vec{p_2}). \tag{B.22}$$

If the system is in a rest-frame and $\vec{p_1} = -\vec{p_2}$ then

$$N(\vec{p_1})\pi(-\vec{p_1}) + \gamma_4 N(-\vec{p_1})\pi(\vec{p_1}) \tag{B.23}$$

still has definite parity. In all the other cases it is not possible to find a combination of interpolators that preserves such properties. For this reason we avoid parity projection in all the studies which involve moving systems.

Appendix C

Isospin projection

C.1 Isospin states

We define the appropriate isospin operators

$$I_+, I_-, I_3 \tag{C.1}$$

via their commutation relations

$$[I_+, I_-] = 2I_3, \qquad [I_3, I_\pm] = \pm I_\pm \tag{C.2}$$

and their action on the quantum states

$$\begin{aligned}
&I_+|u\rangle = 0 \qquad I_-|u\rangle = |d\rangle \qquad I_3|u\rangle = \frac{1}{2}|u\rangle \\
&I_+|d\rangle = |u\rangle \qquad I_-|d\rangle = 0 \qquad I_3|d\rangle = -\frac{1}{2}|d\rangle \\
&I_+|\bar{d}\rangle = 0 \qquad I_-|\bar{d}\rangle = -|\bar{u}\rangle \qquad I_3|\bar{d}\rangle = \frac{1}{2}|\bar{d}\rangle \\
&I_+|\bar{u}\rangle = -|\bar{d}\rangle \qquad I_-|\bar{u}\rangle = 0 \qquad I_3|\bar{u}\rangle = -\frac{1}{2}|\bar{u}\rangle.
\end{aligned} \tag{C.3}$$

The properties of isospin states arise from the commutation relation and can be classified in multiplets of $2I + 1$ states $|I, I_3\rangle$ which are simultaneous eigenstates of the operators I_3 and

$$I^2 = \frac{1}{2}[I_+I_- + I_-I_+] + I_3^2, \tag{C.4}$$

so that

$$I^2|I, I_3\rangle = I(I+1)|I, I_3\rangle, \qquad I_3|I, I_3\rangle = I_3|I, I_3\rangle. \tag{C.5}$$

We define the basic quark and antiquark isodublet

$$(u, d) \qquad (\bar{d}, -\bar{u}) \tag{C.6}$$

as

$$|u\rangle = |\frac{1}{2}.\frac{1}{2}\rangle \qquad |d\rangle = |\frac{1}{2}.-\frac{1}{2}\rangle \tag{C.7}$$

$$|\bar{d}\rangle = |\frac{1}{2}.\frac{1}{2}\rangle \qquad |\bar{u}\rangle = -|\frac{1}{2}.-\frac{1}{2}\rangle. \tag{C.8}$$

The pions form an isotriplet of states with $I = 1$ and $I_3 = \{1, 0, -1\}$.
We start constructing the first state of the isotriplet with the largest value of I_3

$$|1, 1\rangle = \bar{d}u, \tag{C.9}$$

then we use the operator I_- to decrease I_3 and we obtain the next state:

$$I_-|1, 1\rangle = \sqrt{2}|1, 0\rangle, \tag{C.10}$$

$$I_-(\bar{d}u) = I_-(\bar{d})u + \bar{d}I_-(u) = -\bar{u}u + \bar{d}d, \tag{C.11}$$

$$|1, 0\rangle = \frac{1}{\sqrt{2}}(\bar{d}d - \bar{u}u). \tag{C.12}$$

Acting again on both sides with I_- leads to

$$|1, -1\rangle = \bar{u}d. \tag{C.13}$$

Note that an overall sign can be arbitrarily added.
Each state is assigned to one of the pions

$$\pi_+ = \bar{d}u, \qquad \pi_0 = \frac{1}{\sqrt{2}}(\bar{u}u - \bar{d}d), \qquad \pi_- = \bar{u}d, \tag{C.14}$$

and the isotriplet reads

$$(\pi_+, -\pi_0, \pi_-). \tag{C.15}$$

We use the same approach to define the $I = 1/2$ baryons as

$$P = uud = |\frac{1}{2}, \frac{1}{2}\rangle, \qquad N = dud = |\frac{1}{2}, -\frac{1}{2}\rangle, \tag{C.16}$$

where P and N are respectively the proton (with electric charge +1) and the neutron (neutral electric charge).
Analogously the $I = 3/2$ states are

$$\Delta^{++} = |\frac{3}{2}, \frac{3}{2}\rangle, \qquad \Delta^{+} = |\frac{3}{2}, \frac{1}{2}\rangle, \tag{C.17}$$

$$\Delta^{0} = |\frac{3}{2}, -\frac{1}{2}\rangle, \qquad \Delta^{-} = |\frac{3}{2}, -\frac{3}{2}\rangle. \tag{C.18}$$

The total isospin (as well as the angular momentum) can be expanded as

$$|(j_1, j_2), J, M\rangle = \sum_{m_1, m_2} \langle j_1 m_1; j_2 m_2 | JM\rangle |j_1 m_1 j_2 m_2\rangle, \tag{C.19}$$

where $|j_1 m_1 j_2 m_2\rangle = |j_1 m_1\rangle |j_2 m_2\rangle$ and $CG(j_1, m_1, j_2, m_2) = \langle j_1 m_1; j_2 m_2 | JM\rangle$ are the Clebsch-Gordan coefficients.

In this convention the proton couples to

$$|\frac{1}{2}, \frac{1}{2}\rangle = \sqrt{\frac{2}{3}}\pi_+ N + \sqrt{\frac{1}{3}}\pi_0 P, \tag{C.20}$$

while the delta couples to

$$|\frac{3}{2}, \frac{3}{2}\rangle = \pi_+ P. \tag{C.21}$$

C.2 Isospin symmetrization

In our calculation we have always used interpolators for the nucleon which are not isospin symmetrized. This follows from some considerations concerning the symmetries of the gamma matrices. If the quarks u and d are smeared in different ways, the interpolator for the charged nucleon would read

$$N^{\alpha}_{\pm} = \epsilon_{abc} (P_{\pm} \Gamma^{(1)} u_a)^{\alpha} (u_{b\beta}\, \Gamma^{(2)}_{\beta\gamma}\, d_{c\gamma} - d_{b\beta}\, \Gamma^{(2)}_{\beta\gamma}\, u_{c\gamma}). \tag{C.22}$$

On the contrary no isospin symmetrization is needed if the fermionic fields are all subject to the same type of smearing: the second term results identical to the first due to

$$-\epsilon_{abc}\, d_{b\beta}\, \Gamma^{(2)}_{\beta\gamma}\, u_{c\gamma} \;=\; \epsilon_{abc}\, u_{c\gamma}\, \Gamma^{(2)}_{\beta\gamma}\, d_{b\beta} \;=\; \epsilon_{acb}\, u_{b\gamma}\, \Gamma^{(2)}_{\beta\gamma}\, d_{c\beta} \;=\; -\epsilon_{abc}\, u_{b\gamma}\, \Gamma^{(2)}_{\beta\gamma}\, d_{c\beta} \;= \tag{C.23}$$

$$-\epsilon_{abc}\, u_{b\beta}\, \Gamma^{(2)}_{\gamma\beta}\, d_{c\gamma} \;=\; -\epsilon_{abc}\, u_{b\beta}\, {\Gamma^{(2)}_{\beta\gamma}}^{T}\, d_{c\gamma} \;=\; \epsilon_{abc}\, u_{b\beta}\, \Gamma^{(2)}_{\beta\gamma}\, d_{c\gamma}, \tag{C.24}$$

which has been obtained using the following steps: Grassmann variables properties, color anti-symmetry, renaming of the Dirac indices and antisymmetry of $\Gamma^{(2)}$ (valid for every $N^{(i)}$ in this work).

Appendix D

Wick contractions

Notation for the perambulators used in this section: $\tau\,(t, t', a, a', \alpha, \alpha')$ denotes the perambulator $\tau_{\alpha\alpha'}(a, t; a', t')$ from (3.20), i.e., from source at t' (source vector a', Dirac index α') to the sink at t (source vector a, Dirac index α).

Each source/sink nucleon contributes a factor of the form $\widehat{\phi}_N(a, b, c)$, which is constructed from the Laplacian eigenvectors. For a given time slice we have

$$\widehat{\phi}_N^{snk}(a, b, c) = \sum_{\vec{x},i,j,k} \epsilon_{ijk} v_a^i(\vec{x}) v_b^j(\vec{x}) v_c^k(\vec{x}) \;, \tag{D.1}$$

where ϵ denotes the Levi-Civita symbol, v are the Laplacian eigenvectors, and the sum runs over all sites of the time slice and over the color indices i, j, k. The corresponding factor for the pion $\widehat{\phi}_\pi(a, b)$ on a given time slice reads

$$\widehat{\phi}_\pi^{snk}(a, b) = \sum_{\vec{x},i,j} \delta_{ij} v_a^{i*}(\vec{x}) v_b^j(\vec{x}) \;. \tag{D.2}$$

By permuting and renaming the Dirac indices $\alpha, \beta, \gamma, \ldots$ and the eigenvector indices $a, b, c, \ldots$ we group the different contractions such that they have a common prefactor. There also the gamma matrices of the nucleon and pion and the parity projection operators $P^{\pm}$ are located.

D.1 Nucleon $(I = 1/2)$

D.1.1 $N \to N$

This entry has the form

$$\Gamma^{A}_{\alpha'\mu} P^{\pm}_{\mu\nu} \Gamma^{A\dagger}_{\nu\alpha} \Gamma^{B}_{\beta\gamma} \Gamma^{B\dagger}_{\gamma'\beta'} \widehat{\phi}^{snk}_{N}(a,b,c) \widehat{\phi}^{src}_{N}(a',b',c') \sum_{i=1}^{2} A_i \ , \tag{D.3}$$

where summation over index pairs is implied.

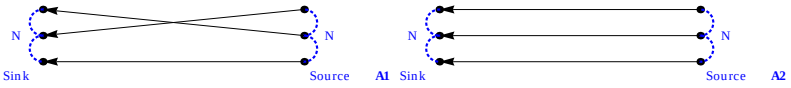

FIGURE D.1: Terms A_1 and A_2 contributing to $N \to N$.

$$\begin{aligned} A_1 &= \tau\left(t,t',c,c',\gamma,\gamma'\right) \tau\left(t,t',a,b',\alpha,\beta'\right) \tau\left(t,t',b,a',\beta,\alpha'\right) \\ A_2 &= -\tau\left(t,t',a,a',\alpha,\alpha'\right) \tau\left(t,t',b,b',\beta,\beta'\right) \tau\left(t,t',c,c',\gamma,\gamma'\right) \end{aligned} \tag{D.4}$$

D.1.2 $N \to N\pi$

This matrix element has 4 terms contributing:

$$\frac{1}{\sqrt{2}} \Gamma^{A\dagger}_{\alpha'\mu} P^{\pm}_{\mu\nu} \Gamma^{A}_{\nu\alpha} \Gamma^{B}_{\beta\gamma} \Gamma^{B\dagger}_{\gamma'\beta'} \Gamma^{\pi}_{\delta\epsilon} \widehat{\phi}^{snk}_{N}(a,b,c) \ \widehat{\phi}^{snk}_{\pi}(e,g) \widehat{\phi}^{src}_{N}(a',b',c') \sum_{i=1}^{4} B_i \ , \tag{D.5}$$

where summation over index pairs is implied.

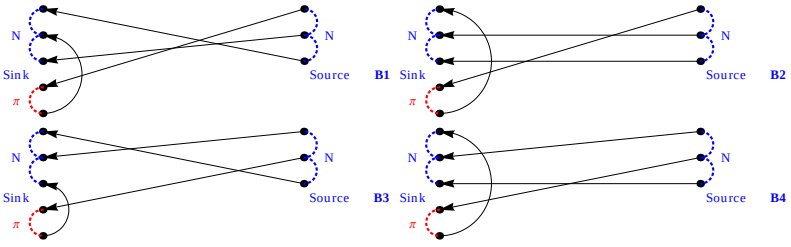

FIGURE D.2: Terms $B_1 - B_4$ contributing to $N \to N\pi$.

$$
\begin{aligned}
B_1 &= 3\,\tau\left(t,t,b,e,\beta,\epsilon\right)\,\tau\left(t,t',a,c',\alpha,\gamma'\right)\,\tau\left(t,t',g,a',\delta,\alpha'\right)\,\tau\left(t,t',c,b',\gamma,\beta'\right)\\
B_2 &= -3\,\tau\left(t,t',b,b',\beta,\beta'\right)\,\tau\left(t,t',c,c',\gamma,\gamma'\right)\,\tau\left(t,t,a,e,\alpha,\epsilon\right)\,\tau\left(t,t',g,a',\delta,\alpha'\right)\\
B_3 &= -3\,\tau\left(t,t,c,e,\gamma,\epsilon\right)\,\tau\left(t,t',b,a',\beta,\alpha'\right)\,\tau\left(t,t',a,c',\alpha,\gamma'\right)\,\tau\left(t,t',g,b',\delta,\beta'\right)\\
B_4 &= 3\,\tau\left(t,t',c,c',\gamma,\gamma'\right)\,\tau\left(t,t,a,e,\alpha,\epsilon\right)\,\tau\left(t,t',b,a',\beta,\alpha'\right)\,\tau\left(t,t',g,b',\delta,\beta'\right)
\end{aligned}
\tag{D.6}
$$

D.1.3 $N\pi \to N$

This matrix element has 4 terms contributing:

$$
\frac{1}{\sqrt{2}}\,\Gamma^{A\dagger}_{\alpha'\mu}P^{\pm}_{\mu\nu}\Gamma^{A}_{\nu\alpha}\Gamma^{B}_{\beta\gamma}\Gamma^{B\dagger}_{\gamma'\beta'}\Gamma^{\pi\dagger}_{\epsilon'\delta'}\;\;\widehat{\phi}^{snk}_{N}(a,b,c)\widehat{\phi}^{src}_{N}(a',b',c')\widehat{\phi}^{src}_{\pi}(g',e')\,\sum_{i=1}^{4}C_i\;, \tag{D.7}
$$

where summation over index pairs is implied.

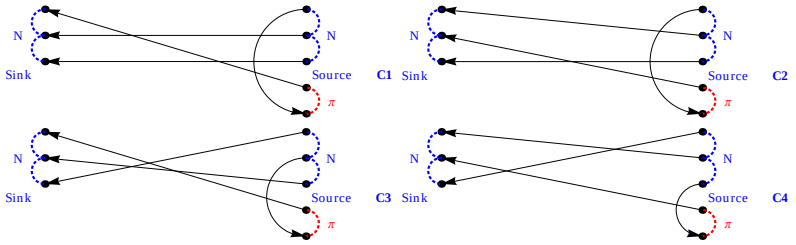

FIGURE D.3: Terms $C_1 - C_4$ contributing to $N\pi \to N$.

$$
\begin{aligned}
C_1 &= 3\,\tau\left(t,t',b,b',\beta,\beta'\right)\,\tau\left(t,t',c,c',\gamma,\gamma'\right)\,\tau\left(t',t',e',a',\epsilon',\alpha'\right)\,\tau\left(t,t',a,g',\alpha,\delta'\right)\\
C_2 &= -3\,\tau\left(t,t',c,c',\gamma,\gamma'\right)\,\tau\left(t,t',a,b',\alpha,\beta'\right)\,\tau\left(t',t',e',a',\epsilon',\alpha'\right)\,\tau\left(t,t',b,g',\beta,\delta'\right)\\
C_3 &= -3\,\tau\left(t,t',c,a',\gamma,\alpha'\right)\,\tau\left(t,t',a,g',\alpha,\delta'\right)\,\tau\left(t,t',b,c',\beta,\gamma'\right)\,\tau\left(t',t',e',b',\epsilon',\beta'\right)\\
C_4 &= 3\,\tau\left(t,t',a,b',\alpha,\beta'\right)\,\tau\left(t,t',c,a',\gamma,\alpha'\right)\,\tau\left(t,t',b,g',\beta,\delta'\right)\,\tau\left(t',t',e',c',\epsilon',\gamma'\right)
\end{aligned}
\tag{D.8}
$$

D.1.4 $N\pi \to N\pi$ $(I = 1/2)$

Here 19 terms contribute:

$$
\frac{1}{2}\,\Gamma^{A\dagger}_{\alpha'\mu}P^{\pm}_{\mu\nu}\Gamma^{A}_{\nu\alpha}\Gamma^{B}_{\beta\gamma}\Gamma^{B\dagger}_{\gamma'\beta'}\Gamma^{\pi}_{\delta\epsilon}\Gamma^{\pi\dagger}_{\epsilon'\delta'}\;\;\widehat{\phi}^{snk}_{N}(a,b,c)\widehat{\phi}^{snk}_{\pi}(e,g)\widehat{\phi}^{src}_{N}(a',b',c')\widehat{\phi}^{src}_{\pi}(g',e')\,\sum_{i=1}^{19}D_i\;, \tag{D.9}
$$

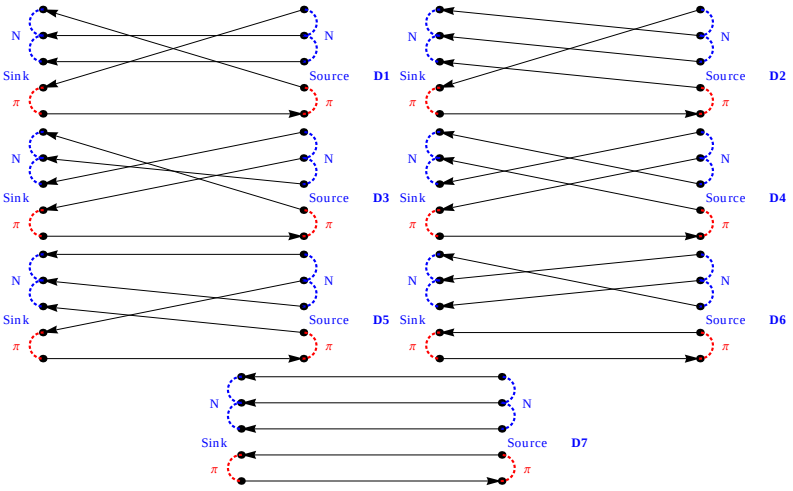

FIGURE D.4: Terms $D_1 - D_7$ contributing to $N\pi \to N\pi$.

where summation over index pairs is implied.

$$
\begin{aligned}
D_1 &= 3\,\tau\left(t,t',b,b',\beta,\beta'\right)\,\tau\left(t,t',c,c',\gamma,\gamma'\right)\,\tau\left(t',t,e',e,\epsilon',\epsilon\right)\\
&\quad\tau\left(t,t',a,g',\alpha,\delta'\right)\,\tau\left(t,t',g,a',\delta,\alpha'\right)\\
D_2 &= -3\,\tau\left(t',t,e',e,\epsilon',\epsilon\right)\,\tau\left(t,t',a,b',\alpha,\beta'\right)\,\tau\left(t,t',g,a',\delta,\alpha'\right)\\
&\quad\tau\left(t,t',b,c',\beta,\gamma'\right)\,\tau\left(t,t',c,g',\gamma,\delta'\right)\\
D_3 &= -3\,\tau\left(t',t,e',e,\epsilon',\epsilon\right)\,\tau\left(t,t',c,a',\gamma,\alpha'\right)\,\tau\left(t,t',a,g',\alpha,\delta'\right)\\
&\quad\tau\left(t,t',b,c',\beta,\gamma'\right)\,\tau\left(t,t',g,b',\delta,\beta'\right)\\
D_4 &= 9\,\tau\left(t',t,e',e,\epsilon',\epsilon\right)\,\tau\left(t,t',a,c',\alpha,\gamma'\right)\,\tau\left(t,t',c,a',\gamma,\alpha'\right)\\
&\quad\tau\left(t,t',b,g',\beta,\delta'\right)\,\tau\left(t,t',g,b',\delta,\beta'\right)\\
D_5 &= -6\,\tau\left(t,t',a,a',\alpha,\alpha'\right)\,\tau\left(t',t,e',e,\epsilon',\epsilon\right)\,\tau\left(t,t',b,c',\beta,\gamma'\right)\\
&\quad\tau\left(t,t',g,b',\delta,\beta'\right)\,\tau\left(t,t',c,g',\gamma,\delta'\right)\\
D_6 &= -6\,\tau\left(t',t,e',e,\epsilon',\epsilon\right)\,\tau\left(t,t',g,g',\delta,\delta'\right)\,\tau\left(t,t',b,a',\beta,\alpha'\right)\\
&\quad\tau\left(t,t',a,c',\alpha,\gamma'\right)\,\tau\left(t,t',c,b',\gamma,\beta'\right)\\
D_7 &= 6\,\tau\left(t,t',a,a',\alpha,\alpha'\right)\,\tau\left(t,t',b,b',\beta,\beta'\right)\,\tau\left(t,t',c,c',\gamma,\gamma'\right)\\
&\quad\tau\left(t',t,e',e,\epsilon',\epsilon\right)\,\tau\left(t,t',g,g',\delta,\delta'\right)
\end{aligned}
\tag{D.10}
$$

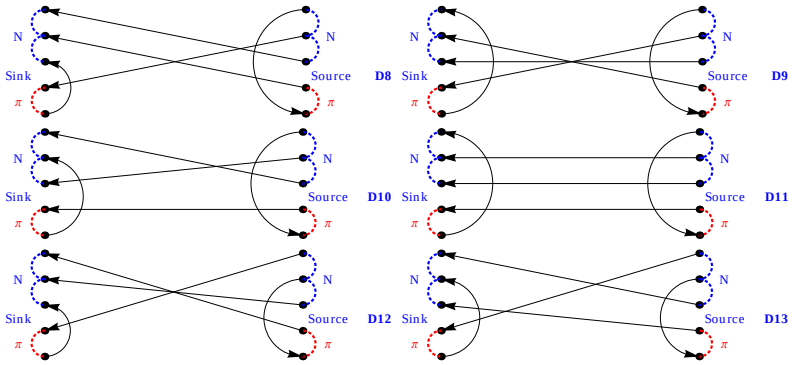

FIGURE D.5: Terms $D_8 - D_{13}$ contributing to $N\pi \to N\pi$

$$
\begin{aligned}
D_8 &= -9\,\tau\left(t,t,c,e,\gamma,\epsilon\right)\,\tau\left(t,t',a,c',\alpha,\gamma'\right)\,\tau\left(t',t',e',a',\epsilon',\alpha'\right)\\
&\quad\ \tau\left(t,t',b,g',\beta,\delta'\right)\,\tau\left(t,t',g,b',\delta,\beta'\right)\\
D_9 &= 9\,\tau\left(t,t',c,c',\gamma,\gamma'\right)\,\tau\left(t,t,a,e,\alpha,\epsilon\right)\,\tau\left(t',t',e',a',\epsilon',\alpha'\right)\\
&\quad\ \tau\left(t,t',b,g',\beta,\delta'\right)\,\tau\left(t,t',g,b',\delta,\beta'\right)\\
D_{10} &= 9\,\tau\left(t,t',g,g',\delta,\delta'\right)\,\tau\left(t,t,b,e,\beta,\epsilon\right)\,\tau\left(t,t',a,c',\alpha,\gamma'\right)\\
&\quad\ \tau\left(t',t',e',a',\epsilon',\alpha'\right)\,\tau\left(t,t',c,b',\gamma,\beta'\right)\\
D_{11} &= -9\,\tau\left(t,t',b,b',\beta,\beta'\right)\,\tau\left(t,t',c,c',\gamma,\gamma'\right)\,\tau\left(t,t',g,g',\delta,\delta'\right)\\
&\quad\ \tau\left(t,t,a,e,\alpha,\epsilon\right)\,\tau\left(t',t',e',a',\epsilon',\alpha'\right)\\
D_{12} &= -3\,\tau\left(t,t,c,e,\gamma,\epsilon\right)\,\tau\left(t,t',a,g',\alpha,\delta'\right)\,\tau\left(t,t',g,a',\delta,\alpha'\right)\\
&\quad\ \tau\left(t,t',b,c',\beta,\gamma'\right)\,\tau\left(t',t',e',b',\epsilon',\beta'\right)\\
D_{13} &= 3\,\tau\left(t,t,b,e,\beta,\epsilon\right)\,\tau\left(t,t',a,c',\alpha,\gamma'\right)\,\tau\left(t,t',g,a',\delta,\alpha'\right)\\
&\quad\ \tau\left(t',t',e',b',\epsilon',\beta'\right)\,\tau\left(t,t',c,g',\gamma,\delta'\right)
\end{aligned}
\tag{D.11}
$$

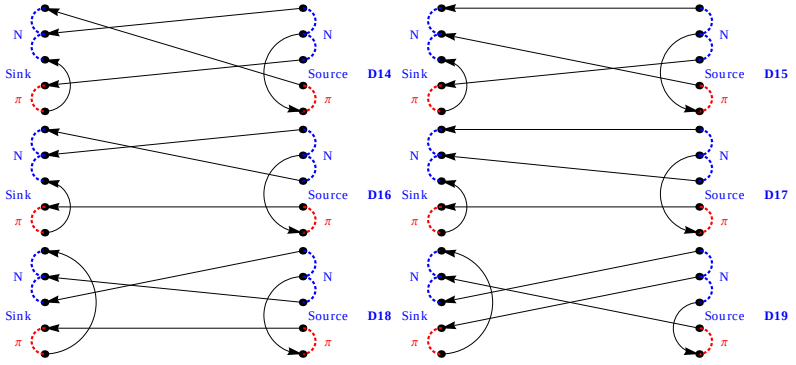

FIGURE D.6: Terms $D_{14} - D_{19}$ contributing to $N\pi \to N\pi$

$$
\begin{aligned}
D_{14} &= 3\,\tau\left(t,t,c,e,\gamma,\epsilon\right)\,\tau\left(t,t',b,a',\beta,\alpha'\right)\,\tau\left(t,t',a,g',\alpha,\delta'\right)\\
&\quad\tau\left(t',t',e',b',\epsilon',\beta'\right)\,\tau\left(t,t',g,c',\delta,\gamma'\right)\\
D_{15} &= 6\,\tau\left(t,t',a,a',\alpha,\alpha'\right)\,\tau\left(t,t,c,e,\gamma,\epsilon\right)\,\tau\left(t',t',e',b',\epsilon',\beta'\right)\\
&\quad\tau\left(t,t',b,g',\beta,\delta'\right)\,\tau\left(t,t',g,c',\delta,\gamma'\right)\\
D_{16} &= -3\,\tau\left(t,t',g,g',\delta,\delta'\right)\,\tau\left(t,t,c,e,\gamma,\epsilon\right)\,\tau\left(t,t',b,a',\beta,\alpha'\right)\\
&\quad\tau\left(t,t',a,c',\alpha,\gamma'\right)\,\tau\left(t',t',e',b',\epsilon',\beta'\right)\\
D_{17} &= -6\,\tau\left(t,t',a,a',\alpha,\alpha'\right)\,\tau\left(t,t',g,g',\delta,\delta'\right)\,\tau\left(t,t,c,e,\gamma,\epsilon\right)\\
&\quad\tau\left(t,t',b,c',\beta,\gamma'\right)\,\tau\left(t',t',e',b',\epsilon',\beta'\right)\\
D_{18} &= 9\,\tau\left(t,t',g,g',\delta,\delta'\right)\,\tau\left(t,t,a,e,\alpha,\epsilon\right)\,\tau\left(t,t',c,a',\gamma,\alpha'\right)\\
&\quad\tau\left(t,t',b,c',\beta,\gamma'\right)\,\tau\left(t',t',e',b',\epsilon',\beta'\right)\\
D_{19} &= -9\,\tau\left(t,t,a,e,\alpha,\epsilon\right)\,\tau\left(t,t',c,a',\gamma,\alpha'\right)\,\tau\left(t,t',b,g',\beta,\delta'\right)\\
&\quad\tau\left(t,t',g,b',\delta,\beta'\right)\,\tau\left(t',t',e',c',\epsilon',\gamma'\right)
\end{aligned}
\tag{D.12}
$$

D.2 Delta $(I = 3/2)$

D.2.1 $\Delta \to \Delta$

This entry has the form

$$
P^{\pm}_{\alpha'\alpha}\Gamma^{\Delta}_{\beta\gamma}\Gamma^{\Delta\dagger}_{\gamma'\beta'}\widehat{\phi}^{snk}_{\Delta}(a,b,c)\widehat{\phi}^{src}_{\Delta}(a',b',c')\,\sum_{i=1}^{2}A_i\ , \tag{D.13}
$$

where summation over index pairs is implied.

FIGURE D.7: Terms A_1 and A_2 contributing to $N \to N$.

$$
\begin{aligned}
A_1 &= 4\tau\left(t,t',c,c',\gamma,\gamma'\right)\,\tau\left(t,t',a,b',\alpha,\beta'\right)\,\tau\left(t,t',b,a',\beta,\alpha'\right)\\
A_2 &= -2\tau\left(t,t',a,a',\alpha,\alpha'\right)\,\tau\left(t,t',b,b',\beta,\beta'\right)\,\tau\left(t,t',c,c',\gamma,\gamma'\right)
\end{aligned}
\tag{D.14}
$$

D.2.2 $\Delta \to N\pi$

This matrix element has 3 terms contributing:

$$\frac{1}{\sqrt{2}}\, P^{\pm}_{\alpha'\nu}\Gamma^{A}_{\nu\alpha}\Gamma^{B}_{\beta\gamma}\Gamma^{\Delta\dagger}_{\gamma'\beta'}\Gamma^{\pi}_{\delta\epsilon}\;\; \widehat{\phi}^{snk}_{N}(a,b,c)\widehat{\phi}^{snk}_{\pi}(e,d)\widehat{\phi}^{src}_{\Delta}(a',b',c')\;\sum_{i=1}^{3} B_i\;, \tag{D.15}$$

where summation over index pairs is implied.

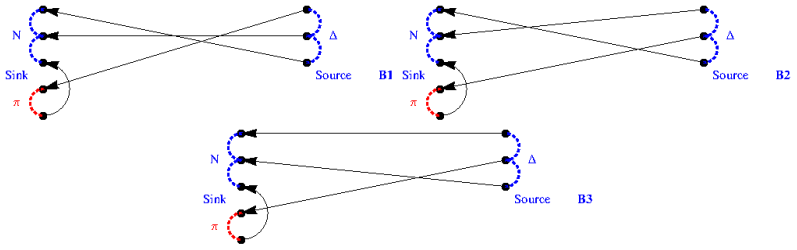

FIGURE D.8: Terms $B_1 - B_3$ contributing to $N \to N\pi$.

$$\begin{aligned}
B_1 &= 2\,\tau\left(t,t,c,e,\gamma,\epsilon\right)\,\tau\left(t,t',a,c',\alpha,\gamma'\right)\,\tau\left(t,t',b,b',\beta,\beta'\right)\,\tau\left(t,t',d,a',\delta,\alpha'\right)\\
B_2 &= -2\,\tau\left(t,t,c,e,\gamma,\epsilon\right)\,\tau\left(t,t',a,c',\alpha,\gamma'\right)\,\tau\left(t,t',b,a',\beta,\alpha'\right)\,\tau\left(t,t',d,b',\delta,\beta'\right)\\
B_3 &= 2\,\tau\left(t,t,c,e,\gamma,\epsilon\right)\,\tau\left(t,t',a,c',\alpha,\gamma'\right)\,\tau\left(t,t',b,c',\beta,\gamma'\right)\,\tau\left(t,t',d,b',\delta,\beta'\right)
\end{aligned} \tag{D.16}$$

D.2.3 $N\pi \to \Delta$

This matrix element has 3 terms contributing:

$$\frac{1}{\sqrt{2}}\,\Gamma^{A\dagger}_{\alpha'\mu}P^{\pm}_{\mu\alpha}\Gamma^{\Delta}_{\beta\gamma}\Gamma^{B\dagger}_{\gamma'\beta'}\Gamma^{\pi\dagger}_{\delta'\epsilon'}\;\; \widehat{\phi}^{snk}_{N}(a,b,c)\widehat{\phi}^{src}_{N}(a',b',c')\widehat{\phi}^{src}_{\pi}(d',e')\;\sum_{i=1}^{3} C_i\;, \tag{D.17}$$

where summation over index pairs is implied.

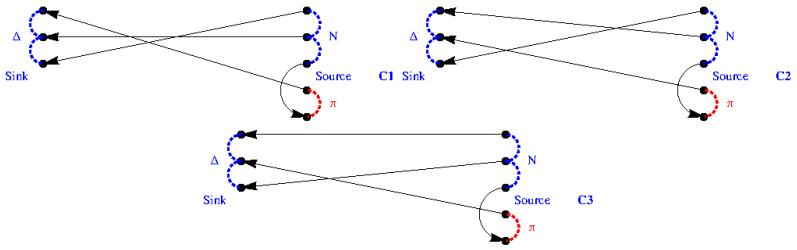

FIGURE D.9: Terms $C_1 - C_3$ contributing to $N\pi \to N$.

$$
\begin{aligned}
C_1 &= 2\,\tau\left(t,t',a,d',\alpha,\delta'\right)\,\tau\left(t,t',b,b',\beta,\beta'\right)\,\tau\left(t,t',c,a',\gamma,\alpha'\right)\,\tau\left(t',t',e',c',\epsilon',\gamma'\right)\\
C_2 &= -2\,\tau\left(t,t',a,b',\alpha,\beta'\right)\,\tau\left(t,t',b,d',\beta,\delta'\right)\,\tau\left(t,t',c,a',\gamma',\alpha'\right)\,\tau\left(t',t',e',c',\epsilon',\gamma'\right)\\
C_3 &= 2\,\tau\left(t,t',a,a',\alpha,\alpha'\right)\,\tau\left(t,t',b,d',\beta,\delta'\right)\,\tau\left(t,t',c,b',\gamma,\beta'\right)\,\tau\left(t',t',e',c',\epsilon',\gamma'\right)
\end{aligned}
\tag{D.18}
$$

D.2.4 $N\pi \to N\pi$ $(I = 3/2)$

Here 12 terms contribute:

$$
\frac{1}{2}\,\Gamma^{A\dagger}_{\alpha'\mu}P^{\pm}_{\mu\nu}\Gamma^{A}_{\nu\alpha}\Gamma^{B}_{\beta\gamma}\Gamma^{B\dagger}_{\gamma'\beta'}\Gamma^{\pi}_{\delta\epsilon}\Gamma^{\pi\dagger}_{\epsilon'\delta'}\;\;\widehat{\phi}^{snk}_{N}(a,b,c)\widehat{\phi}^{snk}_{\pi}(e,d)\widehat{\phi}^{src}_{N}(a',b',c')\widehat{\phi}^{src}_{\pi}(d',e')\;\sum_{i=1}^{12}D_i\;,
\tag{D.19}
$$

where summation over index pairs is implied.

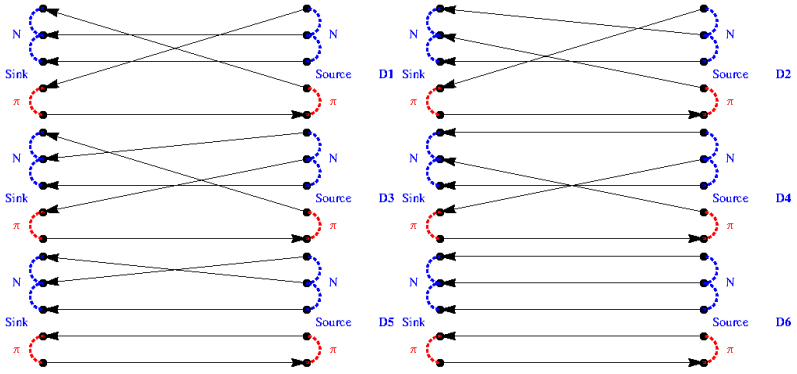

FIGURE D.10: Terms $D_1 - D_6$ contributing to $N\pi \to N\pi$.

$$
\begin{aligned}
D_1 &= +\tau\left(t,t',a,d',\alpha,\delta'\right)\ \tau\left(t,t',b,b',\beta,\beta'\right)\ \tau\left(t,t',c,c',\gamma,\gamma'\right)\\
&\qquad \tau\left(t',t,e',e,\epsilon',\epsilon\right)\ \tau\left(t,t',d,a',\delta,\alpha'\right)\\
D_2 &= -\tau\left(t,t',a,b',\alpha,\beta'\right)\ \tau\left(t,t',b,d',\beta,\delta'\right)\ \tau\left(t,t',c,c',\gamma,\gamma'\right)\\
&\qquad \tau\left(t',t,e',e,\epsilon',\epsilon\right)\ \tau\left(t,t',d,a',\delta,\alpha'\right)\\
D_3 &= -\tau\left(t,t',a,d',\alpha,\delta'\right)\ \tau\left(t,t',b,a',\beta,\alpha'\right)\ \tau\left(t,t',c,c',\gamma,\gamma'\right)\\
&\qquad \tau\left(t',t,e',e,\epsilon',\epsilon\right)\ \tau\left(t,t',d,b',\delta,\beta'\right)\\
D_4 &= +\tau\left(t,t',a,a',\alpha,\alpha'\right)\ \tau\left(t,t',b,d',\beta,\delta'\right)\ \tau\left(t,t',c,c',\gamma,\gamma'\right)\\
&\qquad \tau\left(t',t,e',e,\epsilon',\epsilon\right)\ \tau\left(t,t',d,b',\delta,\beta'\right)\\
D_5 &= +\tau\left(t,t',a,b',\alpha,\beta'\right)\ \tau\left(t,t',b,a',\beta,\alpha'\right)\ \tau\left(t,t',c,c',\gamma,\gamma'\right)\\
&\qquad \tau\left(t',t,e',e,\epsilon',\epsilon\right)\ \tau\left(t,t',d,d',\delta,\delta'\right)\\
D_6 &= -\tau\left(t,t',a,a',\alpha,\alpha'\right)\ \tau\left(t,t',b,b',\beta,\beta'\right)\ \tau\left(t,t',c,c',\gamma,\gamma'\right)\\
&\qquad \tau\left(t',t,e',e,\epsilon',\epsilon\right)\ \tau\left(t,t',d,d',\delta,\delta'\right)
\end{aligned}
\tag{D.20}
$$

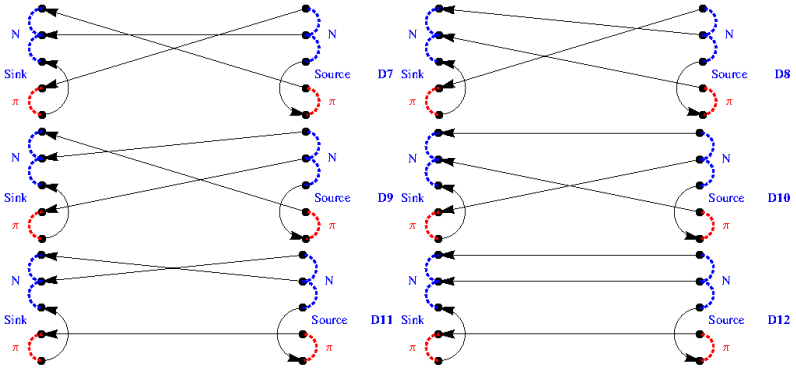

FIGURE D.11: Terms $D_7 - D_{12}$ contributing to $N\pi \to N\pi$.

$$
\begin{aligned}
D_7 = &-\tau\left(t,t,c,e,\gamma,\epsilon\right)\,\tau\left(t,t',a,d',\alpha,\delta'\right)\,\tau\left(t,t',b,b',\beta,\beta'\right)\\
&\tau\left(t,t',d,a',\delta,\alpha'\right)\,\tau\left(t',t',e',c',\epsilon',\gamma'\right)\\
D_8 = &+\tau\left(t,t,c,e,\gamma,\epsilon\right)\,\tau\left(t,t',a,b',\alpha,\beta'\right)\,\tau\left(t,t',b,d',\beta,\delta'\right)\\
&\tau\left(t,t',d,a',\delta,\alpha'\right)\,\tau\left(t',t',e',c',\epsilon',\gamma'\right)\\
D_9 = &+\tau\left(t,t,c,e,\gamma,\epsilon\right)\,\tau\left(t,t',a,d',\alpha,\delta'\right)\,\tau\left(t,t',b,a',\beta,\alpha'\right)\\
&\tau\left(t,t',d,b',\delta,\beta'\right)\,\tau\left(t',t',e',c',\epsilon',\gamma'\right)\\
D_{10} = &-\tau\left(t,t,c,e,\gamma,\epsilon\right)\,\tau\left(t,t',a,a',\alpha,\alpha'\right)\,\tau\left(t,t',b,d',\beta,\delta'\right)\\
&\tau\left(t,t',d,b',\delta,\beta'\right)\,\tau\left(t',t',e',c',\epsilon',\gamma'\right)\\
D_{11} = &-\tau\left(t,t,c,e,\gamma,\epsilon\right)\,\tau\left(t,t',a,b',\alpha,\beta'\right)\,\tau\left(t,t',b,a',\beta,\alpha'\right)\\
&\tau\left(t,t',d,d',\delta,\delta'\right)\,\tau\left(t',t',e',c',\epsilon',\gamma'\right)\\
D_{12} = &+\tau\left(t,t,c,e,\gamma,\epsilon\right)\,\tau\left(t,t',a,a',\alpha,\alpha'\right)\,\tau\left(t,t',b,b',\beta,\beta'\right)\\
&\tau\left(t,t',d,d',\delta,\delta'\right)\,\tau\left(t',t',e',c',\epsilon',\gamma'\right)
\end{aligned}
\tag{D.21}
$$

Bibliography

[1] U.-G. Meissner, PiN Newslett. **16**, 1 (2002), [arXiv:hep-ph/0108133].

[2] Particle Data Group, J. Beringer *et al.*, Phys. Rev. D **86**, 010001 (2012).

[3] M. Gell-Mann, Phys.Lett. **8**, 214 (1964).

[4] G. Zweig, (1964).

[5] K. G. Wilson, Phys. Rev. D **10**, 2445 (1974).

[6] S. Cohen *et al.*, PoS **LAT2009**, 112 (2009), [arXiv:0911.3373].

[7] M. S. Mahbub *et al.*, PoS **LAT2009**, 118 (2009), [arXiv:0910.2789].

[8] J. J. Dudek, R. G. Edwards, M. J. Peardon, D. G. Richards and C. E. Thomas, Phys. Rev. D **82**, 034508 (2010), [arXiv:1004.4930].

[9] J. Bulava *et al.*, Phys. Rev. D **82**, 014507 (2010), [arXiv:1004.5072].

[10] BGR [Bern-Graz-Regensburg], G. P. Engel, C. B. Lang, M. Limmer, D. Mohler and A. Schäfer, Phys. Rev. D **82**, 034505 (2010), [arXiv:1005.1748].

[11] G. P. Engel, C. B. Lang and A. Schäfer, Low-lying lambda baryons from the lattice, 2012, [arXiv:1212.2032].

[12] Hadron Spectrum Collaboration, M. Peardon *et al.*, Phys. Rev. D **80**, 054506 (2009), [arXiv:0905.2160].

[13] C. Michael, Nucl. Phys. B **259**, 58 (1985).

[14] M. Lüscher, Commun. Math. Phys. **104**, 177 (1986).

[15] M. Lüscher and U. Wolff, Nucl. Phys. B **339**, 222 (1990).

[16] B. Blossier, M. DellaMorte, G. von Hippel, T. Mendes and R. Sommer, JHEP **0904**, 094 (2009), [arXiv:0902.1265].

[17] C. B. Lang, D. Mohler, S. Prelovsek and M. Vidmar, Phys. Rev. D **84**, 054503 (2011), [arXiv:1105.5636].

[18] CS, S. Aoki *et al.*, Phys. Rev. D **84**, 094505 (2011), [arXiv:1106.5365].

[19] X. Feng, K. Jansen and D. B. Renner, Phys. Rev. D **83**, 094505 (2011), [arXiv:1011.5288].

[20] C. B. Lang, L. Leskovec, D. Mohler and S. Prelovsek, Phys. Rev. D **86**, 054508 (2012), [arXiv:1207.3204].

[21] D. Mohler, S. Prelovsek and R. M. Woloshyn, D Pi scattering and D meson resonances from lattice QCD, 2012, [arXiv:1208.4059].

[22] C. Pelissier and A. Alexandru, Resonance parameters of the rho-meson from asymmetrical lattices, 2012, [arXiv:1211.0092].

[23] M. Lüscher, Commun. Math. Phys. **105**, 153 (1986).

[24] M. Lüscher, Nucl. Phys. B **354**, 531 (1991).

[25] M. Lüscher, Nucl. Phys. B **364**, 237 (1991).

[26] V. Bernard, M. Lage, U.-G. Meißner and A. Rusetsky, JHEP **08**, 024 (2008), [arXiv:0806.4495].

[27] M. Döring, J. Haidenbauer, U.-G. Meißner and A. Rusetsky, Eur. Phys. J. **A47**, 163 (2011), [arXiv:1108.0676].

[28] L. Roca and E. Oset, Phys.Rev. **D85**, 054507 (2012), [arXiv:1201.0438].

[29] J. M. M. Hall, A. C. P. Hsu, D. B. Leinweber, A. W. Thomas and R. D. Young, Baryon resonances and hadronic interactions in a finite volume, 2012, [arXiv:1207.3562].

[30] U. G. Meißner, K. Polejaeva and A. Rusetsky, Nucl. Phys. B **846**, 1 (2011), [arXiv:1007.0860].

[31] P. Giudice, D. McManus and M. Peardon, Phys.Rev. **D86**, 074516 (2012), [arXiv:1204.2745].

[32] K. Rummukainen and S. Gottlieb, Nucl. Phys. B **450**, 397 (1995), [arXiv:hep-lat/9503028].

[33] C. h. Kim, C. T. Sachrajda and S. R. Sharpe, Nucl. Phys. **B727**, 218 (2005), [arXiv:hep-lat/0507006].

[34] Z. Fu, Phys. Rev. D **85**, 014506 (2012), [arXiv:1110.0319].

[35] L. Leskovec and S. Prelovsek, Phys. Rev. D **85**, 114507 (2012), [arXiv:1202.2145].

[36] M. Göckeler *et al.*, Phys. Rev. D **86**, 094513 (2012), [arXiv:1206.4141].

[37] L. D. Roper, Phys. Rev. Lett. **12**, 340 (1964).

[38] L. Y. Glozman, Nucl. Phys. A **663**, 103 (2000), [arXiv:hep-ph/9908423].

[39] H.-W. Lin and S. D. Cohen, AIP Conf.Proc. **1432**, 305 (2012), [arXiv:1108.2528].

[40] K.-F. Liu *et al.*, PoS **LATTICE2013**, 507 (2014), [arXiv:1403.6847].

[41] W. Kamleh, D. B. Leinweber and D. S. Roberts, PoS **LATTICE2013**, 245 (2013), [arXiv:1312.2314].

[42] M. S. Mahbub, W. Kamleh, D. B. Leinweber, P. J. Moran and A. G. Williams, Phys.Lett. **B707**, 389 (2012), [arXiv:1011.5724].

[43] C. Alexandrou, J. W. Negele and M. Petschlies, PoS **LATTICE2013**, 281 (2014).

[44] H. Fritzsch, M. Gell-Mann and H. Leutwyler, Phys. Lett. **B47**, 365 (1973).

[45] D. K. Hong, hep-ph/0412132.

[46] S. Nussinov, hep-ph/0307357.

[47] R. L. Jaffe and F. Wilczek, Phys.Rev.Lett. **91**, 232003 (2003), [arXiv:hep-ph/0307341].

[48] R. Jaffe and F. Wilczek, Eur.Phys.J. **C33**, S38 (2004), [arXiv:hep-ph/0401034].

[49] L. Glozman, Phys.Rev.Lett. **92**, 239101 (2004), [arXiv:hep-ph/0309092].

[50] L. Y. Glozman, W. Plessas, K. Varga and R. Wagenbrunn, Phys. Rev. D **58**, 094030 (1998), [arXiv:hep-ph/9706507].

[51] L. Y. Glozman and D. O. Riska, Phys. Rept. **268**, 263 (1996), [arXiv:hep-ph/9505422].

[52] E. Seiler, *Gauge Theories as a Problem of Constructive Quantum Field Theory and Statistical Mechanics*, Springer Lecture Notes in Physics Vol. 159 (Springer, Berlin Heidelberg New York, 1982).

[53] M. Creutz, *Quarks, Gluons and Lattices* (Cambridge University Press, Cambrigdge UK, 1983).

[54] C. Rebbi, *Lattice Gauge Theories and Monte Carlo Simulations* (World Scientific, Singapore, 1983).

[55] M. Creutz, *Quantum Fields on the Computer* (World Scientific, Singapore, 1992).

[56] H. J. Rothe, *Lattice Gauge Theories - An Introduction* (World Scientific, Singapore, 1992).

[57] I. Montvay and G. Münster, *Quantum Fields on a Lattice* (Cambridge University Press, Cambridge New York, 1994).

[58] J. Smit, *Introduction to Quantum Fields on a Lattice* (Cambridge University Press, Cambridge UK, 2002).

[59] C. Gattringer and C. B. Lang, *Quantum Chromodynamics on the Lattice: An Introductory Presentation* , Lecture Notes in Physics Vol. 788 (Springer, Berlin Heidelberg, 2010).

[60] S. Weinberg, Physica **A96**, 327 (1979).

[61] J. Gasser and H. Leutwyler, Nucl. Phys. B **250**, 465 (1985).

[62] Y. Nambu and G. Jona-Lasinio, Phys. Rev. **124**, 246 (1961).

[63] Y. Nambu and G. Jona-Lasinio, Phys. Rev. **122**, 345 (1961).

[64] H. B. Nielsen and M. Ninomiya, Phys. Lett. B **105**, 219 (1981).

[65] P. H. Ginsparg and K. G. Wilson, Phys. Rev. D **25**, 2649 (1982).

[66] A. Hasenfratz, R. Hoffmann and S. Schaefer, Phys. Rev. D **78**, 054511 (2008), [arXiv:0806.4586].

[67] A. Hasenfratz, R. Hoffmann and S. Schaefer, Phys. Rev. D **78**, 014515 (2008), [arXiv:0805.2369].

[68] APE, M. Albanese *et al.*, Phys. Lett. B **192**, 163 (1987).

[69] A. Hasenfratz and F. Knechtli, Phys.Rev. **D64**, 034504 (2001), [arXiv:hep-lat/0103029].

[70] T. Blum *et al.*, Phys. Rev. **D55**, 1133 (1997), [arXiv:hep-lat/9609036].

[71] MILC, K. Orginos, D. Touissant and R. Sugar, Phys. Rev. D **D0**, 054503 (1999), [arXiv:hep-lat/9903032].

[72] S. Dürr, Comput. Phys. Commun. **172**, 163 (2005), [arXiv:hep-lat/0409141].

[73] A. Hasenfratz, R. Hoffmann and S. Schaefer, JHEP **0705**, 029 (2007), [arXiv:hep-lat/0702028].

[74] S. Schaefer, A. Hasenfratz and R. Hoffmann, PoS **LAT2007**, 132 (2007), [arXiv:0709.4130].

[75] S. Dürr, Comput. Phys. Commun. **180**, 1338 (2009), [arXiv:0709.4110].

[76] P. J. Moran, P. O. Bowman, D. B. Leinweber, A. G. Williams and J. B. Zhang, Impact of stout-link smearing in lattice fermion actions, 2009, [arXiv:0910.2781].

[77] B. Sheikholeslami and R. Wohlert, Nucl. Phys. B **259**, 572 (1985).

[78] D. H. Weingarten and D. N. Petcher, Phys. Lett. B **99**, 333 (1981).

[79] R. C. Johnson, Phys. Lett. B **114**, 147 (1982).

[80] R. Barrett *et al.*, *Templates for the Solution of Linear Systems: Building Blocks for Iterative Methods* (SIAM, Philadelphia, 1994).

[81] W. H. Press and S. A. Teukolsky, Computers in Physisc **6**, 400 (1992).

[82] A. Stathopoulos and K. Orginos, Computing and deflating eigenvalues while solving multiple right hand side linear systems in Quantum Chromodynamics, 2007, [arXiv:0707.0131].

[83] M. Lüscher, JHEP **07**, 081 (2007), [arXiv:0706.2298].

[84] S. Ciulli, C. Pomponiu and I. Sabba-Stefanescu, Phys. Rep. **17**, 133 (1975).

[85] G. P. Lepage *et al.*, Nucl. Phys. (Proc. Suppl.) **106**, 12 (2002), [arXiv:hep-lat/0110175].

[86] Y. Chen *et al.*, hep-lat/0405001.

[87] M. Asakawa, T. Hatsuda and Y. Nakahara, Prog. Part. Nucl. Phys. **46**, 459 (2001), [arXiv:hep-lat/0011040].

[88] J. J. Dudek *et al.*, Phys. Rev. D **83**, 111502 (2011), [arXiv:1102.4299].

[89] Hadron Spectrum Collaboration, L. Liu *et al.*, JHEP **1207**, 126 (2012), [arXiv:1204.5425].

[90] C. Morningstar *et al.*, Phys. Rev. D **83**, 114505 (2011), [arXiv:1104.3870].

[91] J. Bulava, *An Improved Variance Reduction Technique for Stochastic All-to-All Quark Propagators in Lattice QCD Spectrum Computations*, PhD thesis, Mellon College of Science at Carnegie Mellon University, 2009.

[92] S. Aoki *et al.*, Phys. Rev. D **70**, 034503 (2004), [arXiv:hep-lat/0312011].

[93] C. Kim, C. T. Sachrajda and S. R. Sharpe, Nucl. Phys. B **727**, 218 (2005), [arXiv:hep-lat/0510022].

[94] C. Lang and V. Verduci, Phys.Rev. **D87**, 054502 (2013), [arXiv:1212.5055].

[95] R. A. Arndt, W. J. Briscoe, I. I. Strakovsky and R. L. Workman, Phys. Rev. C **74**, 045205 (2006), [arXiv:nucl-th/0605082].

[96] D. Manley and E. Saleski, Phys. Rev. D **45**, 4002 (1992).

[97] R. Koch, Nucl. Phys. A **448**, 707 (1986).

[98] R. E. Cutkosky, C. P. Forsyth, R. E. Hendrick and R. L. Kelly, Phys. Rev. D **20**, 2839 (1979).

[99] C. McNeile, PoS **LATTICE2007**, 019 (2007), [arXiv:0710.0985].

[100] K. Jansen, C. Michael and C. Urbach, Eur. Phys. J. C **58**, 261 (2008), [arXiv:0804.3871].

[101] BGR, G. P. Engel, C. Lang, D. Mohler and A. Schäfer, Phys.Rev. **D87**, 074504 (2013), [arXiv:1301.4318].

[102] S. Weinberg, Phys. Rev. Lett. **17**, 616 (1966).

[103] Y. Tomozawa, Nuovo Cim. **A46**, 707 (1966).

Acknowledgements

To conclude I would like to thank those who have been involved in the preparation of this thesis. First of all I would like to thank my advisor Christian B. Lang for the interest demonstrated in my work and the constant support. I would like to thank all the members of the Lattice group and of the DK for contributing, step by step, to my understanding of the subject and to my education. I thank Sasa Prelovsek for the interesting discussions and for being a model of enthusiastic scientist for me and many other women in science. I also want to thank my family for supporting me during all these years of studying and for being always present. Finally would like to say *thank you* to all my colleagues who shared with me the joy and the pain of research.

Thank you.